UNIVERSIDAD AUTÓNOMA DE NUEVO LEÓN

FACULTAD DE INGENIERÍA MECÁNICA Y ELÉCTRICA

DIVISIÓN DE ESTUDIOS DE POSGRADO

FATIGA DE UN ACERO AISI/SAE 5160 CON TEMPLE INTERRUMPIDO

POR

DIEGO EMILIO LOZANO DE LA GARZA

TESIS

EN OPCION AL GRADO DE DOCTOR EN INGENIERIA DE MATERIALES

CIUDAD UNIVERSITARIA ABRIL 2013

UNIVERSIDAD AUTÓNOMA DE NUEVO LEÓN

FACULTAD DE INGENIERÍA MECÁNICA Y ELÉCTRICA

DIVISIÓN DE ESTUDIOS DE POSGRADO

FATIGA DE UN ACERO AISI/SAE 5160 CON TEMPLE INTERRUMPIDO

POR

DIEGO EMILIO LOZANO DE LA GARZA

TESIS

EN OPCION AL GRADO DE DOCTOR EN INGENIERIA DE MATERIALES

CIUDAD UNIVERSITARIA ABRIL 2013

UNIVERSIDAD AUTÓNOMA DE NUEVO LEÓN
FACULTAD DE INGENIERÍA MECÁNICA Y ELÉCTRICA
DIVISIÓN DE ESTUDIOS DE POSTGRADO

Los miembros del comité de la tesis recomendamos que la tesis **"Fatiga de un Acero AISI/SAE 5160 con Temple Interrumpido"** realizada por el M.C. Diego Emilio Lozano de la Garza sea aceptada para su defensa como opción al grado de Doctor en Ingeniería de Materiales

El Comité de Tesis

Asesor
Dr. Rafael David Mercado Solís

Coasesor
Dr. Rafael Colás Ortiz

Coasesor
Dr. Rodrigo González López

Revisor
Dr. Alberto Cantú Pérez

Revisor
Dr. Bernardo Hernández Morales

Vo. Bo.
Dr. Moisés Hinojosa

San Nicolás de los Garza, N. L., Abril de 2013

DEDICATORIA

A mi esposa Gaby, por tu amor y apoyo. El primer día del doctorado nos conocimos y el último nos unimos. Te amo.

A mis padres Jesús y Rita, este trabajo es el fruto de su empeño y paciencia de muchos años. Muchas gracias por todos sus sacrificios.

A mis hermanos

A mis abuelos

AGRADECIMIENTOS

Al Consejo Nacional de Ciencia y Tecnología por el apoyo económico brindado, el cual es una motivación para el desarrollo de la investigación en el México.

A la Facultad de Ingeniería Mecánica y Eléctrica y la Universidad Autónoma de Nuevo León.

Al Dr. Rafael Mercado por su orientación, apoyo, exigencias y revisiones durante la investigación. Por haber sido quien me encamino hacia este fascinante tema.

Al Dr. Rafael Colás por todo su aporte, ayuda, consejos y revisiones.

Agradecimiento especial a George Totten por su incansable apoyo, y por ser un motivador natural.

A Lauralice Canale y Luigi Mazzuco, por todo su apoyo y ayuda durante una bella y fructífera estancia, en donde surgieron grandes ideas que hicieron posible alcanzar objetivos ambiciosos. Gracia a Luigi por recibirme y convertirse en un buen amigo.

A la Dra. Martha Guerrero por su ayuda y colaboración bienintencionada, la cual facilitó la realización de este proyecto.

A Nelson, Javier, y todos los de una u otra manera ayudaron y participaron durante la realización del proyecto.

CONTENTS

ABSTRACT

AISI 5160 steel is used for the production of coil and leaf springs. Springs are usually oil-quenched and tempered. In this work, a brine solution is used as a quenchant. The brine promotes a more severe and uniform quenching. The severity of the quenching was analysed, and the heat transfer characteristics determined. A brine interrupted quenching was developed to produce a martensite case with a bainite core. The effect of various conditions after the interruption of the cooling is addressed. Tempering temperatures of 150, 250, 350 , 450 and 550 °C were employed. In addition, a partial decarburisation was promoted in the samples prior to the quenching and tempering, this in order to modify the local martensite start temperature and promote the martensite transformation to take place at a higher temperature, while reducing the amount of retained austenite. To determine the fatigue properties of heat treatments, a rotating bending fatigue tester with constant deflection was developed. Fatigue results showed that the interrupted brine quenching with partial decarburisation has a higher fatigue limit that the case with no decarburisation and also that the case of conventional oil quenching and tempering. Fractography and load data from experiments allowed to model the cracking stages. The model was useful to establish the presence of cracks and their length. It was found that when a martensite case and a pearlite core was produced, nucleation was retarded up to 5 times, however after a crack nucleates it propagates much rapid than in bainite.

CHAPTER 1

INTRODUCTION

Along history mechanical failures have been the cause of human and money losses. Mechanical failures are promoted by a complex sum of variables such as load, service time, load type and environment. The cost of failures represents about 4% of the Gross National Product in the US [1] [2]. There are critical components from which a failure would be catastrophic, such as structural components of transportation vehicles and structures in general. For these applications, components might need to be overdesigned in order to withstand an infinite life. Although this practice prevents failures, it is an expensive solution because the thicknesses of components have to be increased and high alloy steels are used, thus increasing the cost of the steel. In order to increase the fatigue resistance of materials, researchers are in continuous development of processes that improve the strength and resistance of materials, and at the same time reduce the final product cost.

5160 steel is commonly known as spring steel, and is used in the automotive industry for the manufacturing of coil and leaf springs. Springs are components subjected to variable cyclic loads, thus have to be designed to endure fatigue. For this reason, spring producers have to achieve certain mechanical

properties as well as high fatigue strength. Therefore, springs must undergo heat and surface treatments that increase the infinite fatigue life zone of the steel. The most common heat treatment employed in the manufacturing process of springs is austenitizing, followed by oil quenching and further tempering. Moreover, a shoot peening surface treatment is sometimes applied after heat treatment to produce compressive residual stresses at the surface.

Steel parts might suffer distortion during heat treatment. The geometric distortion of steels during quenching is caused mainly by a non uniform cooling of the part, which depends on many factors such as the geometry itself, phase transformation and cooling rate. In parts with complex geometry, distortion occurs firstly because of the presence of high thermal gradients within the part, which produce a non uniform thermal contraction of steel, prior to the phase transformation. This is, the thinner section cools faster and therefore it contracts before than the thicker sections of the part. Then, thermal stresses are induced and thinners sections can undergo plastic deformation.

A second mechanism that produces distortion is attributed to transformational stresses, which are generated because the non-uniform expansion of the material takes place due to a heterogeneous transformation of martensite through the part. Since martensite exhibit higher specific volume than austenite, sections that are cooled first, expand due to phase transformation while other austenite zones are still contracting. Thus, there are simultaneous time intervals when the part has martensite and austenite zones. The expansion of martensite causes stresses in the still plastic austenite zones, producing lattice distortion [3] [4].

The use of oil base quenchants is very common because they provide a moderate heat extraction compared with water, which has a higher heat extraction capacity. The magnitude of internal stresses relates directly on the heat extraction

rate (cooling rate). A very fast cooling produces a high thermal gradient within the part, generating high stresses due to the expansion of martensite and thermal contraction of austenite, therefore producing distortion and cracking. On the other hand, with slow cooling such as oil quenching, low thermal gradients are maintained through the cross section, about 30 ºC between the centre and the surface [5], which means a practically simultaneous phase transformation, minimising thermal and transformational stresses.

Recent studies have proved that it is possible to substitute the conventional oil quenching with a process called Intensive Quenching (IQ), which uses water base solutions as quenchants and high agitation, bestowing considerable improved properties [6]. Although it is known that increasing the cooling rate increases the propensity of cracking, Kobasko [7] states that there is a critical cooling rate where the probability of cracking reaches a maximum and then drops with further increase on the cooling rate (Figure 1.1). The improvement in properties that is reached by IQ is of such magnitude that the content of alloying elements in steel can be reduced.

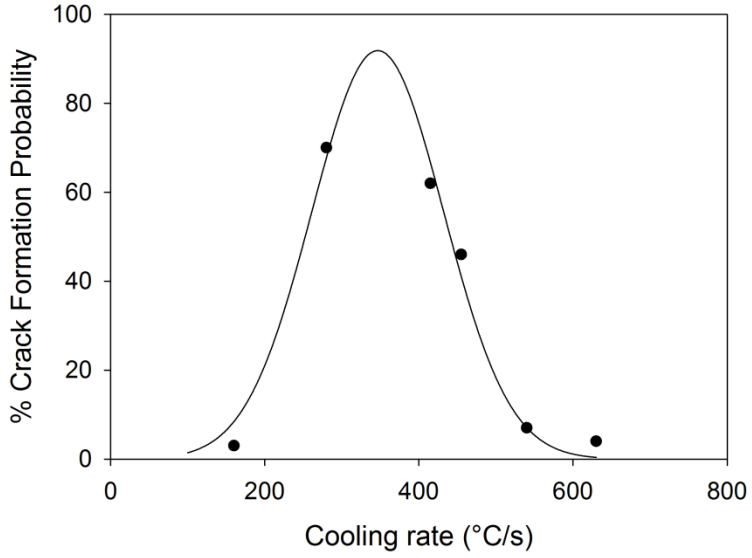

Figure 1.1 Crack formation probability as function of cooling rate [7]

The intensive quenching technique induces the formation of maximum residual compressive stresses at the surface, which might produce a beneficial effect in fatigue resistance. However, there is no evidence reported in the literature regarding the influence of the microstructure produced of intensively quenched steels on fatigue resistance. Moreover, the IQ has been already developed for large cross section (>5 cm) and there is no methodology for getting the IQ benefits in smaller cross-sections (if it is possible), since high thermal gradients between surface and core are more difficult to achieve and maintain in small sections.

Even though compressive residual stresses are known to increase fatigue life, their distribution plays a key role whether the fatigue life is improved or not. Then it is important to understand the residual stress distribution that affects the crack nucleation and propagation mechanism of an intensively quenched 5160 steel, as well as to analyse the effect of the microstructure obtained, during the different fatigue stages in order to improve and determine the proper heat treatment.

Hypothesis

By increasing the martensite start temperature of the surface through a partial decarburisation, and by producing high thermal gradients during quenching, it might be possible to obtain a shell-core type microstructure in small cross sections of AISI 5160 steel that increases its fatigue strength.

Aim

To produce a shell-core type microstructure in small cross section samples of AISI 5160 spring steel and to evaluate the effect of heat treatment conditions on its fatigue resistance using a laboratory scale system which allows monitoring the different stages of fatigue, including crack nucleation and growth.

To develop a fatigue tester capable of provide information about the cracking stages, while testing.

CHAPTER 2

BACKGROUND

2.1 Quenching

Thermal stresses are present during quenching due to the inherent thermal gradients typical of heat transfer processes. This temperature variation in addition to the thermal expansion coefficient of the material, determine the magnitude of the thermal stresses. The specific volume of phases formed during quenching also induce extra stresses in the lattice. These transformational and thermal stresses may cause plastic deformation if the yielding point is overreached, and cracking if the tensile strength is exceeded **[8]**.

Quenching has been traditionally designed to produce through hardening, this is, a fully martensitic microstructures. To minimise cracking, thermal gradients must be diminished by using slow cooling as it is oil quenching. Greater hardenability can be obtained by using higher alloying steels. Whereas in the Intensive Quenching (IQ) process the desired microstructure consist of a tempered martensite shell and a mixed core of bainite, pearlite and ferrite. High strength is obtained in the material due to the creation of a high dislocation density during IQ.

The dislocations are trapped instead of clustering at grain boundary, which improves the plastic properties of material. A high dislocation density in addition to compressive residual stresses at superficial layers increase the life of steel part **[9]**.

2.1.1 Cooling Stages

When a vapourisable fluid is put in contact with a hot metal surface (850°C for common austenitizing temperature), different heat transfer mechanism take place as the surface cools (1st film boiling, 2nd nucleate boiling and 3rd convection). A typical cooling and cooling rate curves are shown in figure 2.1. More detailed information regarding the stages of quenching is available on [10] [11] [12].

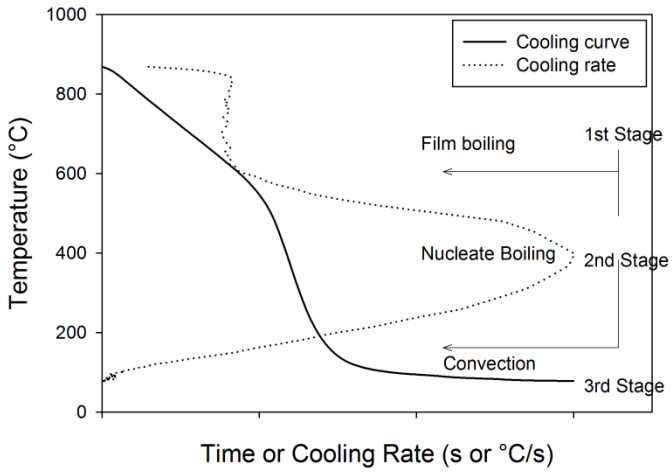

Figure 2.1 Typical cooling and cooling rate curves displaying the cooling stages when quenching in a vaporisable fluid [10].

The first stage of cooling consists in the formation of a vapour film which surrounds the entire part, known as full film boiling or vapour blanket stage. During this low heat transfer stage, the vapour formed around the surface isolates the part from

being wetted by the quenchant. The duration of the full film boiling depends on the thermophysical properties of the quenchant like its saturation temperature, thermal conductivity and temperature [13]; and on physical properties of the quenched part such as its thermal conductivity, roughness and shape [14] [15]. This particular stage is very sensitive to the temperature of the quenchant and concentration of salts in the solution [16] [17].

In the case of pure water, an increase on its temperature promotes longer duration and stability of vapour film, due to the reduction in the energy required to evaporate it [10] (see Fig.2.2).

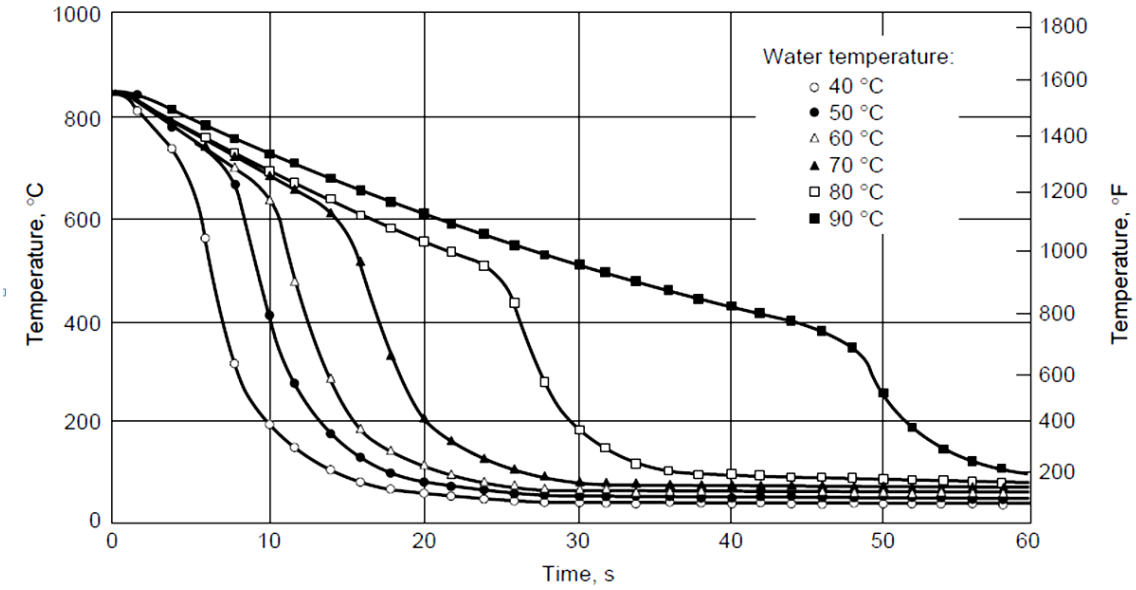

Figure 2.2 Effect of water temperature on full film boiling duration.

The addition of different salts and alkali even in slow concentrations produce a considerable reduction of the film boiling stage and even eliminate it at optimal concentrations. In general, the cooling rate increases with an increase in

concentration up to a critical point where further increments in concentration may reduce the cooling capacity of the quenchant.

The second stage of the cooling consists in the massive formation of bubbles that causes a high increase of heat flux due to the rupture of the vapour blanket and the direct contact of the liquid with the surface. This stage exhibits high heat transfer due to the formation of great amounts of bubbles at the surface. During the nucleate boiling stage, surface temperature drops drastically to approximately the boiling temperature of the quenchant. While the temperature of the part decreases, heat flux diminishes to a point where the heat transfer mode switches to convection.

Finally, convective heat transfer takes place when the surface temperature of the part decreases slightly below the boiling temperature of the quenchant. (More detailed explanation of the heat transfer modes can be consulted in references **[18] [19]**)

These three stages of cooling are usually observed in cooling curves. According to Kobasko **[18]**, there is also a fourth mode at the very beginning of quenching, called the shock-film boiling. This stage is characterised by great heat flux density. In figure 2.3, it can be observed the four cooling modes as function of heat transfer coefficient (2.3a) and heat flux density (2.3b).

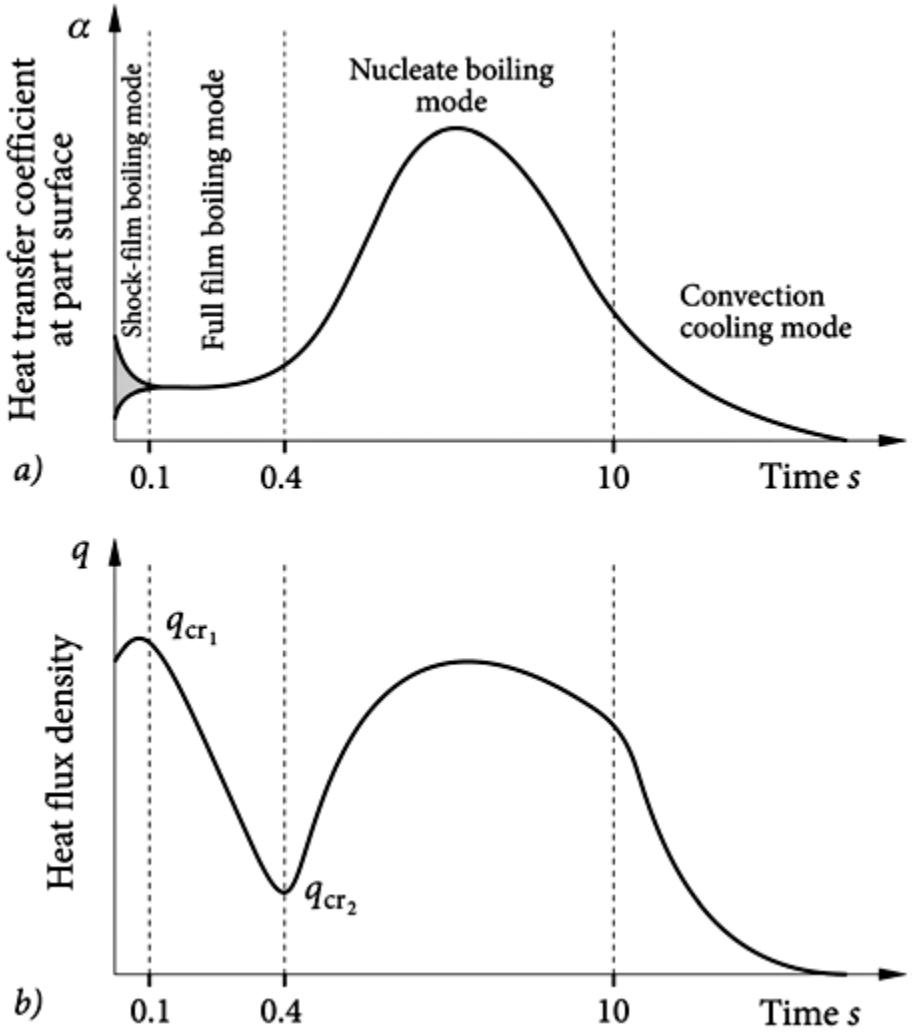

Figure 2.3 Modes of cooling during quenching (a) and critical heat flux densities (b) [20]

2.1.2 Intensive Quenching

There are different methods to achieve the intensive quenching in the martensitic range (IQ-1, IQ-2, IQ-3), which differ from one another in the heat transfer modes **[21]**.

It is worth to point out that the term "intensive quenching" is not necessarily related to great agitation of the quenchant. Instead, the term is used to describe a procedure where high enough thermal gradients are produced between the surface and the core, which produce maximum compressive residual stresses due to transformational and thermal stresses when the cooling is stopped.

IQ-1is a two steps cooling, beginning with a slow cooling from the austenitizing temperature to the martensite start temperature (Ms), followed by intensive quenching.

IQ-2 is a three steps cooling that consists in an initial cooling that prevents the vapour blanket formation at the surface until 50 % martensite is reached at superficial layers. At this point the cooling is interrupted, and the steel part is cooled in air, getting an homogenisation of the temperature through the cross section and producing a self-tempering of the martensite superficial layers just formed. Finally, intensive quenching is continued until martensitic transformation is completed. The usage of salt based solutions is necessary in this method in order to avoid the vapour blanket formation.

IQ-3 consists in a very intensive cooling where the vapour blanket and the nucleate boiling are avoided, taking place only convective heat transfer. In this method, the great flux of quenchants cools the surface almost instantly, generating a maximum temperature gradient possible between the surface and the core. The intensive cooling is maintained until maximum surface compressive stresses are reached, then the part is cooled in air. The time and water flux depends on the geometry of the part and steel composition. IQ-3 is the most intensive of the three methods and is possible to increase the service life of steel parts 1.5 to 2 times compared to the conventional oil quenching according to reference **[21]**.

2.1.3 Distortion minimisation

Reduction of distortion and cracking during the intensive quenching can be explained if a conventional quenching is analysed, in which the cooling and martensite transformation takes place firstly in the thinner sections of the real part (Figure 2.4a), while thicker section have not transformed yet. A volume expansion of about 4.3% in the cold zones is promoted because martensite has higher specific volume than austenite. At the same time, austenitic zones undergo thermal contraction generating high stresses, which may cause deformation and cracking [3] [6] [7] [8].

The key difference in the IQ is remarked by the great heat extraction ability of the quenchant (generally produced by great agitation), producing a more uniform cooling at the surface of the part, independently of the geometry of the part (Figure 2.4b). This uniform cooling minimises distortion and cracking, also generating compressive residual stresses at surface if properly interrupted.

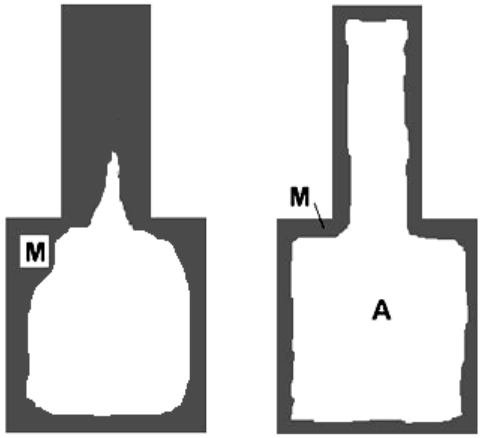

Figure 2.4 Phase transformation during conventional quenching a), and intensive quenching b).

2.1.4 Generation of residual stresses

During quenching there are two main types of stresses, thermal stresses and transformational stresses. The first ones arises from the different cooling rates that experiment the surface and the core, while the transformation stresses appear due to volume changes when the phases transform.

Generation of compressive superficial residual stresses in steel through the usage of IQ can be described by means of the model of Figure 2.5. Only radial heat transfer will occur if the cooling of a cylinder sufficient long to avoid the end cooling effects is considered [22]. Thus, a one-dimensional model can be used, where temperature gradients arise as concentric circles [23]. It is considered that the concentric circles are formed by “balls” which are joined together each other with springs to illustrate the stresses (Figure 2.6). When the piece is heated above the A_{C3} temperature of steel, the springs are in an equilibrium state of relaxation and there are not stresses between the balls ($\sigma=0$, Figure 2.5.a).

During cooling, the surface cools very quickly causing thermal contraction of the outer balls. Because the core is still hot and therefore is still expanded and large, the surface layer experiecing shrinkage is constrained to maintain the size of the core. Then, tensile stresses are generated in the axial and circumferential directions of the cooling shell. This shrinkage breaks the equilibrium state and the springs of the outer circle of balls expand as a reaction to this contraction, simulating the creation of tensile stresses (Figure 2.5b).

After further cooling, martensite (blue balls in Figure 2.5.) will start to form from the outermost layers to the core. Since the martensitic transformation is

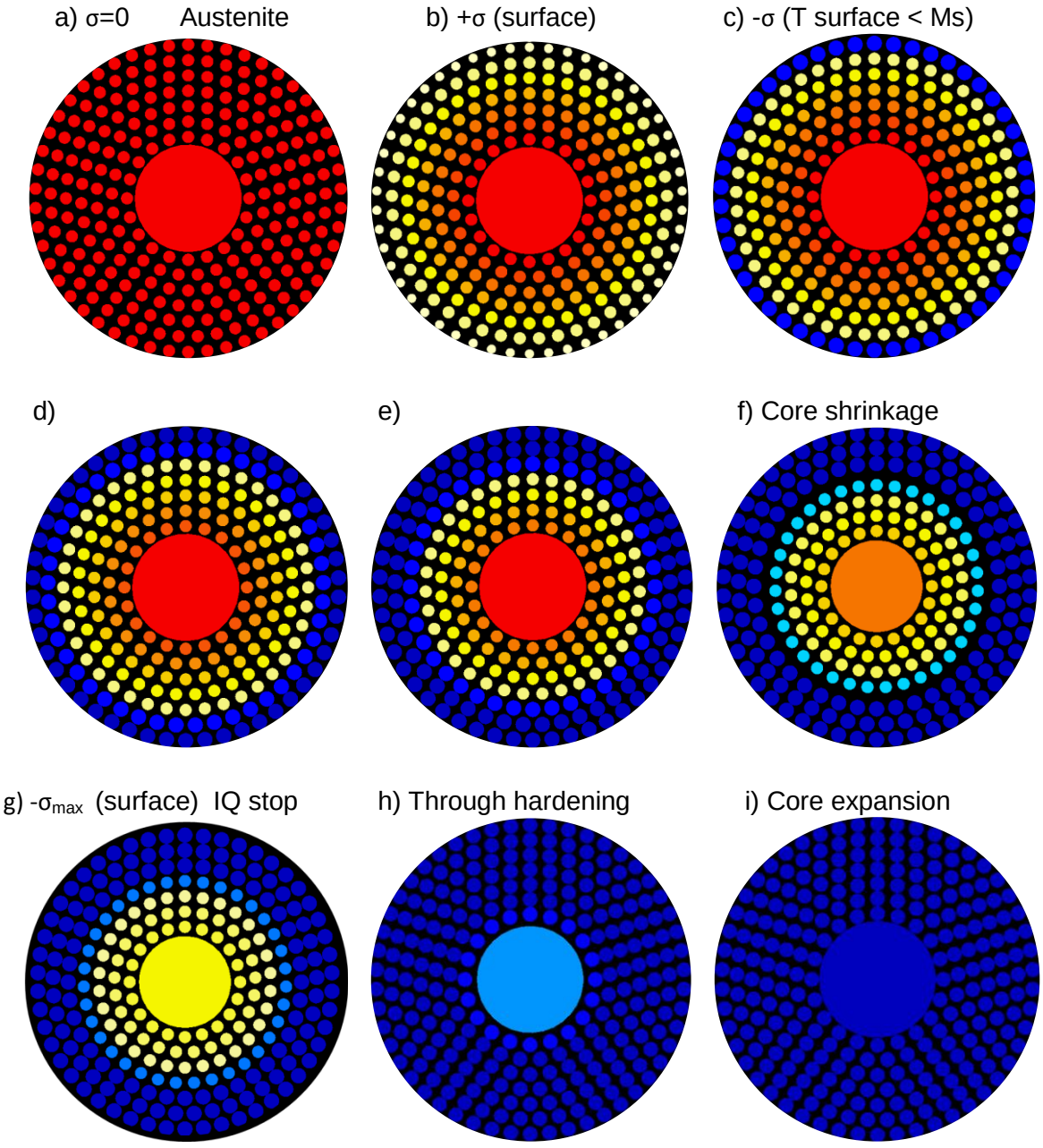

Figure 2.5 Thermal and transformational stresses during quenching of steel.

diffusionless (that depends only on temperature and not on time), transformation starts to take place instantly when the surface temperature reaches the M_s temperature of the steel (Figure 2.5c). These balls, as can be seen in the figure, expand due to the higher specific volume of martensite. This expansion is constrained once again by the size of the core, which compared to the martensite

is now small, and therefore, it pulls the outer layer to the core generating compressive stresses. These superficial compressive stresses ($\sigma<0$) are represented in figure 2.6 as a contraction of the springs.

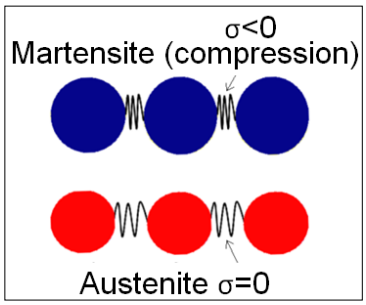

Figure 2.6 Stresses due to martensitic transformation during IQ.

During IQ the surface reaches the M_s temperature extremely fast, while the core is still hot, almost at the austenitizing temperature. At the time when the martensite transformation takes place at surface, the still austenitic core continues to cool and to contract (Figure 2.5f). Contraction of the core is constrained by the now cold and hard martensite layer, which conserves the initial part size with low distortion. The thermal contraction of the core drags the layer towards the centre, thus increasing the compressive stresses of the surface (the springs contract even more, see Figures 2.5f and g) and tensile stresses are present in the core.

At a certain point of the cooling, the surface compressive stresses reach a maximum value. This occurs an instant before the transformation to martensite at the core takes place (Figure 2.5g); to obtain the maximum surface compressive stresses, the intensive cooling must be interrupted in that moment. The cooling rate will slowdown, and martensite formation is interrupted as well. With enough time to diffuse, the austenite of the core will transform into more stable structures such as bainite, pearlite and ferrite. Since these phases have lower specific volume

than martensite, the quenching results in a higher value of compressive residual stresses compared to the case of through hardening showed in figure 2.5i.

Although at this point the stress distribution is like the one exhibited in carburized steels (See figure 2.7b), that distribution is attained by different mechanisms. In both IQ and carburisation, surface compressive residual stresses are generated by means of constraining the free expansion of martensite at surface layers. In the IQ the expansion is constrained by the austenitic core which is smaller compared as it would be if it were of martensite.

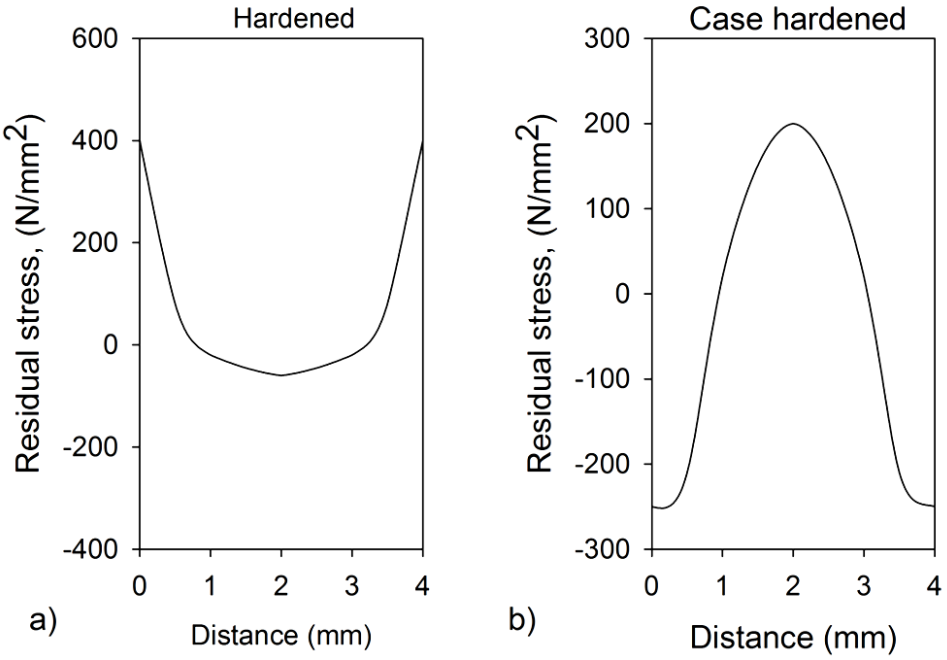

Figure 2.7 Distribution of residual stresses across the thickness of hardened and a) case-hardened plate of 26MnCr4 steel b). [24]

In carburisation processes, carbon content plays an important role by changing the Ms temperature (See figure 2.8). Thus, although during cooling the surface temperature is lower than that of the core, martensite transformation indeed occurs firstly at the core because of the lower carbon content. The

expanded martensite core deforms plastically the still austenite surface layer to the new core size. Afterwards, when surface reaches the Ms temperature, transformation takes place, however, the expansion is constrained by the core which do not allow the free swelling of surface layer. The stress distribution is observed in the figure 2.7b showing compressive residual stresses at the surface and tensile stresses at the core, similar to IQ.

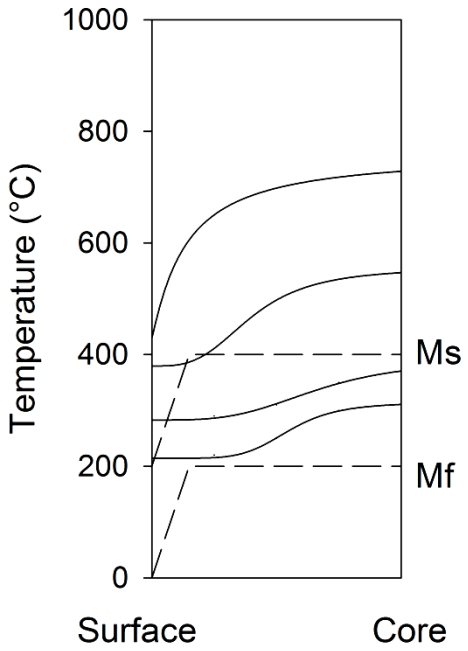

Figure 2.8 Temperature distribution and progress of martensitic transformation during quenching of a carburised steel bar [24]

2.1.5 Aqueous Salt Solutions

At room temperature, water has high cooling capacity. However, its low boiling temperature makes water unsuitable to be used for quenching of many steel grades and complex shapes. Moreover, high cooling rates are associated with high thermal gradients within the quenched part, and therefore related with cracking and distortion [25]. In addition, water quenching promotes a non-uniform cooling, since at the beginning of the cooling a vapour blanket forms and covers the steel part, isolating it from the quenchant [26] [27] [14] [28]. To promote a uniform cooling, the vapour blanket or full film boiling stage might be reduced or eliminated either by the usage of salt additives or destabilised by agitation.

Aqueous solutions containing salts or alkalis are called Brines (usually NaCl), although the term has been used for some authors to refer aqueous solutions with other salts [29] [30] [31] [32] [33]. Commonly employed salts include chlorides, nitrides, sulphates and hydroxides [10] [34] [35]. Such additives, which form negative ions when dissolved in water, are attracted by the positive charge of the metal surface and destabilise the vapour film (if formed), producing its collapse [36] [37] [29]. In addition to reduce or eliminate the film boiling stage, higher cooling rates are obtained with these aqueous solutions than pure water. Since high cooling rates might increase the propensity of cracking and distortion, the use of these solutions is frequently limited to quenching low-hardenability steels [10].

2.1.5.1 Cooling Power of Brines

Compared to other quenchants, brine has the highest heat extraction capacity. Many authors have compared the cooling power of various media using different methods and probes. Although there is no straightforward comparison from one author to other due to experimental methodology, there is a common agreement among researchers regarding the ranking positions of cooling capacities of various quenchants [38] [36] [27].

Figure 2.9 shows the cooling curve for different quenching media using the Japanese silver probe [38]. It can be seen that film boiling stage is apparently suppressed in the cooling curve of brine, and that the HTC calculations showed almost 4 times greater for brine than for water quenching (45 and 11 KW/m^2 K respectively) and 8-10 times greater than oil.

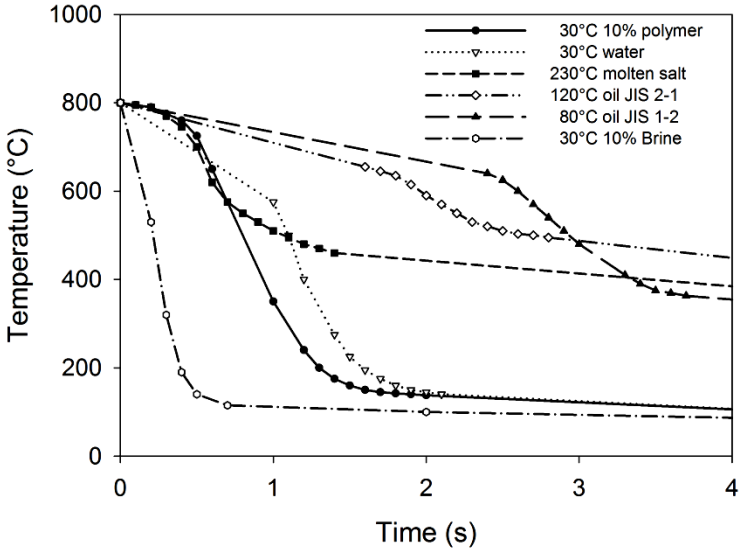

Figure 2.9 Cooling curves of different quenchants using a silver probe of 10 mm in diameter. [38]

The maximum cooling rate and heat transfer coefficient (HTC) values are usually employed to determine and to compare the severity of quenchants. However, it is worth to note that no single number of heat transfer coefficient nor cooling rate characterises a quenchant. These values are strongly dependent on material properties and shape (thickness) of the quenched sample, thus different HTC are obtained by changing the composition of the quenched part. There are various methods available in literature to evaluate the cooling capacity of quenchant for specific conditions [39,40,11,41,42], which are useful as a direct comparison between quenchants if experimental conditions are maintained. Nevertheless, for real geometries cooling rates and HTC might be lower. The thicker the section, the lower the HTC that a given quenchant produce [11]; thus to maintain similar heat transfer conditions on the same steel, cooling severity has to be increased for thicker parts and lowered for thinner sections.

Cooling capacity of salt aqueous solutions is usually increased proportionally with a concentration increase up to a maximum, which is commonly considered as an optimal concentration. The optimal concentration of a specific brine is related to the highest cooling rate achievable as function of composition. Usually further additions above the optimal concentration tend to decrease the cooling power of the solution. Saturated solutions might cool slower than pure water. In table 2.1 the cooling rate of different salts and concentrations are shown.

Water Solution	Concentration (%)	Cooling Rate (°C/s)
Water NaCl	0	102-120
	5	170
	10	195
$CaCl_2$	5	170
	10	193
	20	170
Na_2CO_3	10	170
NaOH	2.5	195
	5	202
	11.5	202
	16.5	207
HCl	5	153
	20	100
H_2SO_4	5-20	143-150

Table 2.1 Cooling Rate in aqueous solutions in the range of 880 to 730 °C of a Ø12.7 mm 0.95 C wt% steel probe. *Thermocouple at centre [27].

2.1.5.2 Electrical Processes

When a metal is heated at high temperature, electrical charge flow is induced from surface (electrons or ions). Due to the thermionic emission [43] [44] when the metal and the quenchant (electrolyte) come in contact, the negative ions of the solution are attracted by the positive charge of the metal, forming a double layer of electrical charges [45] [37] [46], see figure 2.10a. Since the liquid is dragged to the metal surface, stabilisation of vapour blanket becomes more difficult. For the case where cooling is related to electrical charges, the electrical conductivity plays a fundamental role. The range of concentrations where greater cooling rates take place in electrolytes correspond to the range of greater electrical conductivity [13]. Figure 2.10b shows the electrical conductivity of various solutions as function of concentration.

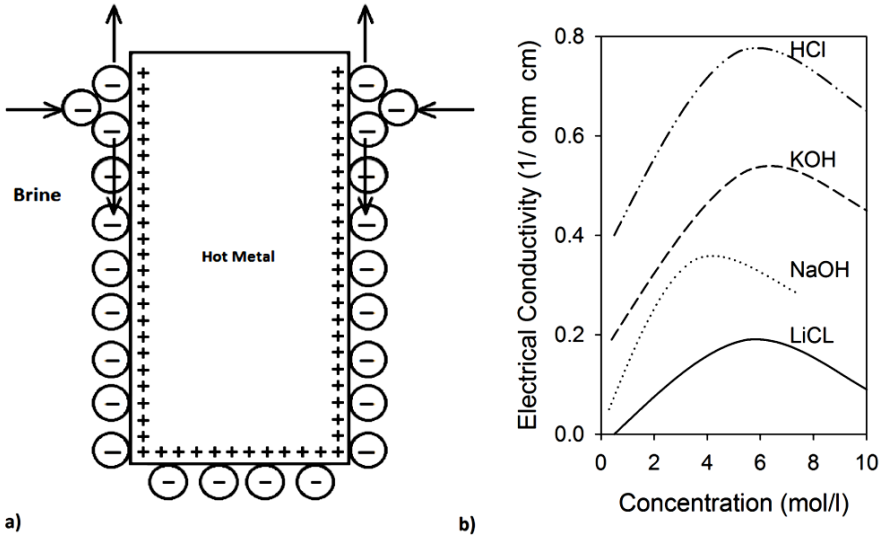

Figure 2.10 Schematic diagram of double electrical layer during quenching of steel in water salt solutions a) and the effect of salt concentration on electrical conductivity for various salts b) [37].

In figure 2.10a a diagram representation of the double electrical layer is shown. The negative ions surround the hot metal surface, also the surface tension of the solution is modified due to the accumulation of these negative ions [37]. The reduction of surface tension by the addition of surfactants improves the wettability and the heat transfer [47]. Qiao and Chandra [48], in their research on surfactants concluded that surfactants increase the contact area and promote the nucleate boiling stage, and that there is no evidence to correlate the reduction on the surface tension with the increase on the heat transfer. Further reading on the double electrical layer effect can be found in Ref. [37] [45].

2.1.5.3 Effect of salts concentration

Sodium chloride (NaCl) is the most common salt used as brine, since is easy to get it and at low cost. However NaCl could damage the pumping and agitation

systems due to its high potential to corrode steel [49]. Workpieces might also require further washing after quenching. Cooling curves of a nickel sample quenched in water and 10 % NaCl can are shown in figure 2.11 [50].

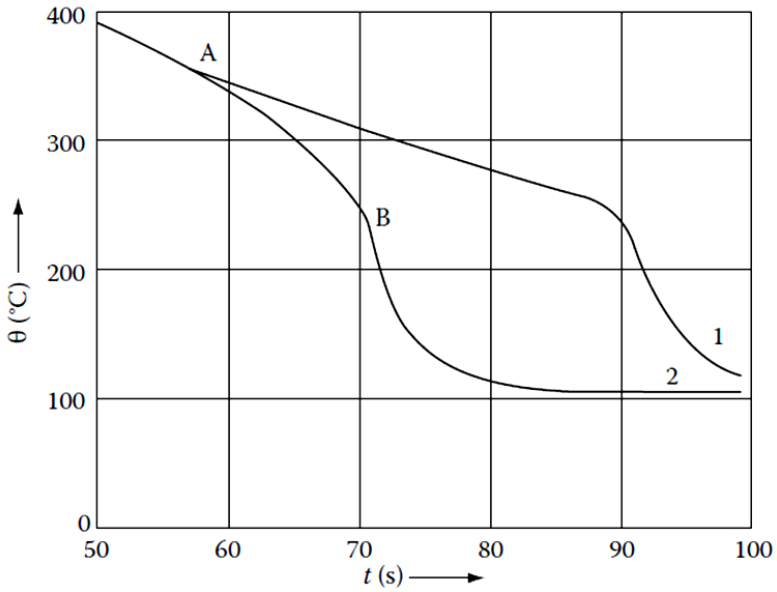

Figure 2.11 Cooling curves of a nickel probe quenched in water at 100°C (1) and in 10% NaCl aqueous solution at 101°C (2). *Ø16 mm [50].

Film boiling duration is considerably shorter with NaCl at 100°C; and at room temperature it may be eliminated. In figure 2.12, cooling rates of different concentrations of NaCl aqueous solution are shown. There is an optimal concentration of about 10-15 % which produce the most severe cooling, and with higher concentration up to 20 %, the cooling rate decrease considerably. Although the maximum cooling rate with 20 % and 1 % are in the range of 1200- 1300 °C/s for the experiment shown, there is a reduction in the film boiling duration with 20% compared with the curve of 1% in the range of 800-500°C.

It is worth to point out that such high cooling rates (higher than 750°C/s) when quenching in aqueous solutions, are usually obtained at the surface. The fact that these high values were obtained from a thermocouple at the centre of a 20 mm silver sphere, is possible due to its high conductivity. Thermal gradients within the probe are small, then core temperature may be assumed to be equal to the surface temperature during cooling.

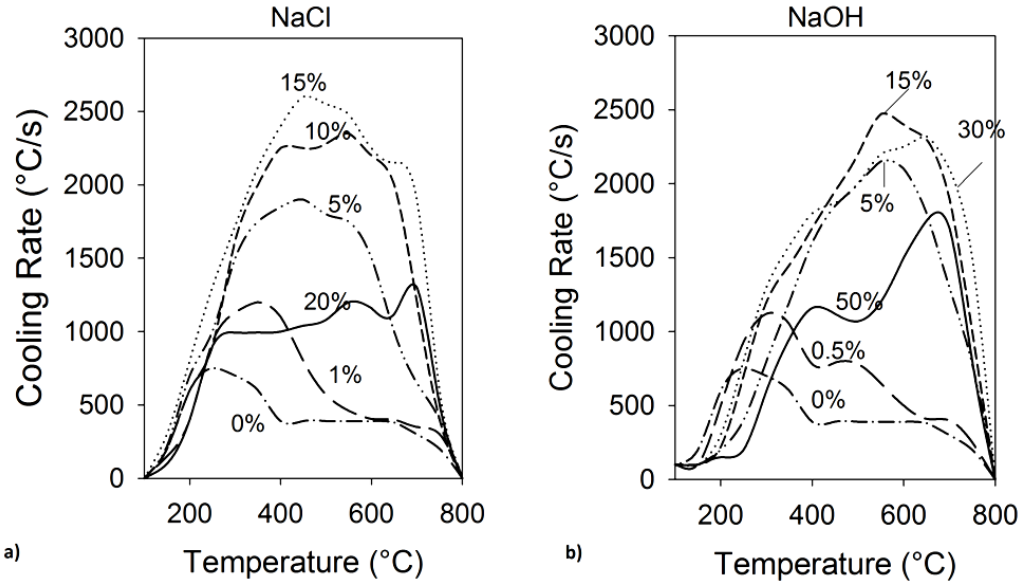

Figure 2.12 Effect of salt concentration on cooling capacity of NaCl a) and NaOH b) aqueous solutions. *Cooling rate as function of temperature at the centre of Ø20mm silver sphere [10].

One important aspect of brine quenching is the reduction of film boiling, which promotes a more uniform cooling. Although an increase in salts concentrations usually corresponds to a reduction in the film boiling duration (see figure 2.13), cooling rates usually reach a maximum followed by a decrease for concentrations higher than the optimal (Figure 2.12). The maximum cooling rate or optimal concentration depends on the salt or alkali used. Regarding the cooling capacity, from figure 2.12 can be concluded that 15% NaCl and 15% NaOH solution have similar cooling power. However, these results differ slightly from ref

[36] where it is reported that the highest HTC is reached with 10% for both brines, see figure 2.14. The HTC is strongly dependent on the part thickness [11] [34], thus many reported values differ even by one o two orders of magnitude for the same quenchant. In addition to the thickness of the sample, such scatter is also affected by the method of which the temperature was measured and by the calculation methodology itself. Some methods for HTC determination are addressed in references [51] [8] [41] [52] [53] [54] [11] [55] [56] [57] [58]. Standardisation of a methodology to determine the HTC is a current subject of the International Federation of Heat Treatment and Surface Engineering (IFHTSE).

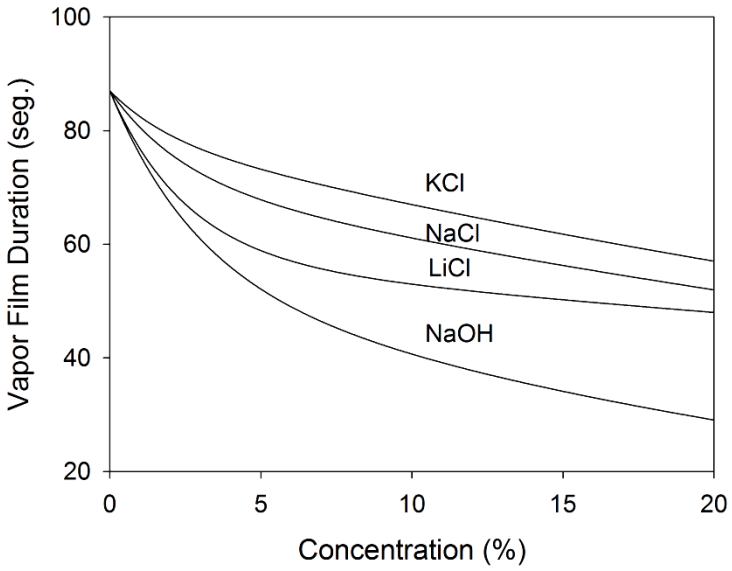

Figure 2.13 Film boiling duration as function of aqueous solution concentration. *Ø16 mm nickel probe. [50]

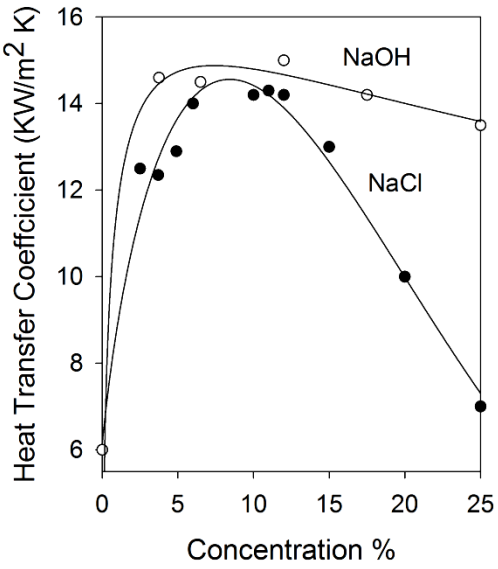

Figure 2.14 Effect of salt concentration on heat transfer coefficients of NaOH and NaCl aqueous solutions [36].

Calcium chloride ($CaCl_2$) is also used to reduce the vapour film boiling duration and increase the cooling severity [59] [29] [60]. Maximum cooling rates are obtained with concentrations within the range of 8-12%, and film boiling is eliminated [10].

Arai and Furuya [29] studied the effect of NaCl on the vapour film collapse by immersing half of a steel ball and maintaining the other half air cooled. By doing this, the vapour film stabilises as it would in larger parts, and the effect of salt concentration is clearly observed. Is important to note that with a full immersion, the duration of vapour film boiling may be considerable shorter. In figure 2.15 the cooling curves for different concentrations are shown, and is observed that an increase in concentration corresponds to a decrease of vapour film duration. Also the vapour collapse temperature is raised with salt addition, this means that the quenching temperature when liquid media actually wets the hot part is higher. With 40 wt% $NaCl_2$ vapour film is almost eliminated for this specific system (half ball

immersed). In addition, it was reported that with salt addition the vapour film thickness is reduced and the direct-contact frequency between the part and the quenchant increases as well as the collapsing temperature of vapour film.

It is worth to note that complete elimination of film boiling depends also on thickness of the quenched part and the volume of quenchant (due to agitation and local temperature increment). Therefore, all results presented are useful for comparison, and field tests are required in order to confirm whether or not film boiling could be suppressed for a specific application.

If a saturated solution is prepared (about 65% $CaCl_2$), the cooling capacity falls between water and oil, being able to quench medium-carbon steels while reducing cracking and distortion [59].

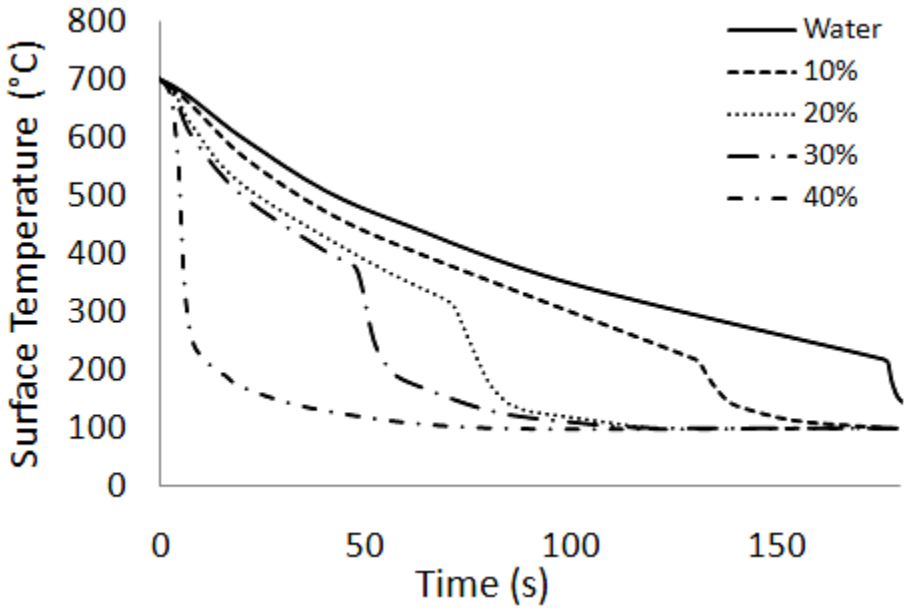

Figure 2.15 Effect of $CaCl_2$ concentration on cooling [29].

Magnesium chloride ($MgCl_2$) or bischofite has been used for specific application to increase the hardness depth. According to reference [31], cooling capacity of $CaCl_2$ solution is identical to the one of $MgCl_2$, although no concentrations were provided, it is assumed that the statement refers to the same concentrations. The main disadvantage of using $MgCl_2$ as brine is that it increases corrosion of metals by forming hydrochloric acid vapour through the reaction:

$$MgCl_2 + H_2O \leftrightarrow MgOHCl + HCl$$

Magnesium sulfate ($MgSO_4$) and sodium sulfate(Na_2SO_4) were reported in ref [30] to enhance the nucleate boiling heat transfer and the heat flux in spray quenching. These solutions exhibited superior cooling power than NaCl solution, with same concentration (0.06 mol/l), see figure 2.16. Authors noticed more foam formation for these sulfate solutions than for NaCl. In figure 2.17a the heat flux against $MgSO_4$ solute concentration is shown, and it can be observed that the optimal concentration is 0.2 mol/l and further additions as 0.4 mol/l reduces the heat transfer.

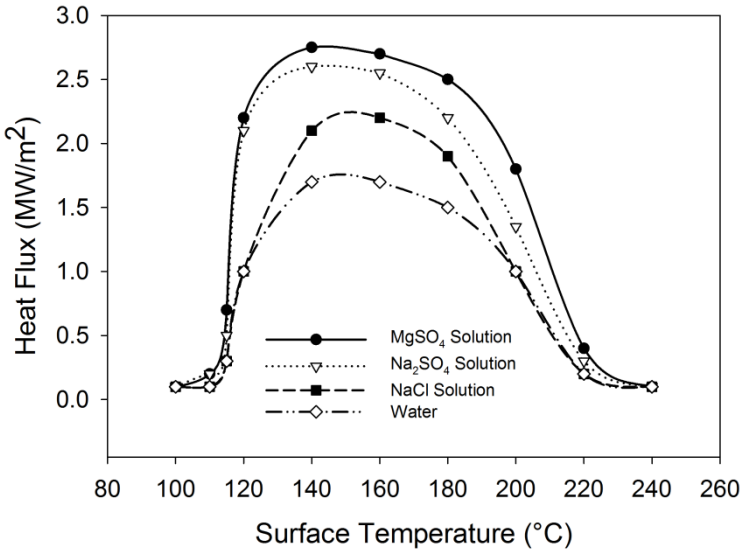

Figure 2.16 Effect of various salt solutions on the surface heat flux. *Concentration 0.06 mol/l [30].

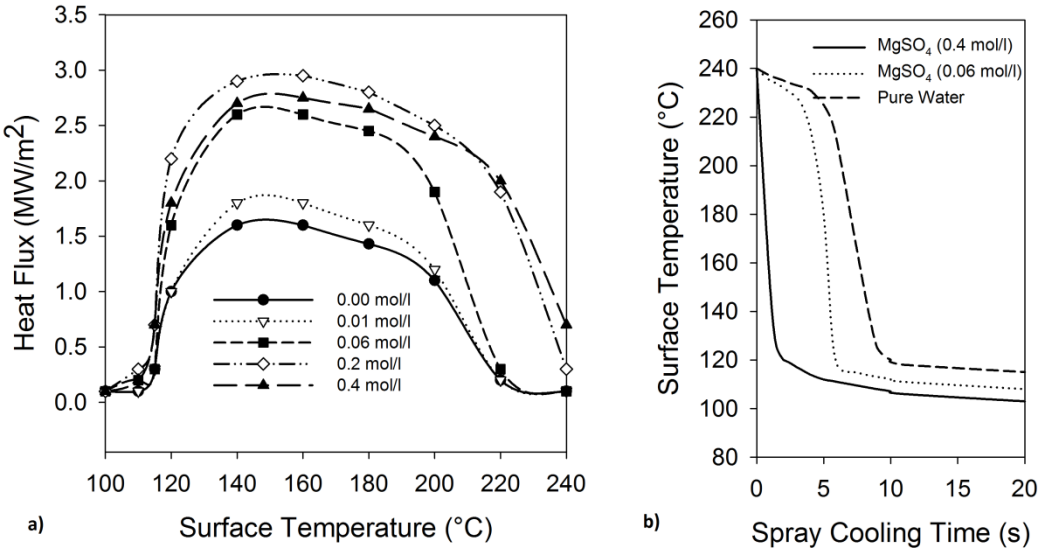

Figure 2.17 Effect of $MgSO_4$ concentration on surface heat flux a) and on the cooling curve b) [30].

From cooling curves of figure 2.17b it can be observed that with water spray and small concentrations of $MgSO_4$, the initial cooling is slow, authors attribute this to the vapour film formation and the rebounding of droplets after impact. With 0.06 mol/l the transition from film boiling to nucleate boiling was reduced and with 0.4 mol/l it was eliminated. After experiments, surface roughness was increased due to salt deposition on surface. Thus, this mechanism of adhesion could enhance the heat transfer due to an increase of superficial area.

Precaution must be taken in the selection of brine solutions for quenching, since the high severity of the quench may increase the cracking and distortion potential. Moreover, high concentration of salts promote corrosion in both the quenching system and the workpiece. There are organic salts which increase the cooling rate and at proper concentration act as corrosion inhibitors such as sodium nitrite ($NaNO_2$). The optimal concentration of the $NaNO_2$ to act as inhibitor differs among authors from 0.04 to 4 % **[61] [62] [63] [64] [65]**.

The heat transfer coefficient during quenching in aqueous solution can be as high as 300,000 W/m^2 K, according to experiments performed using a 5% water NaOH solution to quench a Ø38.1 mm sphere **[66]**.

2.1.6 Heat Transfer

Analysis of the heat transfer during quenching is of great relevance since a proper examination could lead to predict the optimal conditions of cooling rate and quenching times that would produce certain microstructure. The first step of the process is the acquisition of temperature data, which is commonly made by the use of embedded thermocouples within the part to be quenched.

During unsteady processes like quenching, it is difficult to get the surface temperature experimentally. Then, heat transfer analysis has to be done in order to obtain information of surface instantaneous temperature and therefore of convective heat transfer coefficients.

If a hot cylinder, long enough to be consider as semi-infinite (Length > 4 times Diameter), is suddenly quenched, the heat transfer will occur in one dimension, as shown in figure 2.18. The energy balance for convection is: [67]

$$-kA\frac{\partial T}{\partial x}\Big]_{surface} = hA\left(T_{surface} - T_{\infty}\right) \qquad \text{Eq. 2.1}$$

The finite-difference approximation is therefore:

$$-k\frac{\Delta y}{\Delta x}(T_{m+1} - T_m) = h\Delta y(T_{m+1} - T_{\infty}) \qquad \text{Eq. 2.2}$$

or

$$T_{m+1} = \frac{T_m + (h\Delta x/k)T_\infty}{1 + h\Delta x/k} \qquad \text{Eq. 2.3}$$

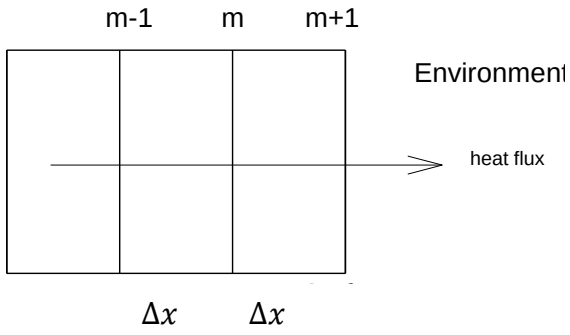

Figure 2.18 Nomenclature for numerical solution of unsteady-state conduction problem with convection boundary condition [67].

If the surface and inner temperatures are known the heat transfer coefficient is then calculated as:

$$h = -\frac{k}{\Delta x}\frac{(T_{m+1} - T_m)}{(T_{m+1} - T_\infty)} \qquad \text{Eq. 2.4}$$

where T_{m+1} is the surface temperature, T_m is a near surface temperature, x is the distance between the two positions and T_∞ is the quenchant's temperature **[67]**.

2.1.6.1 Calculation of surface temperature

The temperature of the surface is typically estimated from data acquired with thermocouples positioned inside the part. Usually, the surface temperature is calculated from a near surface temperature and the heat transfer coefficient. When heat transfers coefficients are not available for a specific quenching system

(geometry and quenchant), there is a need to evaluate the surface temperature using alternative methods, such as inverse problem methods. The inverse problem methods (IPM) are widely employed to estimate the heat transfer condition and their calculation is based on at least one temperature from an interior position of the sample and the thermo-physical properties of the material.

Although the use of the inverse problem analysis has been employed by many authors **[42] [68] [69] [70] [71] [72] [73]**, there is a considerable scatter of results among researchers. There are various valid solutions when solving and inverse problem (backwards), and the selection of thermophysical properties as function of temperature selected play an important role on this scattered results.

In addition to the intrinsic scatter of the Inverse Problem, the position, time response, insulation and wiring of thermocouple could strongly affect the final results.

The use of the called effective heat transfer coefficient described in reference **[39]**, is useful to compare the cooling severity of different quenchants or flow velocities. Since its calculation derives from the thermal history at the centre of a probe, the extrapolation of the surface temperature using the effective and the actual heat transfer coefficient may vary considerably. The effective HTC can be as 5 times as lower than the actual HTC. Thus, its practical application for surface temperature determination is limited only for quenchant comparison.

If it is considered that during unsteady state conduction the temperature distribution follows a parabolic trend in simple geometries, the surface temperature and the profile of temperature distribution can be estimated from thermocouple data at certain positions inside the part. A demonstration of the parabolic trend is addressed in section 3.3.4.

2.1.6.2 Determination of parabolic temperature distribution

During cooling of symmetric geometries, namely cylinders or prisms, the temperature distribution follows a parabolic shape from the geometric centre to any point on the surface if one dimensional heat transfer conditions are set (e.g at the middle length of infinite cylinders, bars) **[74]**. Thus, the temperature at the centre of the sample will be the maximum point of the parabola which is the vertex (The parabola opens downward during cooling).

If two points are known (x1, y1) and (x2,y2), then the parabola is symmetric with one axis, and being one of the points in the axis of symmetry, the equation of the parabola can be determined as shown in figure 2.19. Although the equation of a parabola ($y=ax^2+bx+c$) has three unknown constants, it can be solved with 2 equations because one point lies on the "y" - axis (temperature). Then the equation at this point x=0 is reduced to y=c. Furthermore, since the parabola is vertical and it is known that the vertex is on the axis, the slope of the derivative of the equations for the parabola must be zero at the vertical axis. Therefore, the value of the variable b is zero and the term can be neglected. The equation system is reduced to one unknown constant (a) and one equation, and can be solved by substituting the value of c for the equation of the (x2,y2) point. See Figure 2.19.

The equation at point $(\mathbf{x_1}, \mathbf{y_1})$ or $(\mathbf{x_1}, \mathbf{T_1})$, is:

$$\mathbf{T_1 = a{x_1}^2 + b x_1 + c} \qquad \text{Eq. 2.5}$$

where $\mathbf{x_1 = 0}$ then:

$$\mathbf{T_1 = c} \qquad \text{Eq. 2.6}$$

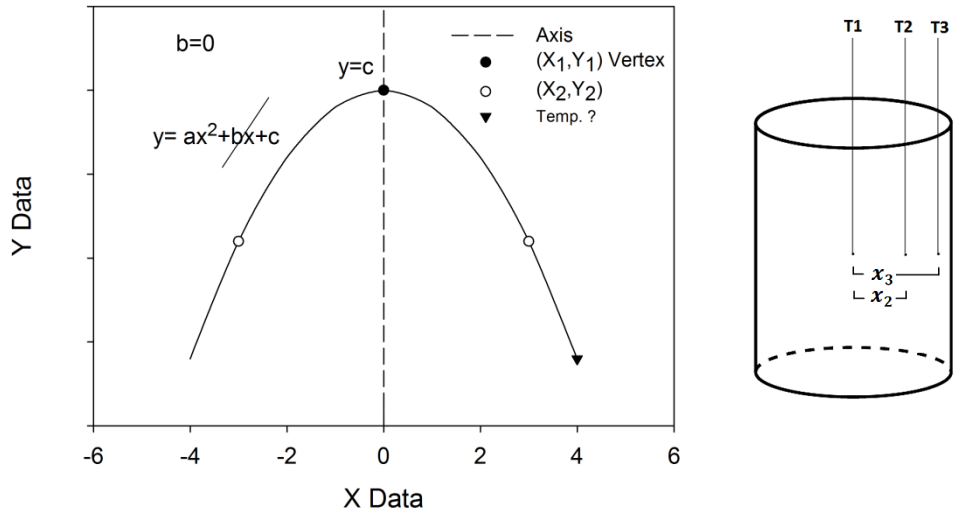

Figure 2.19 Schematic illustration of temperature distribution behaviour during quenching of a symmetric geometry. Y axis represents the temperature and X axis the radial position.

and since the slope at x=0 is zero, the derivative of eq. (1) is equal to zero:

$$\frac{\delta T}{\delta x} = ax + b = 0 \qquad \text{Eq. 2.7}$$

since x=0

$$\frac{\delta T}{\delta x} = b = 0 \qquad \text{Eq. 2.8}$$

substituting b and c on the equation of point (x_2, y_2) or (x_2, T_2):

$$T_2 = a{x_2}^2 + T_1 \qquad \text{Eq. 2.9}$$

Then a is obtained:

$$a = \frac{T_2 - T_1}{{x_2}^2} \qquad \text{Eq. 2.10}$$

where x is the radial position of the off-centre known temperature (T2).

The temperature at any *r* position $(\mathbf{x_r}, \mathbf{y_r})$ can be determined by:

$$\mathbf{T_r} = \mathbf{y_r} = \mathbf{a x_r^2} + \mathbf{c} \qquad \text{Eq. 2.11}$$

where r is the radial distance, then substituting a:

$$\mathbf{T_r} = (\mathbf{T_2} - \mathbf{T_1}) \left(\frac{\mathbf{x_r}}{\mathbf{x_2}}\right)^{\mathbf{2}} + \mathbf{T_1} \qquad \text{Eq. 2.12}$$

If three temperatures are known, the third thermocouple data can be used to validate the experiment, as demonstrated in the Section 3.3.4.

The method selected to obtain the temperature distribution is a simple procedure which uses only experimental data. Since there are not thermophysical properties involved in the calculation of the temperature distribution (unlike the inverse method analysis), the variation due to the proper selection of these temperature-dependent values, which are not available for many steel compositions, is avoided.

2.2 Martensitic transformation

The martensitic transformation is a displacive and diffusionless transformation in which the parent phase (austenite) undergoes a shear mechanism during cooling. Thus, the fcc austenite structure deforms due to shear on opposite sides of the plane and forms a body-centred tetragonal (bct) unit cell. This transformation ($\gamma \rightarrow \alpha'$) involves a volume expansion of 4% in a 1 wt% carbon steel. [75]. Figure 2.20 shows the effect of temperature and carbon content on the specific phase volume. According to this figure, a 5160 steel (0.58%C and Ms of 250°C) will experience an expansion of 3% due to the transformation ($\gamma \rightarrow \alpha'$).

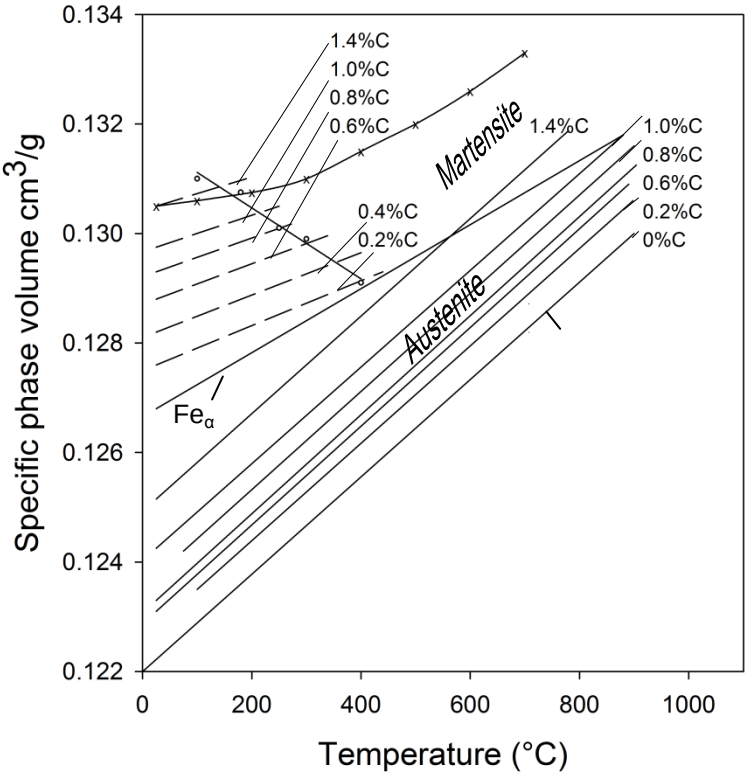

2.20 Variation of the specific phase volume of various steel transformation phases as a function of temperature [76]

This transformation occurs athermally, thus it does not depend on time but only on temperature. Therefore the fraction of martensite transformed depends only on the undercooling below the M_s. In the Koistenen and Marburguer equation the fraction of martensite is obtained from the Ms of the alloy and the temperature of the undercooling [77].

$$1 - V_{\propto'} = \exp\{\beta(\mathrm{M_s} - \mathrm{T_q})\} \qquad \text{Eq. 2.13}$$

where $\beta \cong -0.011$, $V_{\alpha'}$ is the fraction of martensite and T_q is the temperature at which the steel is cooled below M_s.

The Ms temperature depends mainly on carbon content, being inversely proportional to the M_s temperature (see Fig. 2.21). All alloying elements (except cobalt) lower the M_s temperature as well as carbon addition. There are a number of equations regarding the influence of alloying elements on the M_s temperature [78], being Andrews' equation the most common to predict the M_s temperature.

$$M_s(°C) = 539 - 423(\%C) - 30.4(\%Mn) \\ -17.7(\%Ni) - 12.1(\%Cr) - 7.5(\%Mo) \qquad \text{Eq. 2.14}$$

As can be seen in figure 2.21, for carbon steels containing more than 0.7 wt % C or for various alloyed steels, the martensite finish temperature does not appear on the diagram. This means that the transformation does not take place completely at room temperature. For these steels, certain amount of retained austenite is expected during quenching at room temperature, unless subzero cooling is employed [79]. Retained austenite is commonly undesired due to its low mechanical properties and low fatigue resistance [80].

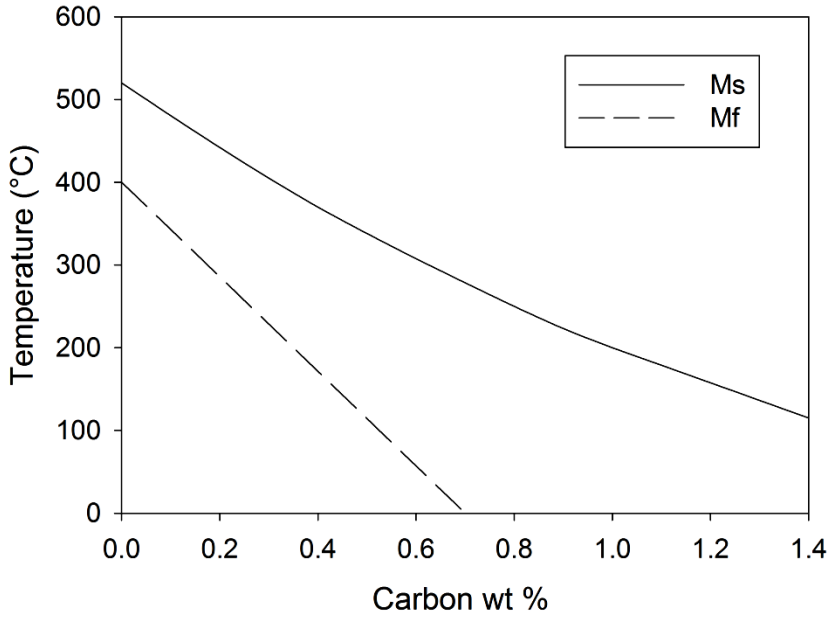

Figure 2.21 Effect of carbon content on M_s and M_f temperatures [77].

2.2.1 Martensite hardness

The hardness of the as-quenched martensite is much higher than that of ferrite or pearlite. Thus the maximum hardness obtainable in a carbon steel is achieved when the steel is in a fully martensitic structure. Martensite hardness is directly proportional to the carbon content (see figure 2.22). The high hardness is related to high mechanical properties, wear and fatigue resistance; therefore the quenching processes play an important role in order to obtain the desired amount of martensite.

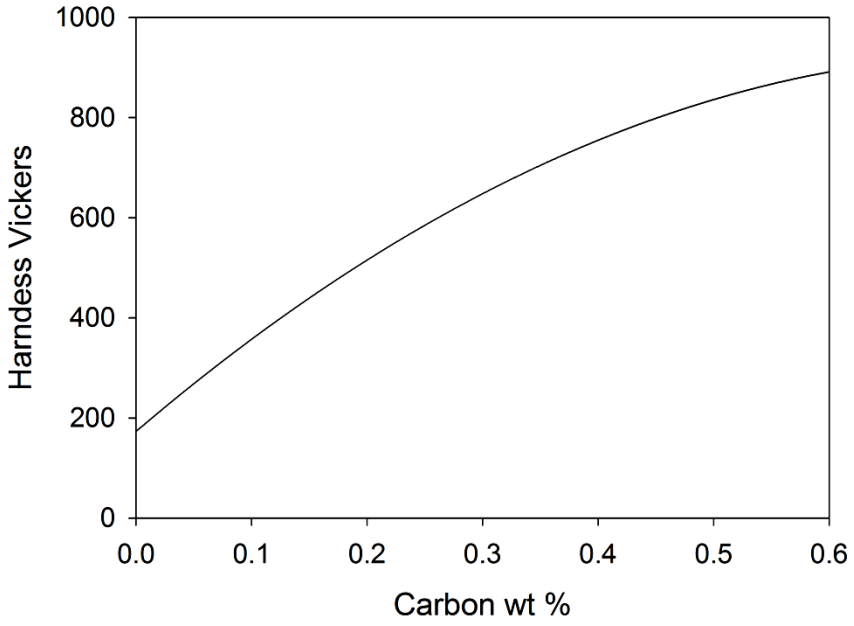

Figure 2.22 Martensite hardness as a function of carbon content [81]

Although a hard martensite is related to the steel strength, the as-quenched martensite is brittle and due to its low ductility always requires further tempering.

2.2.2 Hardenability

Hardenability is the ability of a steel to form martensite during quenching. Depending on geometry, thicker and thinner zones of the part will cool at different rates during quenching. These different cooling rates could usually produce mixed microstructures consisting of martensite, bainite and pearlite if the cross section is too large. The TTT and CCT diagrams are used in conjunction with the cooling curves of a process to predict the possible final microstructure and hardness. In conventional quenching, the target is to cool the part fast enough to avoid the bainite nose of the diagram and to obtain a fully martensitic structure if possible.

Alloying elements shift the TTT and CCT diagrams to the right and down, this is, alloying elements (except cobalt) make the steel more hardenable, then there is more time (or lower cooling rates) available to achieve a martensitic structure deeper in the steel part. Figures 2.23 and 2.24 show the TTT/CCT diagram and the Jominy curve of AISI 5160 steel (0.58 C, 0.26 Si, 0.885 Mn, 0.78 Cr, 0.01 Ni), respectively. The maximum as-quenched hardness attainable for this steel composition is 63 HRC (840 HV). Hardness can be reduced to a desired value by tempering after quenching.

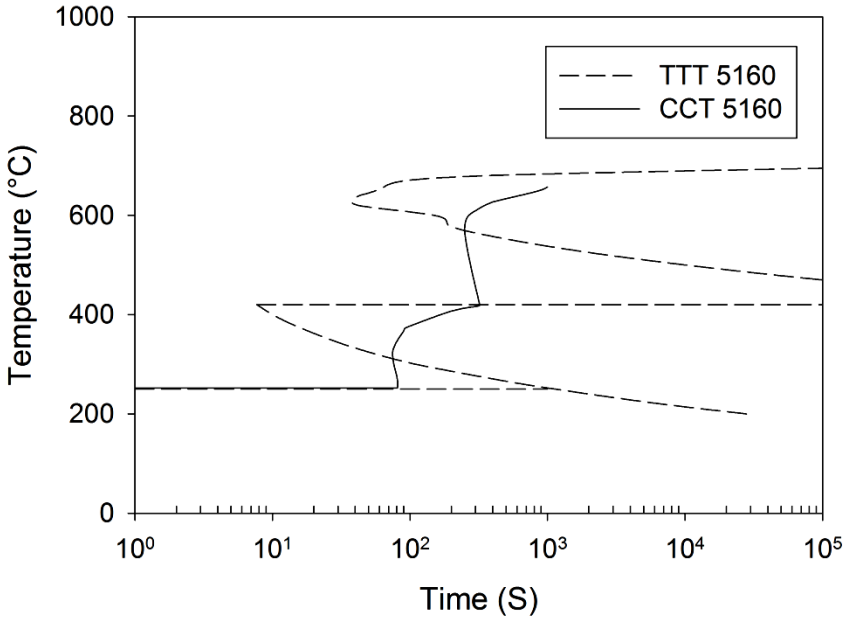

Figure 2.23 TTT and CCT diagrams of a 5160 steel (0.58 C, 0.26 Si, 0.885 Mn, 0.78 Cr, 0.01 Ni) generated using the Program MAP STEEL MUCG73 [82] [83]

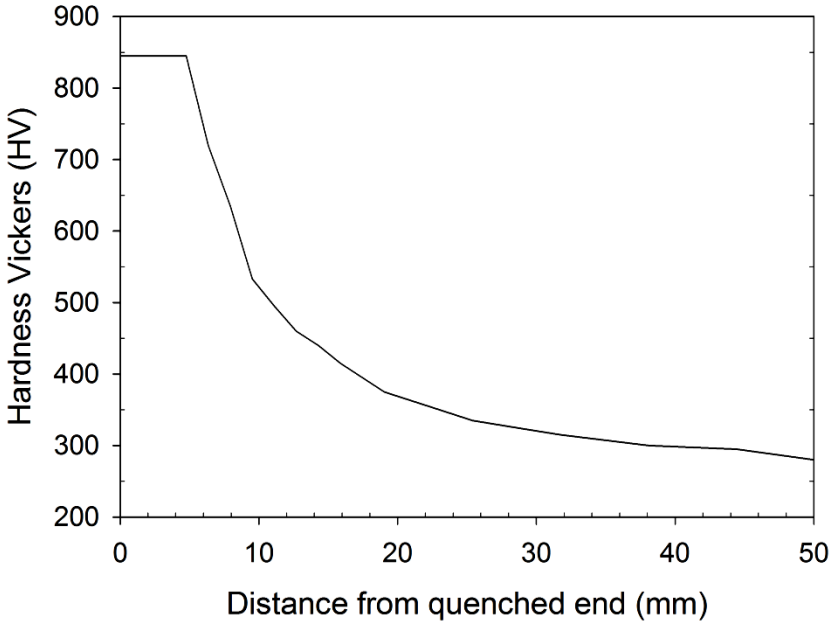

Figure 2.24 Jominy end-quench curve of a 5160 steel (0.58 C, 0.26 Si, 0.885 Mn, 0.78 Cr, 0.01 Ni) [84].

2.3 Tempering of steel

The heat treatment of martensite is called tempering, and results in a microstructure called tempered martensite, which is formed by fine carbides dispersed in martensite **[85]**. The objective of tempering is to reduce hardness and to increase the ductility while internal stresses are relieved.

Furthermore, during the tempering process, isothermal transformation of retained austenite to bainite usually takes place. In the case of the AISI 5160 steel the Mf is below room temperature, thus retained austenite cannot be avoided when quenching at room temperature. Interrupted quenching might result in higher levels of retained austenite since the lowest surface temperature is governed by the saturation temperature of the quenchant and the self-regulated thermal process, instead of the temperature of the quenchant.

Although the as-quenched martensite is very hard, is at the same time brittle for many applications. With a tempering process, toughness is increased at the expense of strength and hardness. When heated, the original body-centred tetragonal lattice of martensite becomes body centred cubic since cementite particles are expelled from the lattice **[86]**. These particles grow by coalescence and the higher the temperature the greater coalescence **[87]**.

It has been reported in references **[85,87,88,89]** that there is a range of tempering temperatures that produce a tempered martensite embrittlement (TME) from 250°C to 370°C. This phenomenon is related to the transformation of retained austenite to cementite among martensite laths **[85] [88]**. Embrittlement due to tempering is not limited to the TME temperature range, at higher temperatures from 450-600°C a different mechanism of embrittlement takes place. At this temperatures, the impurities segregate at grain boundaries. However, this type of embrittlement is only observed in heavy parts since impurity segregation requires long times. Furthermore, high temperature embrittlement can be reversed by heating the part above 600°C and quenching it in water.

2.3.1 Effect of tempering on fatigue resistance

The fatigue resistance of steel is strongly affected by the tempering temperature. Htun **[90]** reported the effect of tempering temperature on the fatigue resistance and mechanical properties of AISI-5155 spring steel (0.52C-0.61Cr-0.7Mn-0.21Si). Results showed that the maximum yield strength is reached when tempering at 450°C for 1 hr and the maximum endurance limit of 900 MPa (fatigue limit) was obtained at a tempering temperature of 400°C for 1hr. Unfortunately the results in ref. **[90]** do not show the S-N fatigue curves, nor specify whether the endurance limit versus tempering temperature plot is displayed using the stress range or the stress amplitude. Since the experiments were carried out using rotating bending fatigue tester with similar probe dimensions that the present work it is assumed that the endurance limit might refers to the stress range.

Haftirman **[91]** reported the effect of tempering temperature of a 0.3C-0.2Si-0.5Mn-0.2Cr-1.6Ni steel ranging from 100 to 600°C on the rotating bending fatigue resistance. Results showed that the highest fatigue strength for this alloy was achieved by tempering at 300°C.

The effect of tempering temperature and time on the mechanical properties, toughness and fatigue resistance strongly depends on the alloying elements concentration. Thus, is important to study this effect for the specific alloy of interest, instead of using the available data from different alloys.

2.4 Decarburisation

Another important concern when heat treating is the amount of decarburisation allowed for the alloy treated. Although the use of inert atmospheres in furnaces is a common method to minimize decarburisation, slight partial decarburisation is present in most industrial processes since large parts are overheated above austenitizing temperature of the alloys in order to compensate the heat loses when transporting from furnaces to further processes, and they may be exposed to oxygen.

The term decarburisation is related to failure and low strength of steel. It has been reported the detrimental effect of decarburisation on the fatigue resistance of steel **[92] [93]**.

The reduction of strength is related to the switch of the CCT and TTT diagrams for the decarburised layer. This is, a steel part is oil-quenched to avoid high thermal gradients and to promote the martensite transformation to occur at similar times at surface and core, thus reducing the amount of tensile residual stresses. When the surface layer is completely decarburised the transformation does not take place at the surface, and when the expansion due to the core's transformation takes place, the ferrite superficial layer cracks.

In the case of a partially decarburised steel, the Ms temperature is increased as the carbon content is reduced, as presented in figure 2.21. Therefore, the surface layer would transform to martensite first although the thermal gradients from surface to core are maintained low (oil quench). The surface transforms and expands while the core is still shrinking, when the Ms is reached at the core, the expansion is restrained by the hard and brittle martensite shell already formed at the surface. The surface layer is exposed to high tensile stresses which can remain as tensile residual stresses or crack the material.

2.4.1 Effect of decarburisation on TTT and CCT diagrams

Since the carbon content plays a key role on the hardenability of steels, its diffusion out of the steel switch the TTT and CCT diagrams. Figure 2.25 shows how the 5160 steel TTT diagram would be modified if carbon is released from nominal 0.58%C to 0.4 and 0.3 %C. The Ms is increased from 250°C to 336°C and 376°C respectively and the bainite nose is shifted to the left. From figure 2.26 it can be noticed that the time to reach the bainite nose is reduced from 100 seconds for 0.58%C to only 10 seconds for 0.3%C.

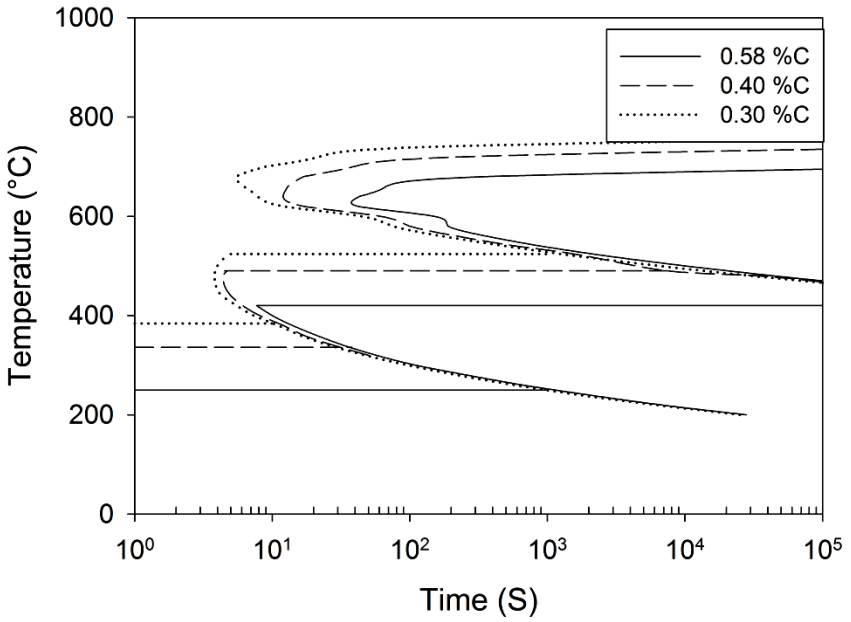

Figure 2.25 TTT diagram of a 5160 steel, 0.58%C, 0.88%Mn, 0.78%Cr, 0.26 %Si (solid line), and the effect of partial decarburisation (0.3%C and 0.4%C) [82].

Is worth to mention that this modification of the CCT diagram would be valid for the partially decarburised layer, as the diagram for the core remains as the original.

Thus, a profile of carbon content would lead to a complex set of CCT diagrams instead of a single CCT.

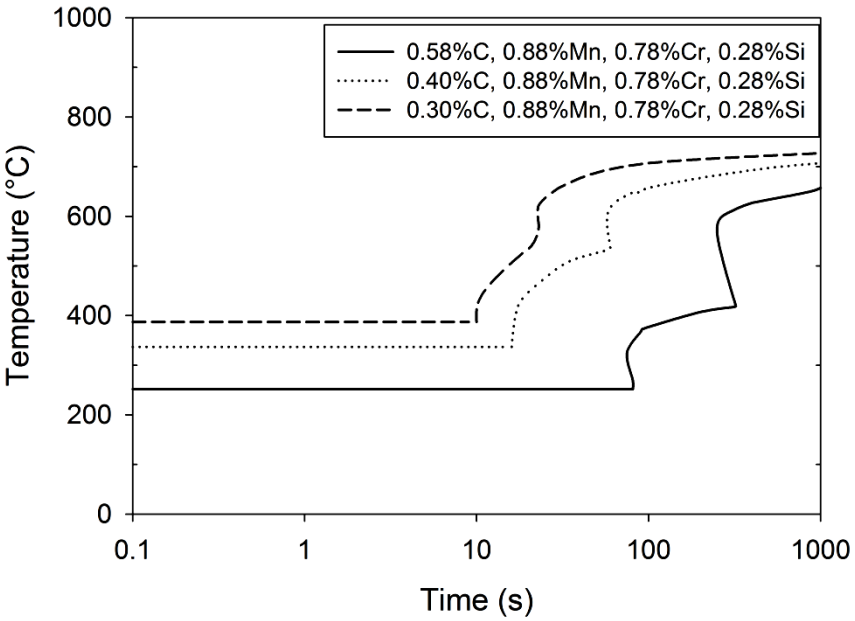

Figure 2.26 CCT diagram of a 5160 steel, 0.58%C, 0.88%Mn, 0.78%Cr, 0.26 %Si (solid line), and the effect of partial decarburisation (0.3%C and 0.4%C) [83].

Since the practical application of the intensive quenching is limited to parts greater than 50 mm in thickness due to the high thermal gradients required, a partial decarburisation might be beneficial for small sections. Since highly enough thermal gradients are difficult to produce in these tiny sections, a modification of the surface Ms temperature would simulate an increase on the thermal gradient. The transformation at surface will take place before than it would on a non-decarburised part, letting the quenching to be interrupted when the core is still austenitic and fulfil the IQ theory. In addition, the Mf temperature is also raised and, therefore, the amount of retained austenite is reduced when the quenching is interrupted.

2.5 Fatigue

The fatigue resistance of materials dependens on factors such as the type and magnitude of loading. The most accepted type of experiments are based on constant load or constant deformation. By using a constant load the real stress increases exponentially as the crack grows, while the constant deformation test could provide more information since the force required to deform the material certain displacement is reduced as the crack grows and the remnant cross-section decreases. Information of the type of fatigue experiments and influence of loading modes can be found in references **[94] [95]**

Typical S-N (stress- number of cycles) or Wöhler curves are displayed as nominal stress. This is, whether the stress range or amplitude are plotted, they refer to the initial nominal stress without considering the presence of a crack. The stress range (ΔS) is the difference between the maximum and the minimum stresses, and the stress amplitude (S_a)is half the stress range, see following equation.

$$\boldsymbol{S_a = \frac{\Delta S}{2} = \frac{S_{max} - S_{min}}{2}} \qquad \text{Eq. 2.15}$$

The mean stress influences the fatigue limit, a mean stress equal to zero is a fully reversed condition where the maximum and minimum stresses are of the same magnitude but different sign, this is the case of rotating bending fatigue. In addition to the stress relationships, the "*R*" parameter is commonly used among researchers to compare the severity of experiments. The "*R*" parameter is the ratio of minimum to maximum stress. A *"R"* value of 1 means that there is no fatigue and instead a static loading, and a value of -1 means a fully reversed condition.

$$\boldsymbol{S_m = \frac{S_{min}+S_{max}}{2}} \qquad \text{Eq. 2.16}$$

$$\boldsymbol{R = \frac{S_{min}}{S_{max}}} \qquad \text{Eq. 2.17}$$

2.5.1 Stress Concentrators

In addition to loading conditions, notches cause a detrimental effect on the fatigue limit. Notches, or better known as stress concentrators, increase the local strain and stress. The effect of the notch on local stress depends on the geometry and the root radius, and is represented by the stress concentrator factor K_t. The mathematical solution for the nominal stress of a bending shaft is:

$$\sigma_{nom} = \frac{M(y)}{I} = \frac{32\,M}{\pi d^3} \qquad \text{Eq. 2.18}$$

where M(y) is the bending moment at the surface, I is the inertia moment, d is the smaller diameter of the shaft. The stress concentrator factor K_t of a shaft with fillet under bending is obtained from figure 2.27 [94].

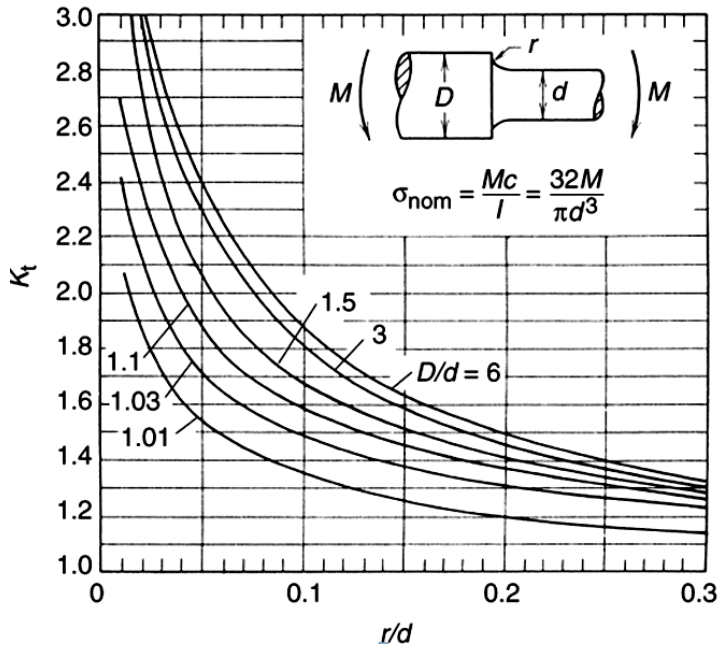

Figure 2.27 Stress concentration factors for a stepped-shaft bending [94].

Since the fatigue limit is reduced with the presence of a notch, a ratio of the smooth to the notched fatigue strengths called the fatigue notch factor K_f is used to correlate the real effect of the notch on fatigue strength [96].

$$K_f = \frac{\text{Smooth Fatigue strength}}{\text{Notched fatigue strength}} \qquad \text{Eq. 2.19}$$

The fatigue notch factor is a function of material properties and notch geometry. Neuber [96] proposed the following equation for the notch factor for R=-1 loading:

$$K_f = 1 + \frac{K_t - 1}{1 + \sqrt{\rho / r}} \qquad \text{Eq. 2.20}$$

where r is the radius at the notch root and ρ is a characteristic length that depends on material properties. The values of ρ for steel as function of the tensile strength are shown in figure 2.28. More information regarding the notch factors can be found in references [94] [96].

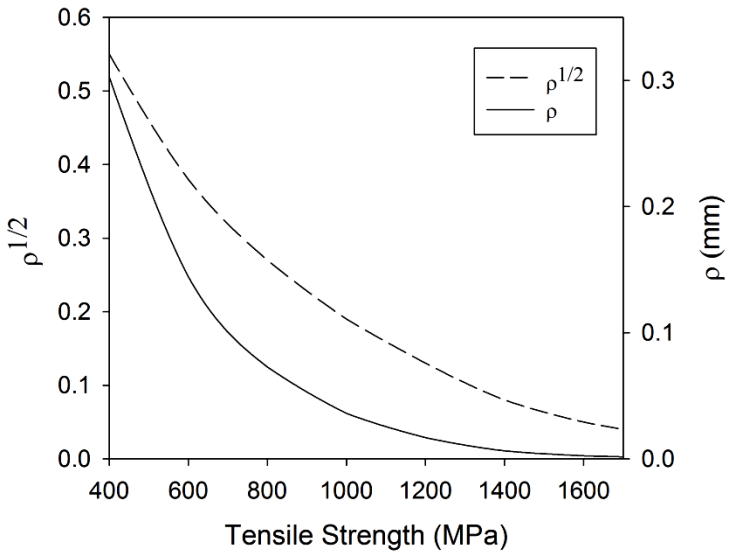

Figure 2.28 Neuber's material characteristic length √ρ versus tensile strength for steel alloys [96].

Another approach to determine the K_f is the Peterson's criteria [96] which is defined as:

$$K_f = 1 + \frac{K_t - 1}{1 + a/r} \quad \text{Eq. 2.21}$$

where *a* (mm) is a material characteristic length defined as function of S_u (MPa) as:

$$a = 0.0254 \left(\frac{2070}{S_u}\right)^{1.8} \quad \text{Eq. 2.22}$$

A comparison between both criteria is shown in Table 2.2 for an ultimate tensile strength range from 1200 to 1600 MPA and a K_t= 2.2

S_u (MPa)	Neuber K_f	Peterson K_f
1200	2.0086	2.02
1400	2.0505	2.06
1600	2.1457	2.09

Table 2.2 Comparison between Neuber's and Peterson's fatigue notch factors for a K_t of 2.2.

The notch influences how the cracking mechanisms take place. Depending on its severity, the fatigue fractures might look as the schematic of figure 2.29 shows [95]. From this figure and the notch factors of Table 2.2, the type of fracture that could be expected for rotating bending are the ones corresponding to the sharp notch drawings shown in the red square.

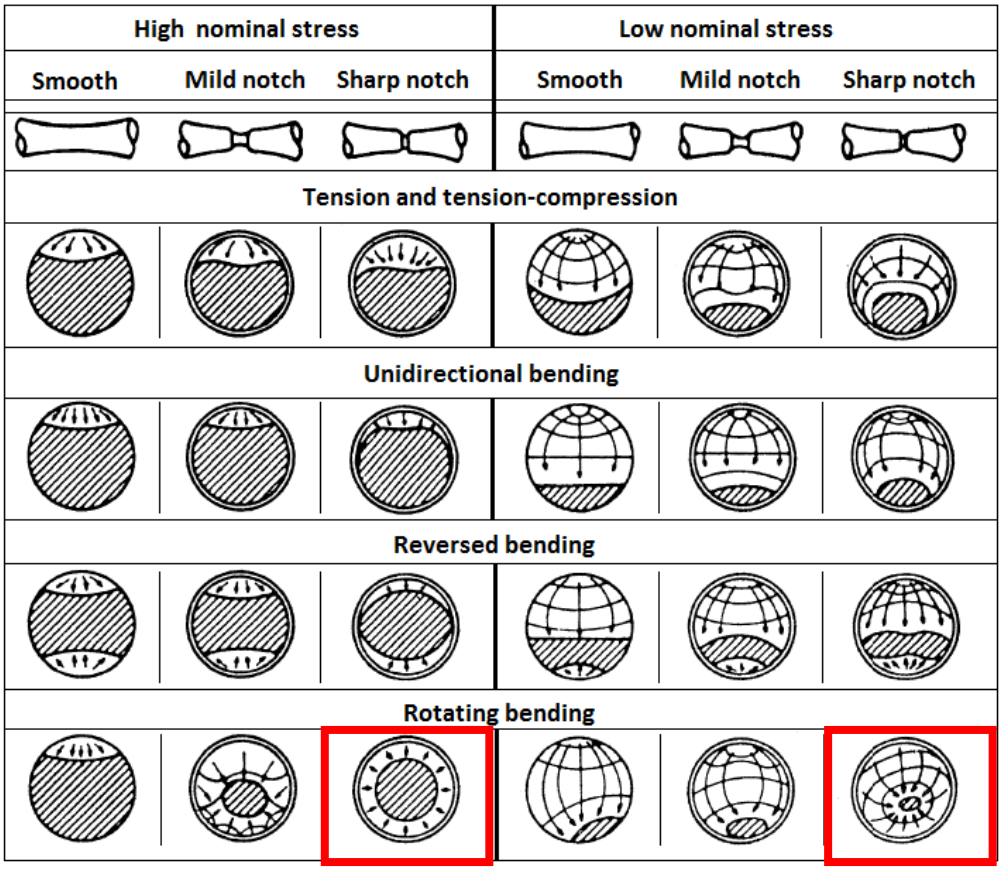

Figure 2.29 Schematic fatigue fractures [95].

CHAPTER 3

EXPERIMENTAL PROCEDURE

3.1 Introduction

The experimental procedure was carried out mainly in three stages, which are listed below:

1. Fatigue equipment design and development
2. Heat treatment development
3. Fatigue experiments

3.2 Fatigue testing equipment

A rotating bending fatigue testing equipment was designed and built for the present work in order to specially address the crack nucleation and propagation phenomena, as well as to be able to perform experiments at frequencies in the range 10-40 Hz, although in this work a constant frequency of 20 Hz was employed in all the tests.

Common fatigue experiments are based on either constant load or constant deformation [95]. Usually, for constant load experiments the information obtained is limited to the cycles of final fracture. While for constant deformation more information can be acquired like crack growth characteristics, although instrumentation is expensive.

The first stage of the experimental procedure consisted in the design of a rotating bending fatigue with high sensitivity to crack nucleation and propagation. For this purpose a cantilever bending fatigue with constant deflection was selected as an adequate configuration, since in this probe type the surface undergoes the maximum stress and the superficial effects of decarburisation and hardened layer can be evaluated.

The fatigue tester incorporates a motor and a drive, a inductive sensor, a digital counter, two house ball bearings, shaft, sample holder (collet) and an endless screw loading frame system with a digital force gauge mounted, as can be seen in figures 3.1 and 3.2. This loading system allows to maintain a constant deflection through the experiment and at the same time to record the load decrement, which is related to the cracking of the specimen. The applied load is displayed and logged to a computer. Data is acquired at a rate of 10 samples/second.

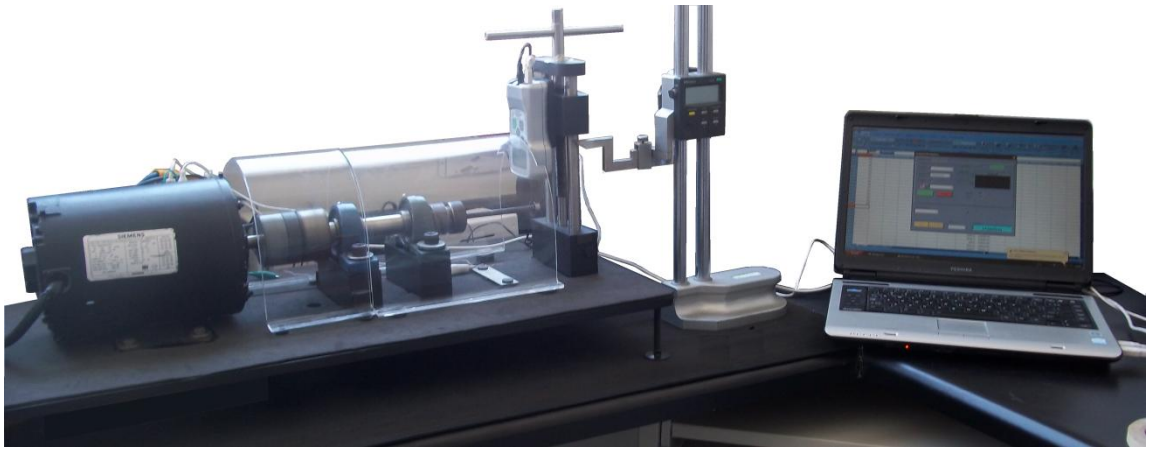

Figure 3.1 Rotating bending fatigue tester.

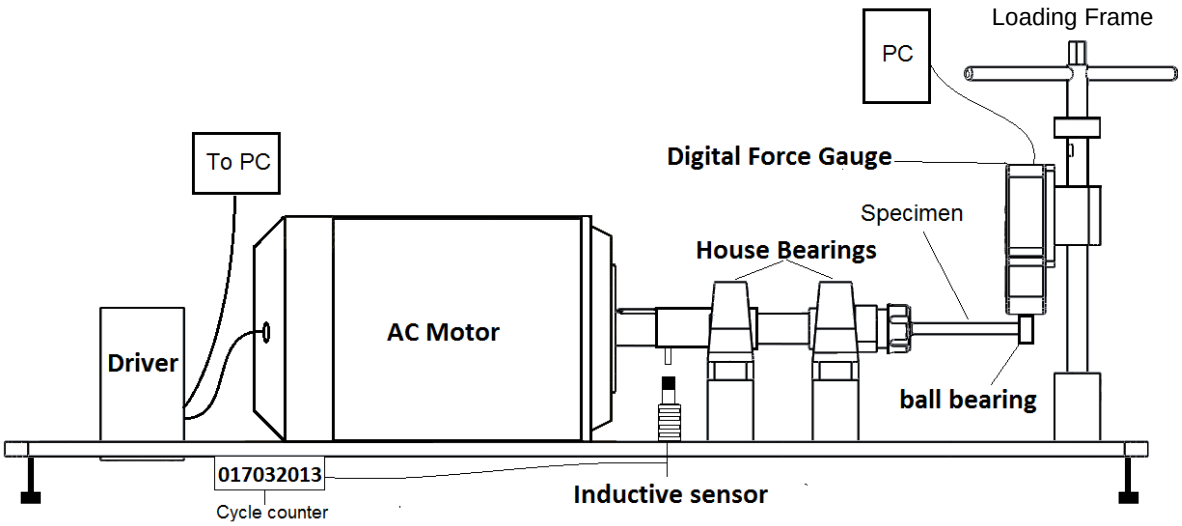

Figure 3.2 Schematic diagram of the fatigue tester.

Fatigue specimens were fabricated with a sharp notch with a radius of 0.4 mm. Figure 3.3 shows the geometry of the fatigue specimens.

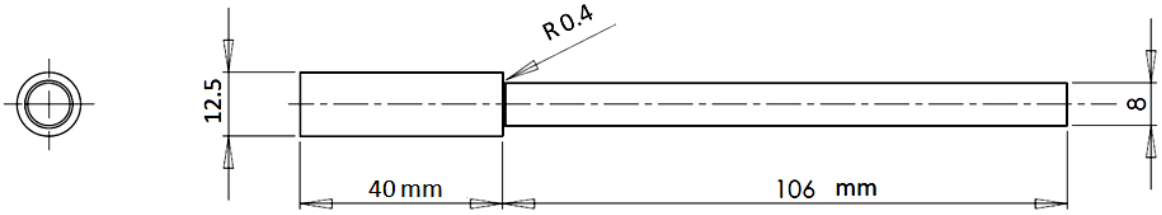

Figure 3.3 Geometry of the fatigue specimens.

3.2.1 Stress concentrator analysis

According to figure 2.27 of stress concentraion of notches, and using the multiplying factor due to moment caused by the load, the initial nominal stress was calculated. The relationship applied-load against stress is shown in figure 3.4.

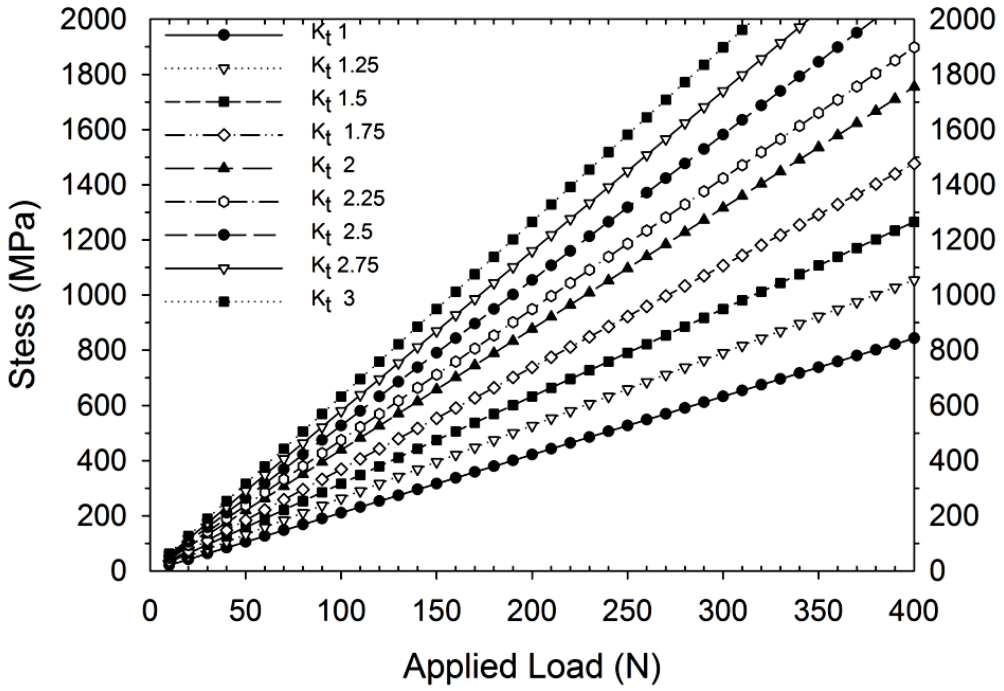

Figure 3.4 Stress at notch as function of applied load and stress concentrator factor K_t for fatigue specimens.

3.3 Heat Treatment

Once the geometry of the samples was specified for the fatigue experiments, the heat treatment required tailored development. Usually the intensive quenching theory involves samples thicker than 50 mm because of the thermal gradients possibly attainable. Since the geometry of the samples (Ø8 mm) is not suitable for obtaining sufficient thermal gradients between the core and surface, even with a severe quenching, the hypothesis stated was that with a partial decarburisation the Ms at the surface would be higher and therefore could increase the time difference from transformation at the surface and that at the core, emulating the thermal conditions of a thicker part.

3.3.1 Decarburisation

Decarburisation of 5160 steel was studied at different temperatures (850, 900, 950, 1000°C) and different times (15, 30, 45 and 60 min). Cylinders of 12 mm in diameter and 15 mm high were heated in an electrical resistance furnace (20 x 20 x 20 cm) in air. In order to ensure the same atmosphere condition for all conditions and to avoid oxygen from entering into the furnace, experiments were carried out one at a time for each temperature and time. After heating and holding time, samples were quenched in water. Samples were cut and a micro-hardness profile of the cross section was measured.

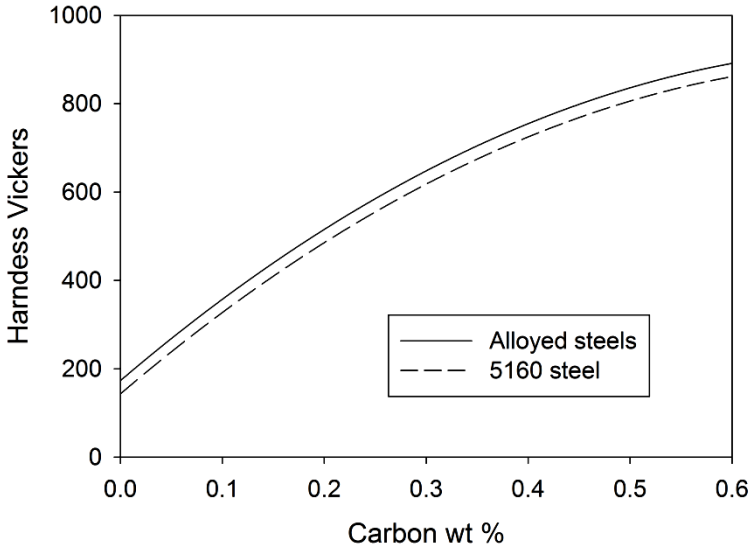

Figure 3.5 Martensite hardness as function of carbon content commonly found in steels [81] and experimentally obtained in this work for AISI 5160.

Using the data reported by Krauss [81] and Bhadeshia [77] (figure 2.13), a correlation between martensite hardness and carbon content was obtained. Using the hardness value from completely decarburised zones, and the hardness of martensite without decarburisation (0.58%C), it was found a 30 HV offset between the reported data for alloyed steels and the values of the 5160 alloy (see figure 3.5) in the whole range of carbon concentrations.

3.3.2 Quenchant Severity

In order to increase the cooling power of water and also to decrease the full film boiling stage characteristic of pure water, $NaNO_2$ was used as additive Ref [97]. However, there is not literature available regarding the effect of NaNO2 concentration on the heat transfer modes and cooling severity, thus a proper study was necessary. Using various concentrations and geometries, cooling curves were experimentally obtained to determine the optimal concentration and heat transfer condition for the desired heat treatment.

3.3.3 Cooling Curves acquisition

A standard INCONEL 600 probe according the ASTM D-6200 [40] was used to obtain the cooling curves of the aqueous solutions (see Figure 3.6). This type of cylindrical probe (Ø12.5 mm x 60 mm) uses a single thermocouple located at the geometric centre and is useful for determination of the cooling characteristics of quenchants for comparison. However for an accurate heat transfer determination, the temperature near the surface must be known.

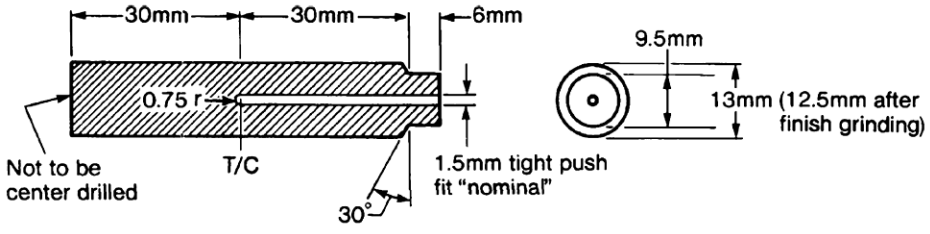

Figure 3.6 Geometry of the standard INCONEL 600 probe [40]

It is commonly assumed that a diameter/length ratio of at least (1:4) will adequately minimise the end cooling effects and then the heat transfer calculation can be treated as a one-dimensional (1D) problem which simplifies the computations. Therefore, cylindrical probes of three diameters (8, 12 and 20 mm) of an AISI 304 austenitic stainless steel were fabricated. The length of the probes were 5 times greater than their diameters (40, 60 and 100 mm respectively). Three Ø1mm blind holes were drilled by electro discharge machining up to the mid length in each of the probes. The holes were drilled at the centre, mid-radius and at 1 mm from the surface in each probe size. A schematic illustration of the Ø12 mm probe is shown in Figure 3.7. The dimensional relationship shown in this figure was maintained for the Ø8 and Ø20 mm probes.

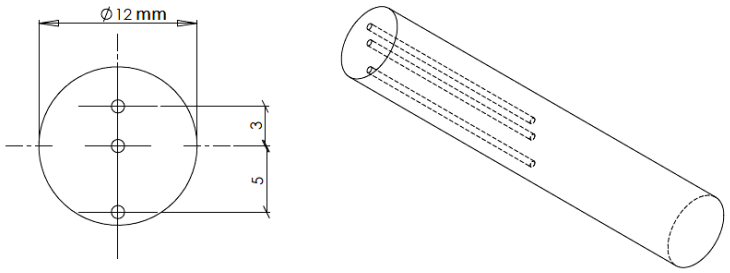

Figure 3.7 Geometry of the Ø12 mm and 60mm length AISI 304 austenitic stainless steel probe, showing thermocouple positions.

Three ungrounded Ø1 mm Type-K thermocouples were inserted into the holes. The holes were machined in order to tightly adjust the thermocouples, see figure 3.8. A small amount of graphite powder was deposited into the holes before thermocouple insertion to ensure good contact between the thermocouple and the probe and to fix the thermocouple. After thermocouple placement, a ceramic coating was used to seal the holes to prevent the quenchant from entering the holes.

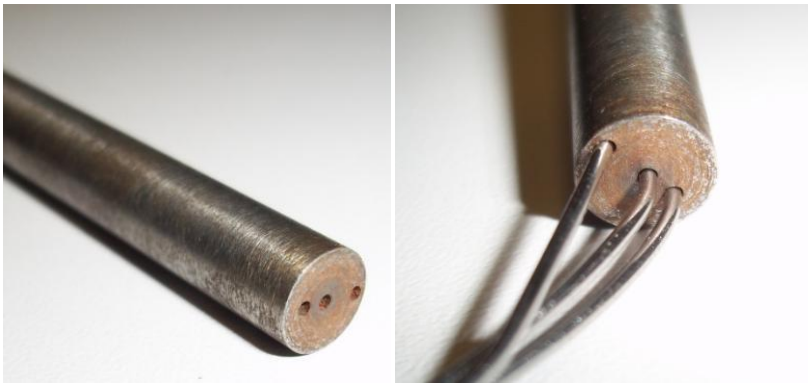

Figure 3.8 AISI 304 stainless steel bar of 8 mm in diameter and 40 mm in length

The thermocouples were differentially connected (negative terminals were connected to different channels not to ground) using a 75 KΩ resistor between the negative terminal and ground to have a good reference. Data was acquired at a sampling frequency of 100 Hz and was smoothed for the cooling rate and heat transfer calculations.

For cooling curves generation, probes were heated to 900°C and then quenched. A glass reservoir, 200 mm diameter and 500 mm high, with 12 litres of quenchant was used. All experiments were performed at quenchant temperature of 25-27 °C. The temperature of the quenchant was measured. A localised quenchant temperature increase (from 25 to 45°C) was recorded near surface in the upper zones of the liquid. After each experiment the quenchant was mixed and no considerable temperature increase was measured (≈1 to 2 °C).

3.3.3.1 Cooling Curve Smoothing

In order to manage the data for cooling rate and heat transfer calculations, cooling curves were smoothed. An accurate method to get the global approximation over the time range is the employment of a cubic spline algorithm

[98] [20] [99]. In figure 3.9. the plot of the original data acquired at 100 Hz against the smoothed data is shown.

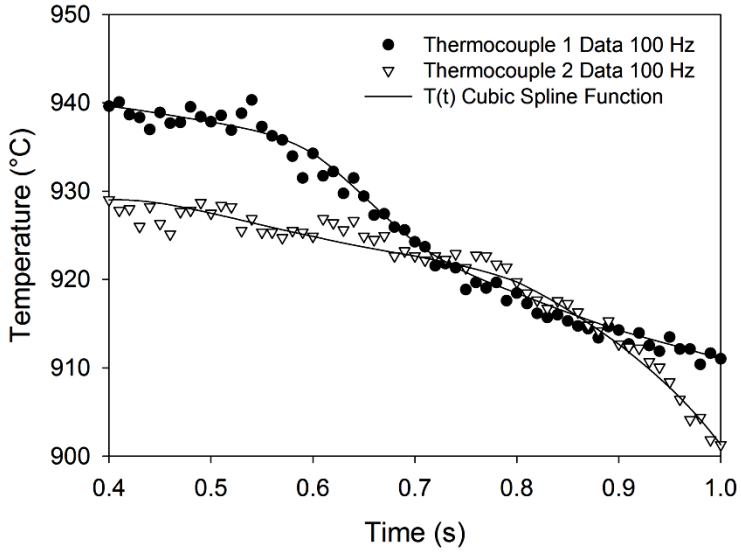

Figure 3.9 Original thermocouple data 100 Hz and smoothed data with a cubic spline function T(t).

3.3.4 Validation of the method for determining the temperature distribution

Demonstration of the parabolic temperature distribution explained in section 2.1.5.2 was validated with a set of experiments using samples with different diameters and cooling media. In Table 3.1 the set of experiments is shown.

Table 3.1 Experiments to validate the parabolic temperature distribution.

Experiment ID	Probe type	Diameter or thickness	Quenchant
I	cylinder	8 mm	Water
II	cylinder	8 mm	9% Brine
III	cylinder	8 mm	Oil
IV	cylinder	12 mm	1% Brine
V	square bar	20 mm	Water

Cooling curves were acquired at three positions within the samples during quenching. As indicated in figures 2.19 and 3.7, T1 is the temperature at the centre and T3 is the near-surface thermocouple position. These two experimental data points were used in equation 2.12 to determine the temperatures at surface and at position T2'. The calculated temperature T2' was compared to the experimentally obtained temperature T2. The error percentage and temperature difference between the experimental and the calculated points were analyzed.

Figures 3.10 to 3.14 show the cooling curves and the plot of the error and temperature difference for experiments I to V respectively. From figure 3.10 of the experiment I (8mm bar water quench), it is noted that although the T2' (calculated) do not overlap the T2 (measured) curve, the maximum temperature difference was at the beginning of the cooling where its influence on the error is less due to the high temperatures. The average error percentage during the 3 first seconds where the curve is more deviated was 4.14% and the average ΔT was 17°C. After 3 seconds the curves almost overlapped and the average temperature difference was only 4°C. Note that the calculated surface temperature curve drops to 101°C (boiling point of water) and except for the small reheating obtained due to the internal heat source, is maintained close to the boiling temperature. This phenomena is commonly observed and is known as the self- regulated thermal processes, where the surface temperature does not cool below this point until sufficient heat has been extracted from the entire mass [100]. This phenomena is also explained since no agitation was present during quenching, therefore, localised heating of the quenchant up to its boiling point occurs. Thus the surface becomes surrounded by quenchant at the same temperature until the natural convection of the fluid mixes the hot with the cooler bulk fluid.

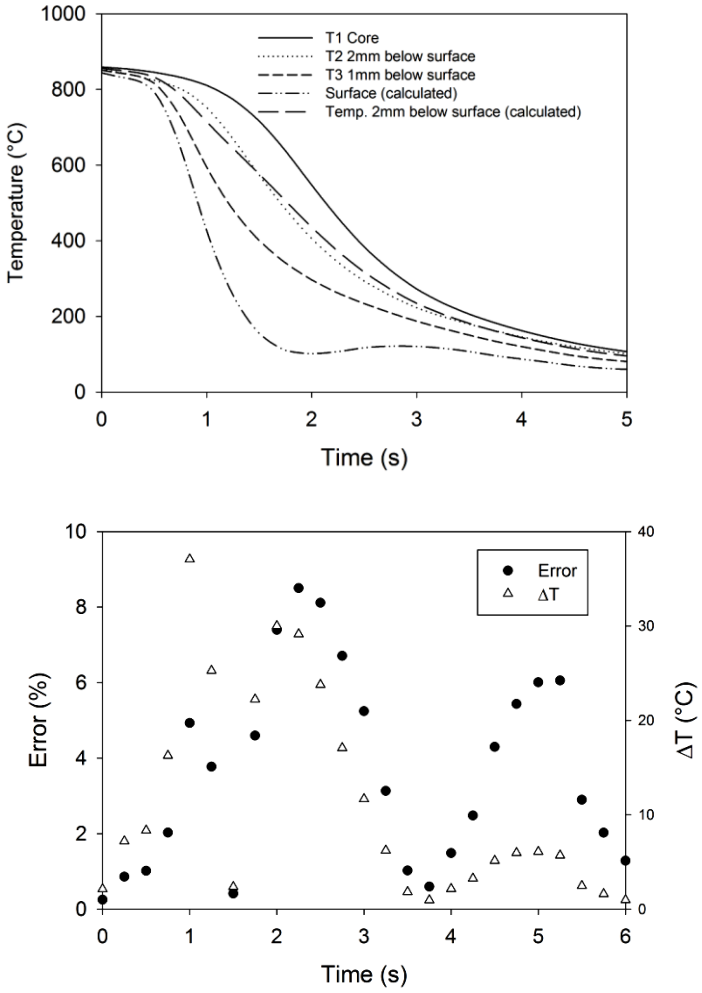

Figure 3.10 Water quench of an AISI 304 stainless steel bar of 8 mm in diameter, showing 3 thermocouples data and temperatures at surface and 2 mm below surface calculated from T1 and T3 (upper figure) and error between measured and calculated temperature as function of time.

In the 2nd experiment (II), the same bar was quenched in water with the addition of salts to promote a more aggressive cooling. The boiling point of water is increased by salt addition and thus the surface temperature is expected to decrease and maintain above 100°C. From figure 3.11, it can be observed that during the first three seconds, the error reaches a maximum of only 4% and maximum ΔT of 16°C. The error and ΔT averages for the first three seconds were 2.15% and 8°C

respectively. From immersion time of 3 to 5 seconds, the averages were 0.7% error and 0.7°C of difference. The calculated surface temperature decreased to 133°C due to the higher boiling temperature of the aqueous solution.

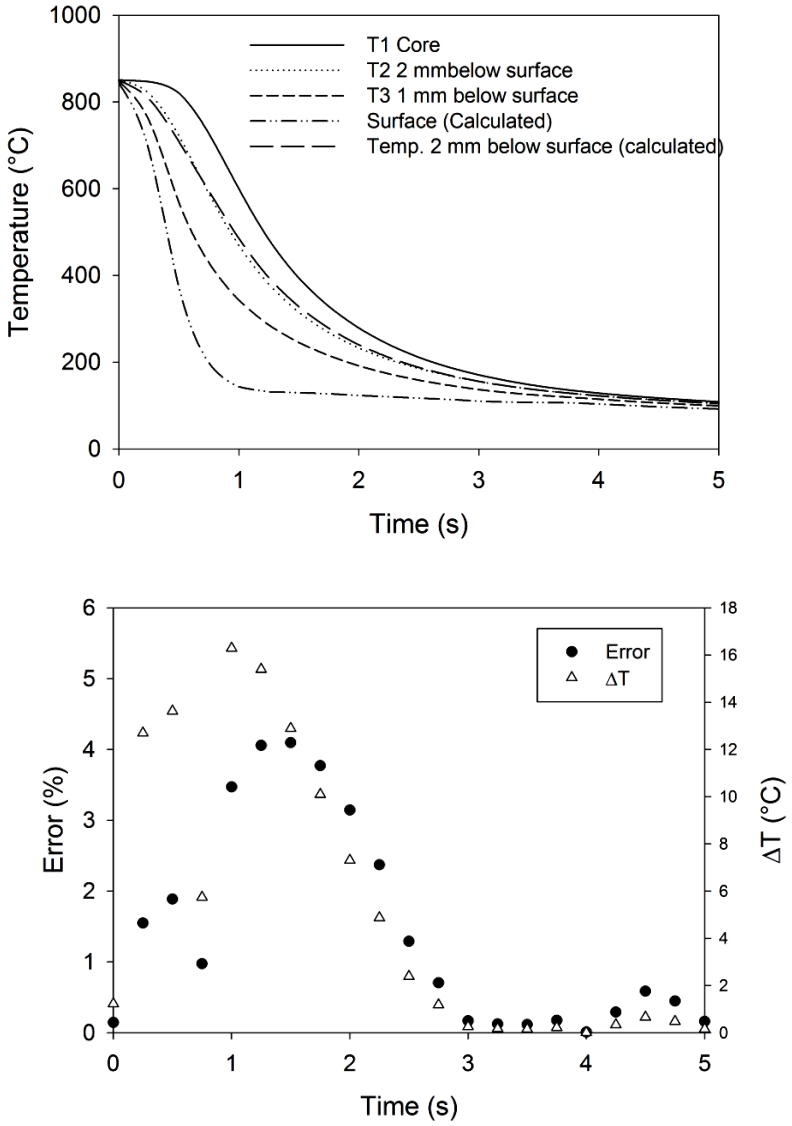

Figure 3.11 Brine quench (9% $NaNO_2$) of an AISI 304 stainless steel bar of 8 mm in diameter, showing 3 thermocouples data; and temperatures at surface and 2 mm below surface calculated from T1 and T3 a) and error between measured and calculated temperature as function of time.

The cooling curves of experiment III, corresponding to the 8 mm bar quenched in canola oil, are shown in figure 3.12. The heat extraction of the oil is considerably lower than water and the salt solution (brine), thus low thermal gradients between surface and centre were present. Since the temperature difference between the thermocouples was low, the error when calculating the temperature distribution was low. The average of error percentage was 1.8% and the ΔT average was 0.8°C. For most of the time range, the error between the experimental and the calculated temperatures was less than 5°C.

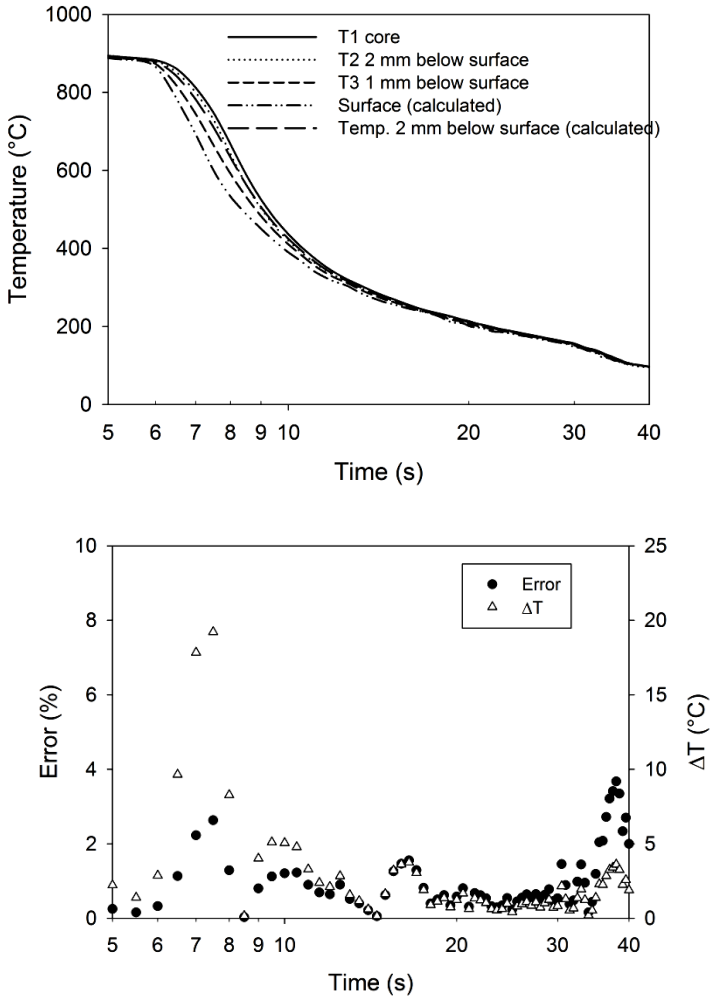

Figure 3.12 Vegetable oil quench of an AISI 304 stainless steel bar of 8 mm in diameter, showing 3 thermocouples data and temperatures at surface and 2 mm below surface calculated from T1 and T3 a) and error between measured and calculated temperature as a function of time .

Increasing the size of the sample did not produce any change of the parabolic distribution of temperature as can be seen in figure 3.13 of experiment IV, where a 12 mm bar was quenched in 1% brine. The calculated temperature from the parabolic approach overlapped the experimental curve. The temperature difference remained below 14°C. On average, the error was 6.6% and the ΔT 9°C.

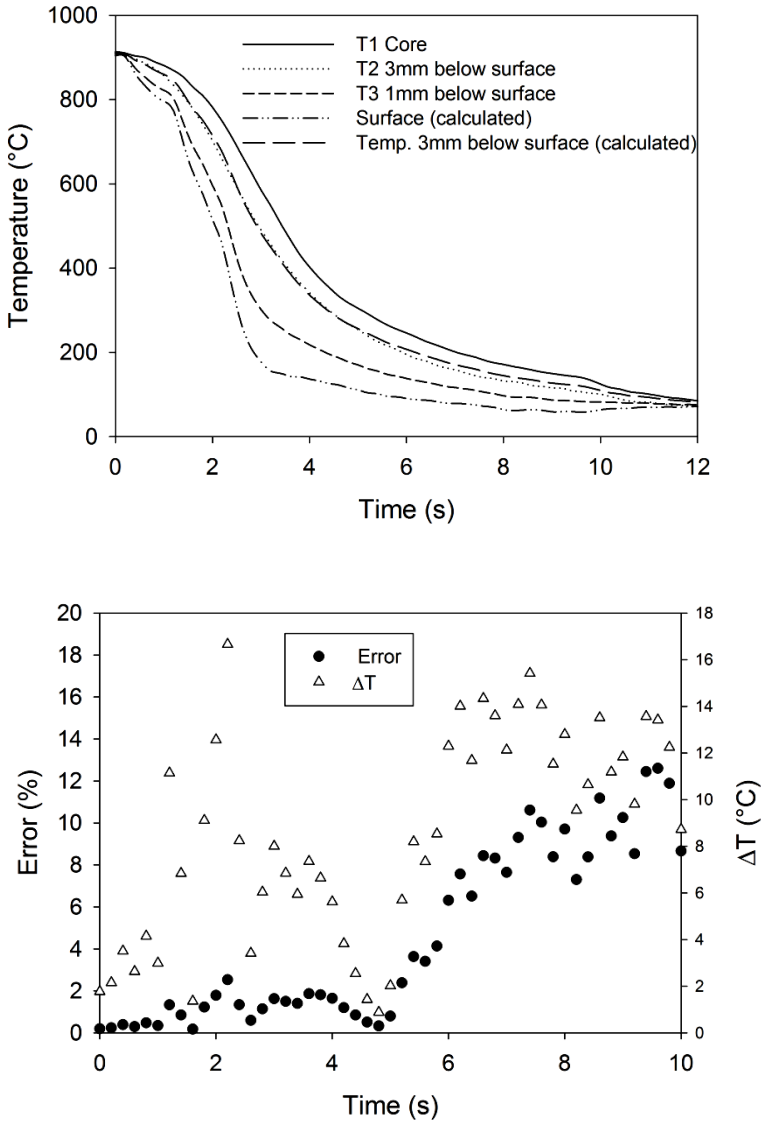

Figure 3.13 Brine quench (1% $NaNO_2$) of an AISI 304 stainless steel bar of 12 mm in diameter, showing 3 thermocouples data; and temperatures at surface and 3 mm below surface calculated from T1 and T3 a) and error between measured and calculated temperature as a function of time.

In addition to semi-infinite cylinders where one dimensional heat transfer conditions are assumed, a square bar was also instrumented. The long square bar exhibits one dimensional heat transfer at the mid-thickness as it would be on a slab.

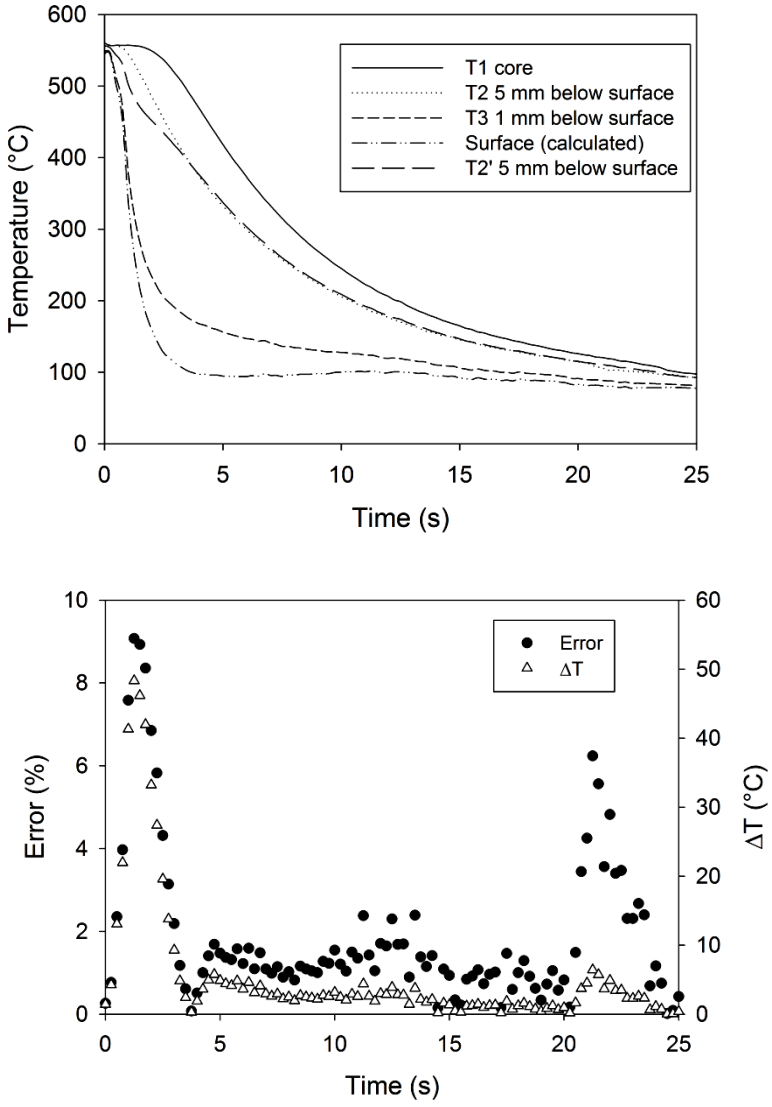

Figure 3.14 Water quench of an AISI 304 stainless steel square bar of 20 x 20 mm in cross section, showing 3 thermocouples data; and temperatures at surface and 5 mm below surface calculated from T1 and T3 a) and error between measured and calculated temperature as a function of time .

For experiment V, the square bar was heated to 550°C and water quenched, see figure 3.14. At the beginning of the cooling, a stable vapour blanket formed around the probe. The calculated T2' temperature does not match the experimental data initially. This may be due to the presence of this low heat transfer stage. After the first 3 seconds, where the error reaches 10% and the ΔT reaches a relatively high value of 50°C, the calculated data overlapped the experimental curve with a divergence of 4.5°C. Geometry of the square bar is shown in figure 3.15.

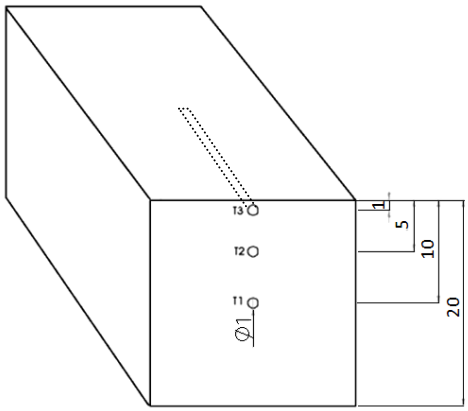

Figure 3.15 Geometry of the 20x20x100 mm AISI 304 austenitic stainless steel square bar, showing thermocouple positions.

In addition to these experiments to validate the temperature distribution calculated by a parabolic approach, experimental data from reference [68] were used to estimate the surface temperature and the heat transfer coefficient for the cooling curve of figure 3.16. Three cooling curves and a heat transfer coefficient obtained through the gradient method were presented in Ref. [68]. Using the parabolic approach, the surface temperature and subsurface temperature were estimated, then heat flux and heat transfer coefficient were determined. From Figure 3.16 b it can be noticed that the HTC calculated from the parabolic approach is similar to the originally calculated through the gradient method. Both have a maximum of 3200-3300 W/m^2 K. The shift to the left might be due to the fact that the HTC is plotted using the calculated surface temperature.

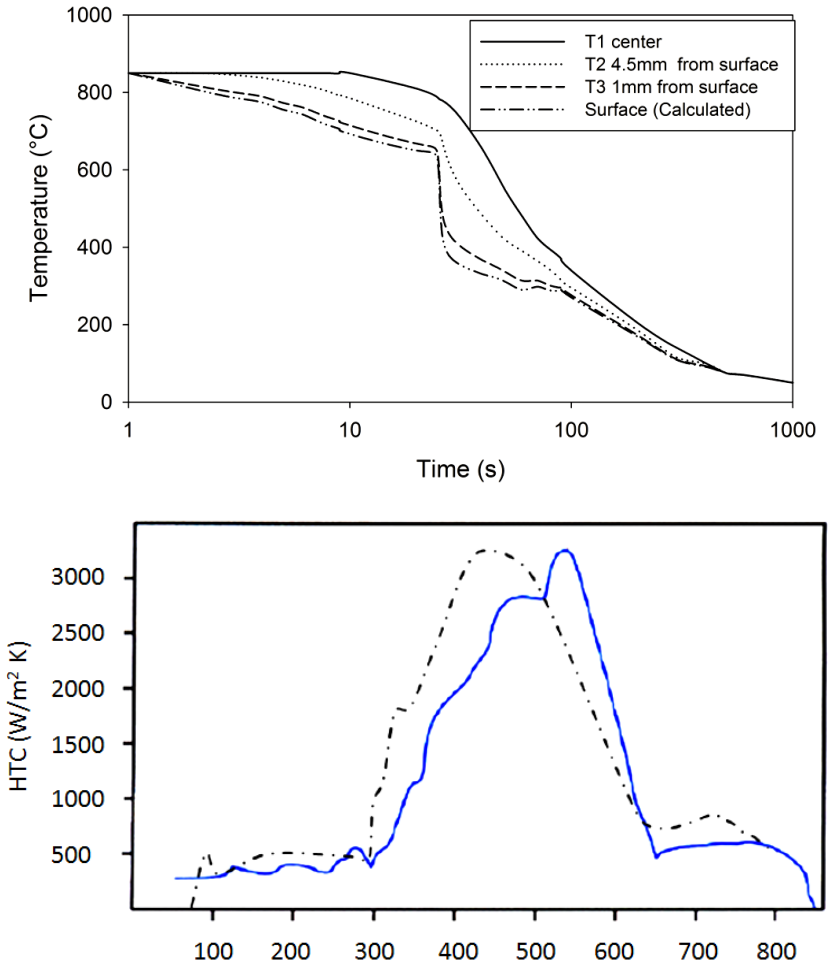

Figure 3.16 Cooling curves of a Ø50mm bar quenched in slow oil taken from reference [68] and the surface temperature calculated by the method proposed in this work a). HTC reported by ref. [68] (solid line) and HTC calculated by the proposed method (dashed line) b).

3.3.5 Tempering

Once the quenchant concentration and quenching times to produce the desired microstructure were determined, the steel samples required further tempering.

Immediately after the interruption of quenching the samples were rapidly transferred into a furnace to temper the hardened surface and to prevent the core temperature to decrease below the Ms temperature and to get hardened.

The tempering temperature is a key element on the final microstructure and properties. In order to analyse the effect of the tempering temperature on hardness, three cylindrical samples of 8 mm in diameter and 30 mm length were heated to 950 °C and quenched in water to produce a fully martensitic microstructure (same as for the decarburisation analysis). Afterwards, samples were tempered at different temperatures (150, 200, 250, 350, 450 and 550°C) for 60 minutes. Subsequently, a microhardness profile of the cross section was obtained from the surface to the core. By analysing the partially decarburised zone, it was then possible to establish the effect of tempering temperature on hardness. Samples were characterised by scanning electron microscopy.

3.3.6 Quenching of 5160 steel samples

Fatigue specimens were preheated at 400°C for 10 minutes prior to be placed in the austenitizing furnace to reduce distortion due to high heating rates. Then they were austenitized, quenched and tempered. Selection of austenitizing temperature, quenchant, quenching time and austenitizing temperature are discussed in detail in Chapter 4.

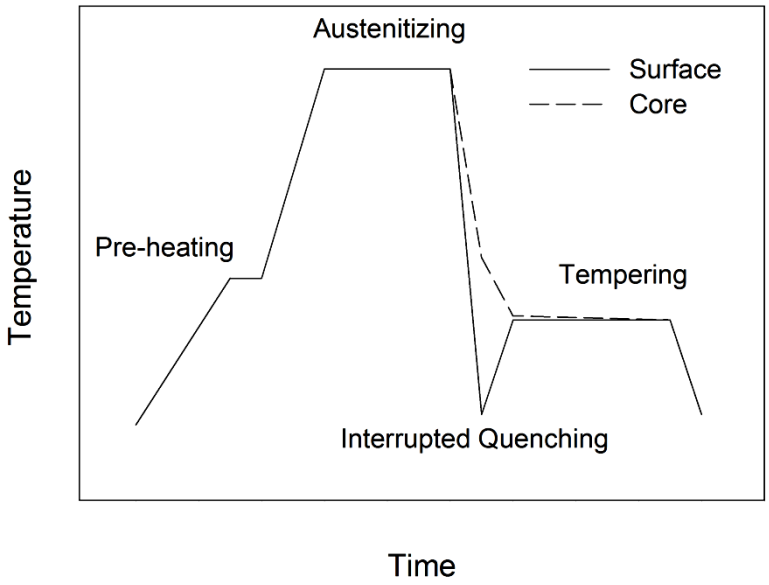

Figure 3.17 Heat treatment diagram, showing the effect of quenching interruption on cooling curves at surface and core.

Once the optimal quenching time and quenchant was determined samples were treated and tempered at different temperatures. After interruption of the quench samples were tempered at a temperature of 250°C, (Ms temperature) for 30 minutes, then a second tempered at 250, 350, 450 and 550°C was carried out. After tempering, the samples were water quenched.

The austenitizing temperature was 950°C. One set of samples were austenitized at 850°C, quenched and tempered at 350°C for comparison. In addition to the interrupted quenching, conventional oil quench and temper was performed to built a S-N reference diagram. In general, 10-15 samples for each treatment were required to construct the Wöhler curves. The conditions and identifications of heat treatments are shown in Table 3.2.

Table 3.2 Conditions and identification of heat treatments.

HT ID	Austenitizing Temperature °C	Quench	1st Temper		2nd Temper		No. Samples
			Temp. °C	Time (min)	Temp. °C	Time (min)	
BIQ1	850	BRINE (1s)	250	30	250	60	10
BIQ2	850	BRINE (1s)	250	30	350	60	10
BIQ3	950	BRINE (1s)	150	30	150	60	3
BIQ4	950	BRINE (1s)	250	30	250	60	15
BIQ5	950	BRINE (1s)	250	30	350	60	10
BIQ6	950	BRINE (1s)	250	30	450	60	10
BIQ7	950	BRINE (1s)	250	30	550	60	12
BIQ8	950	BRINE (1s)	550	60	---	---	6
OQ1	850	OIL	250	60	---	---	6
OQ2	850	OIL	400	60	---	---	10

BIQ= Brine Interrupted Quenching

OQ= Oil Quenching

Note: The number of samples was determined when the fatigue experiments were carried out. Heat treatments with less samples presented low fatigue resistance and no further samples were treated.

3.4. Fatigue Experiments

After heat treated, samples were tested under fatigue. All experiments were performed at a 20 Hz load frequency. Since heat treatment conditions produce a considerable change on fatigue resistance, applied stresses near the fatigue limit were experimentally determined.

The maximum applied stress for all heat treatment conditions was 900 MPa, followed by a middle stress of 600 MPa and a lower stress of 400 MPa. Experiments were repeated 3 times at each stress level for each heat treatment condition, except at 900 MPa where only 2 experiments were performed since the dispersion is low at 10^4 cycles. Infinite fatigue life was considered for samples that endured 5×10^6 cycles. During testing, load data was acquired at a 10Hz frequency in order to correlate the load decrease with crack nucleation and growth.

CHAPTER 4

RESULTS AND DISCUSSION

4.1 Chemical Analysis

The chemical analysis and nominal chemical composition of the AISI 5160 steel are shown in Table 4.1. The composition of the analysis was used to construct the TTT and CCT diagrams.

Table 4.1 Chemical composition of AISI 5160 steel.

	Chemical Composition %wt	
	Nominal	Chemical analysis
Fe	Balance	Balance
C	0.55-0.65	0.58
Si	1.80-2.20	0.26
Mn	0.7-1.00	0.885
P	0.035	0.017
S	0.035	0.016
Cr	0.7-1.00	0.78
Ni	---	0.01
Sr	---	0.013
Ti	---	0.003

4.2 Quenching

Since the cross section of the samples was small, the common requirement of Intensive Quenching of great agitation to destabilise the formation of the vapour blanket was substituted by the usage of brine. The selected salt was sodium nitrite due to its inhibiting characteristics. The concentration that produces the greater cooling rate was experimentally determined.

4.2.1 Optimal $NaNO_2$ concentration

Experiments carried out following the ASTM D6200-01 standard **[40]**, for determination of quenchant severity, showed that the maximum cooling rate obtained with aqueous $NaNO_2$ solutions is obtained at a 4% concentration, see figure 4.1. From the cooling time-temperature curve it can be seen that increasing the $NaNO_2$ concentration produces a proportional reduction of the film-boiling duration up to 4%. It was noticed that the 4% and 9% cooling curves overlapped. Figure 4.1b shows that the cooling rate was 2.1 times greater with 4% $NaNO_2$ than the one obtained under the same conditions for water.

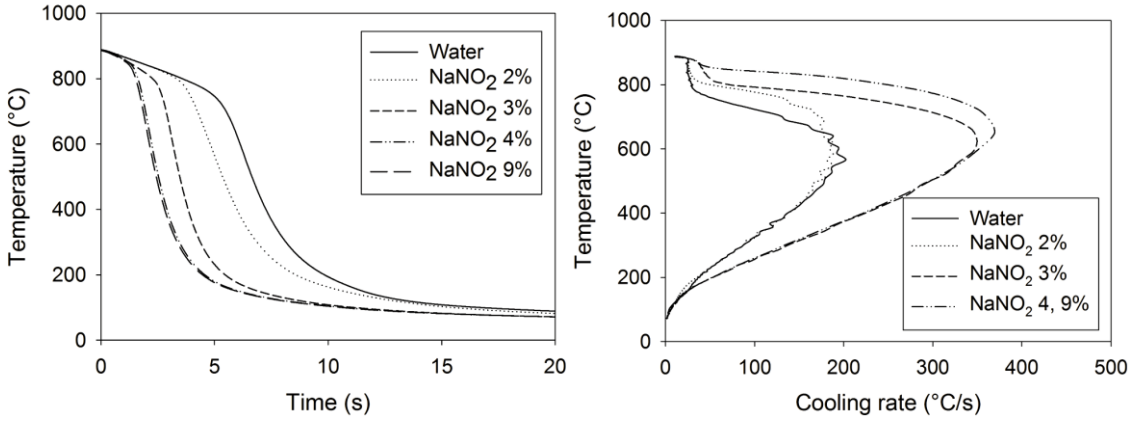

a) b)

Figure 4.1 Cooling curves of a Ø12.5 mm INCONEL 600 probe (a) and cooling rate curves (b).

Cooling curves were also obtained using the stainless steel probe of 8 mm in diameter with three thermocouples for the 4 and 9 % brine solutions. For both concentrations cooling curves almost overlapped the entire time range, the main difference was that with 4% the surface temperature dropped near 112°C while with 9% the temperature dropped only to 140°C. This is related to the saturation temperature of the solution, which is increased with salts addition. Maximum cooling rates were similar, being approximately 1340 and 1300 °C/s respectively. The 4% $NaNO_2$ solution was selected, the thermal gradient from surface to core reach a maximum of almost 750°C in the 8 mm bar. Is worth to note that surface temperature reached the saturation temperature of the quenchant before two seconds and the core at 6 seconds.

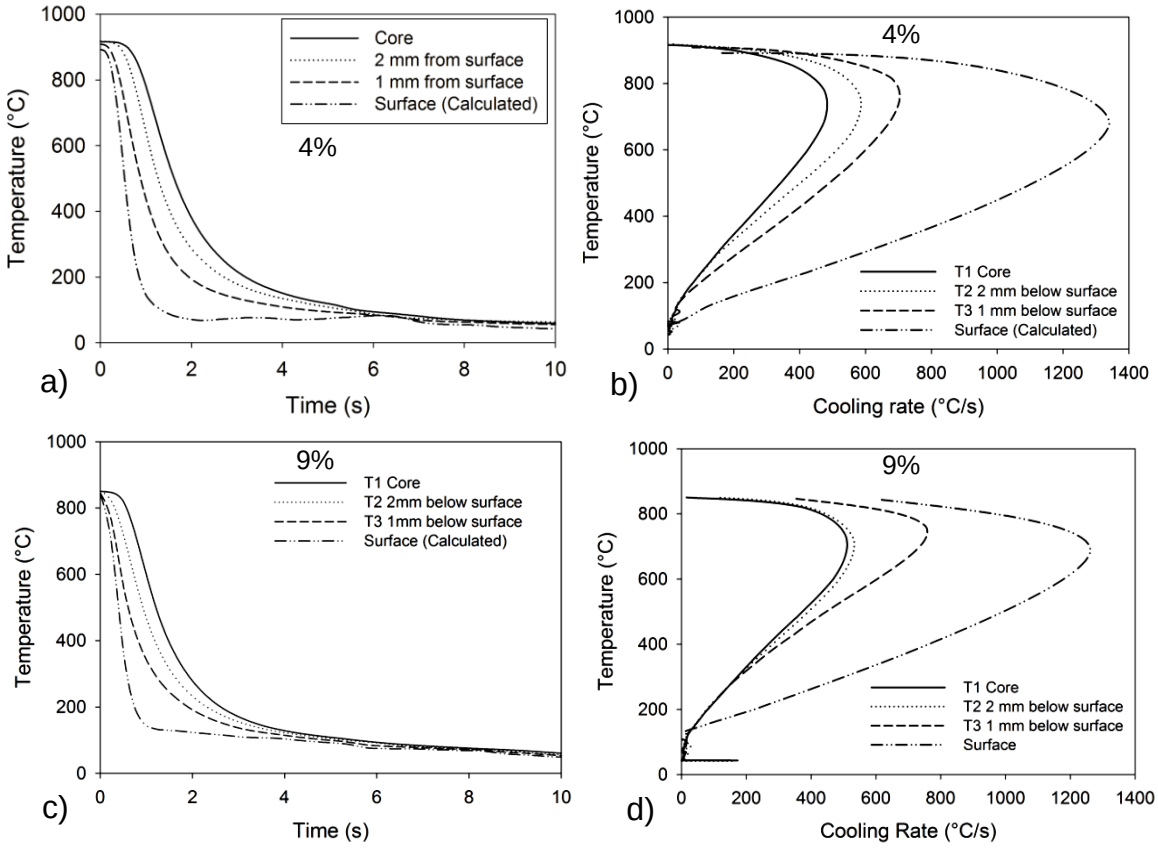

Figure 4.2 Cooling curves and cooling rates curves of a Ø8mm AISI 304 stainless steel bar quenched in 4% a),b) and 9% c),d) NaNO2 aqueous solution.

Oil quench was performed to compare the cooling rates and thermal gradients. It has been reported that the cooling rate commonly required for oil quenching vary from 150 to 200 °C/s. It was established in reference [101] that cooling rate when quenching in canola oil is similar to quenching-oils frequently used. Therefore and since the purpose of this experiments was to compare and not to develop a full research on quenching-oil, canola oil was used to obtain the cooling curves. Figure 4.3 shows the cooling curves and cooling rates obtained. It can be noticed that the higher thermal gradient from the surface to the core did not exceeded 100°C, and that cooling rates were similar through the cross section. Surface cooling rate reached a maximum of 185°C/s which agrees with the usual cooling rates for oil quenching.

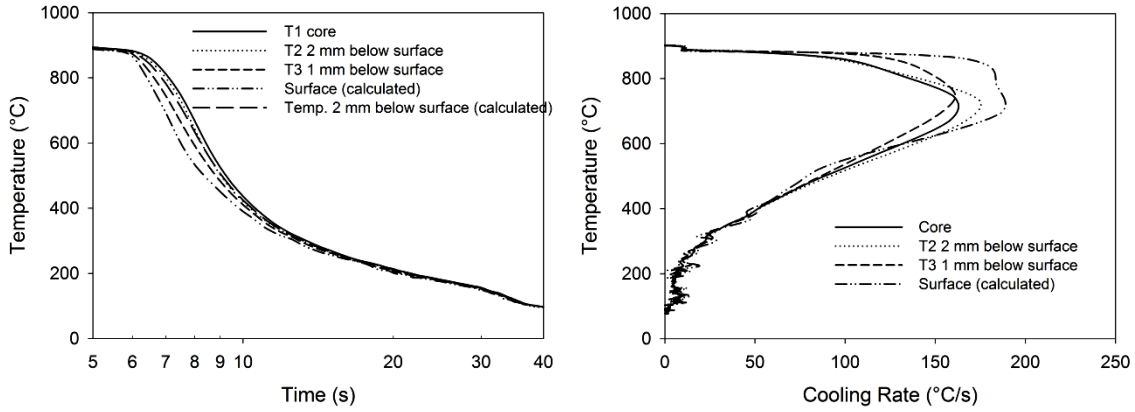

Figure 4.3 Cooling curves and cooling rates curves of a Ø8mm AISI 304 stainless steel bar quenched in oil at 50°C

Figures 4.4 and 4.5 show the experimentally obtained cooling curves and cooling rate curves of the Ø12 mm stainless steel probe and their calculated surface temperature for tap water and for the 4 % $NaNO_2$ solution. During water quenching, the duration of the film-boiling stage was 3.6 seconds (627°C) while the duration of the film boiling stage for the $NaNO_2$ solution was considerably reduced or even eliminated.

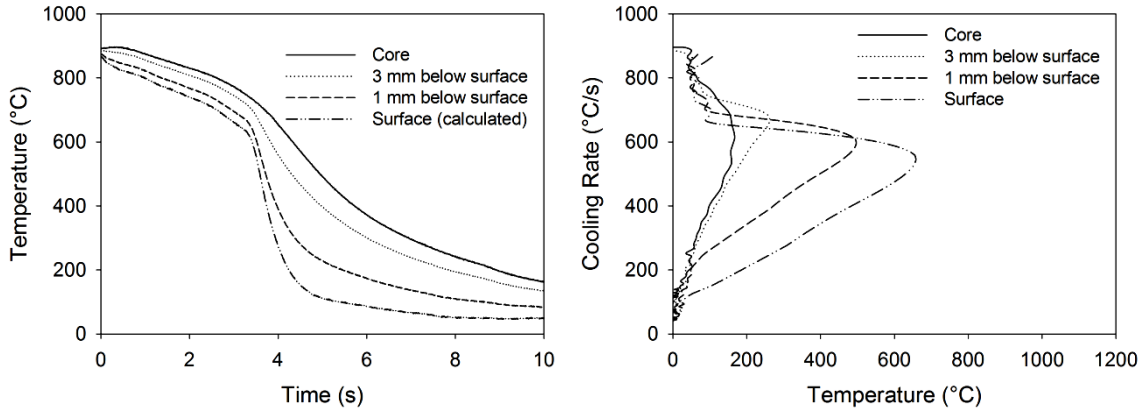

a) b)

Figure 4.4 Cooling curves of a Ø12 mm AISI 304 stainless steel probe quenched in water (a) and cooling rate curves(b).

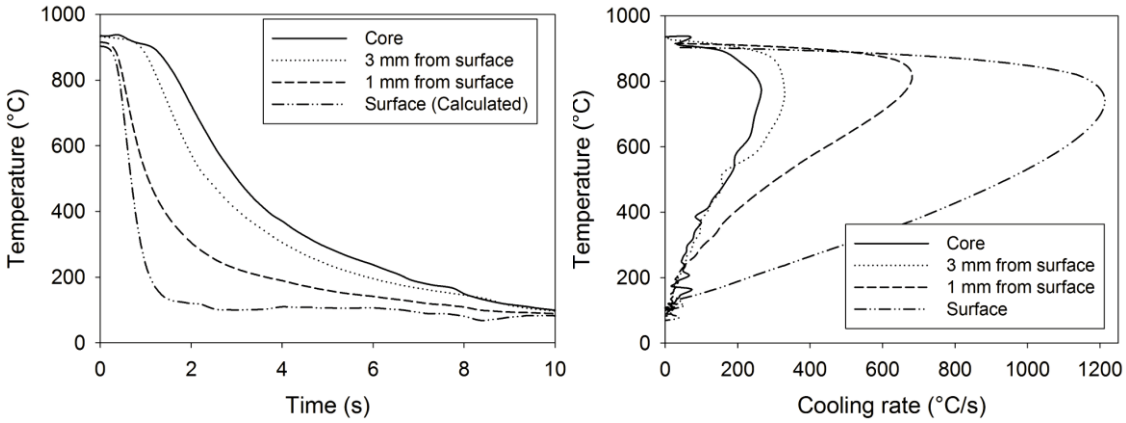

a) b)

Figure 4.5 Cooling and cooling curves of a Ø12 mm AISI 304 stainless steel probe quenched in 4% $NaNO_2$ solution (a) cooling rate curves(b).

It can be noticed that with the 4% sodium nitrite addition of the time that surface required to reach the saturation temperature decreased 3 times and the maximum surface cooling rate increased roughly from 600 to 1200 °C/s. Similarly, for the 8 mm bar, the high cooling rates obtained for the 12 mm bar are suitable to perform a more uniform cooling without cracking.

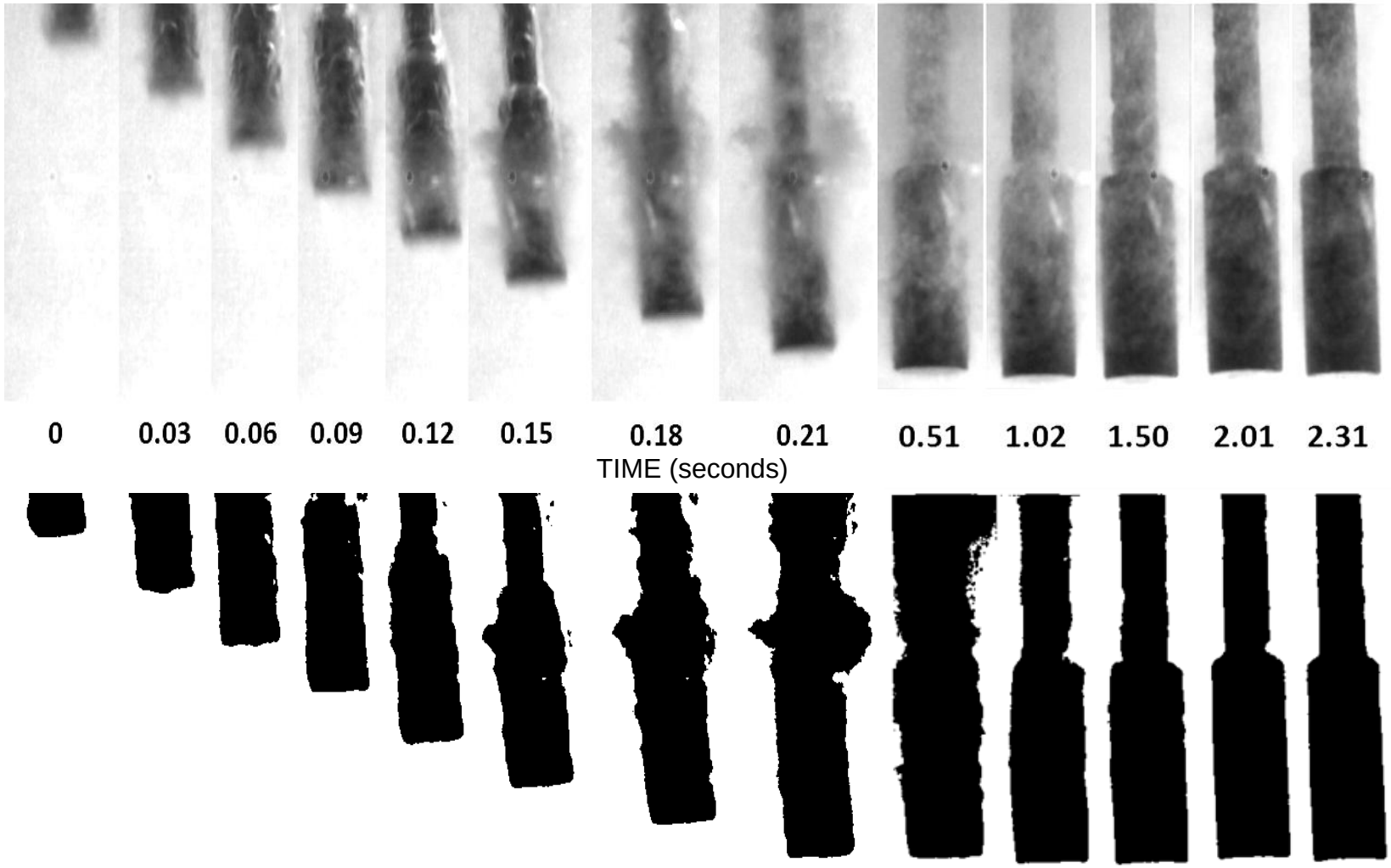

Figure 4.6 Images of a fatigue-type sample (with 8mm and 12 mm sections) quenched from 900°C in 4% $NaNO_2$, showing the cooling stages as function of time (up) and black and white images (b).

Although it is difficult to determine the presence and duration of vapour blanket from the cooling curves in figure 4.5, images taken from the cooling of a sample with the fatigue-type geometry (8 and 12 mm in diameters) as can be seen in figure 4.6, showed that a unstable vapour blanket formed at the very beginning of the cooling. This unstable film started to collapse at 0.15 seconds and at 0.18 seconds collapsed entirely and the nucleate boiling stage took place. Figure 4.7 shows a close up of the cooling curve from figure 4.5 and can be noticed that the unstable vapour blanket observed in figure 4.6 was also detected by the thermocouples as a change in the slope at the beginning of cooling. Furthermore, from figure 4.5, 4.6 and 4.7 can also be noticed that the nucleate boiling stage ended approximately 1 second after the quencching started and the rest of the heat transfer was extracted by convection. From time 1.02 to 2.31 in the black and white image of figure 4.6 the shape of the sample is clearly observed, which means that nucleate boiling had finished.

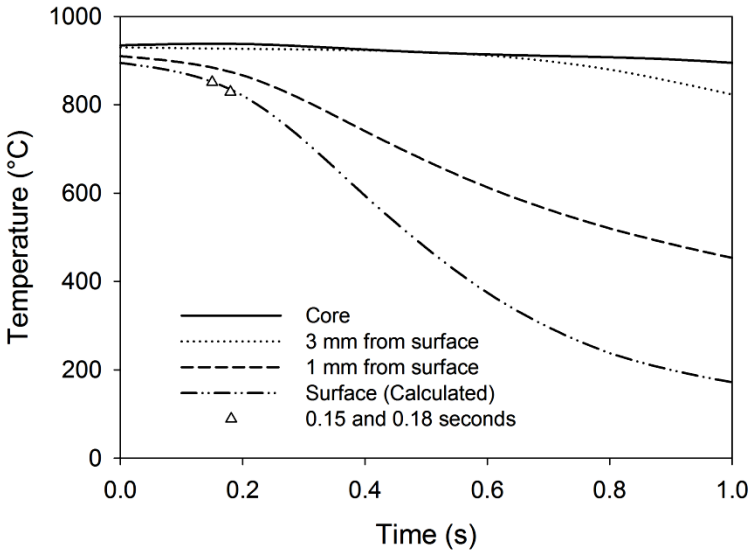

Figure 4.7 Zoom of cooling curve of figure 4.5 to illustrate the vapour blanket formation.

Figure 4.8 shows the heat flux density as function of time for the 12 mm sample quenched in water and 4% $NaNO_2$. The heat flux density was determined using the calculated temperatures at the surface and at 0.1 mm below it. The curve

from quenching in water shows the film boiling stage during the first three seconds of the quench, then nucleate boiling and convection are observed. In the brine heat flux curve, only nucleate boiling and convection are noticeable. The increase in the heat flux density during the nucleate boiling for the aqueous $NaNO_2$ solution (6 MW/m^2) was almost 3 times greater than that obtained with water.

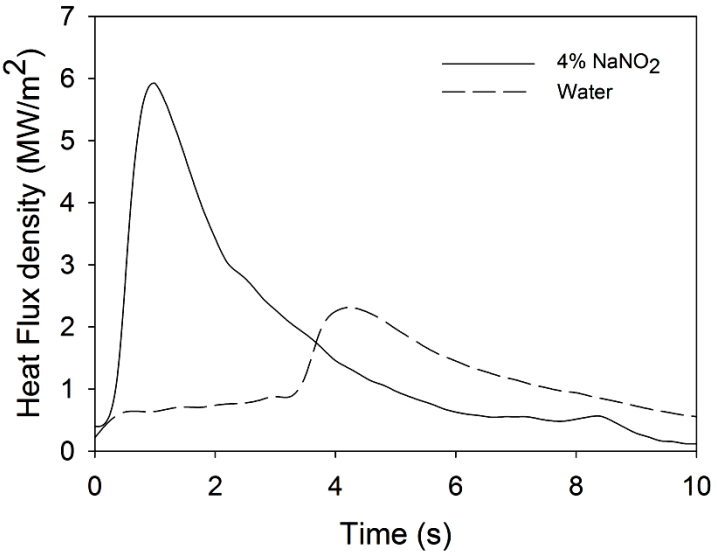

Figure 4.8 Heat Flux density as function of time for water and 4% $NaNO_2$ aqueous solution

The HTC for tap water was 10 KW/m^2 K, which is in good agreement with the value found for water according to Narazaki **[102]**, whose experiments were conducted using a Ø10 mm silver probe. A straightforward comparison cannot be made because the diameter and material differences. The HTC for the 4 % solution reached a maximum of 45 KW/m^2 K. This value is similar to the 42-47 KW/m^2 K reported by Narazaki for 10% brine (NaCl). Once again, for a direct comparison, the size and material of the probe must be considered. Kobasko **[36]** reported values of the average effective HTC of 16 KW/m^2 K for 10 % brine, however this lower value may be derived by the method of HTC determination. If the thermal history at the centre of the probe of experiment of Figure 4.5 is used

to calculate the average effective HTC via the method described in references **[56] [39]**, a value of 9 KW/m^2 K was estimated.

4.2.2 Influence of diameter on cooling

In addition to the cooling of 8 and 12 mm samples, a 20 mm in diameter probe was quenched in the brine solution in order to analyse the effect of probe size on the HTC and on the heat flux density. Cooling and cooling rates curves are shown in figure 4.9. As expected, an increase in the diameter corresponds to a reduction of the HTC and heat flux (Figure 4.10 and 4.11 respectively). According to the figure of the heat flux as function of time, a linear correlation was found between the HTC and the diameter (Figure 4.12). However, it is important to point out that this linear relationship could be non-linear for greater diameters as Liscic reported in reference **[20]** and concluded that no simple correlation can be determined as a function of the diameter. The effect of size on the heat flux density is shown in figure 4.11. The heat flux decreased from 7 to 3 MW/m^2 with an increase in diameter from 8 to 20 mm. These findings are important when designing an interrupted quenching, because in order to maintain similar heat transfer conditions, the cooling severity has to be increased or reduced when the part size is increased or reduced respectively.

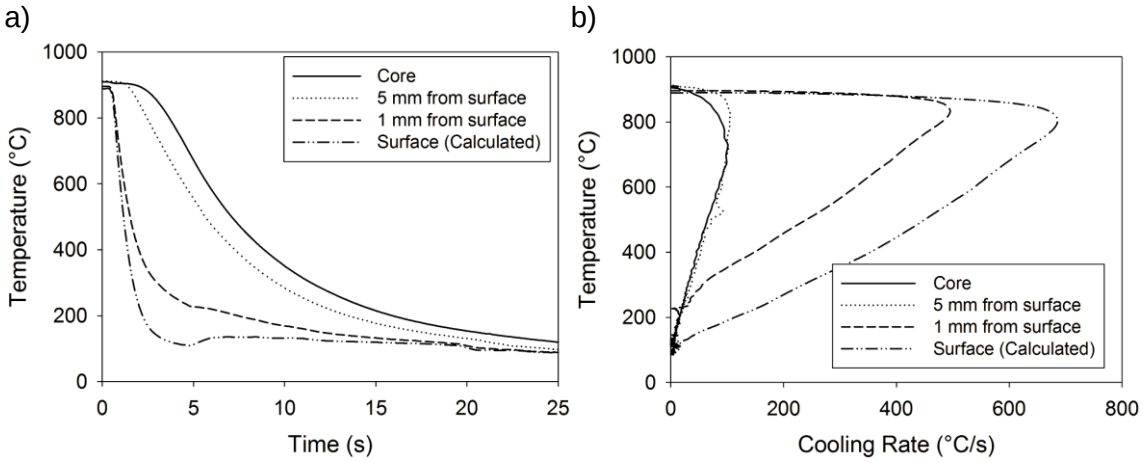

Figure 4.9 Cooling curves of a Ø20 mm AISI 304 stainless steel probe quenched in 4% $NaNO_2$ aqueous solution (a) and cooling rate curves(b).

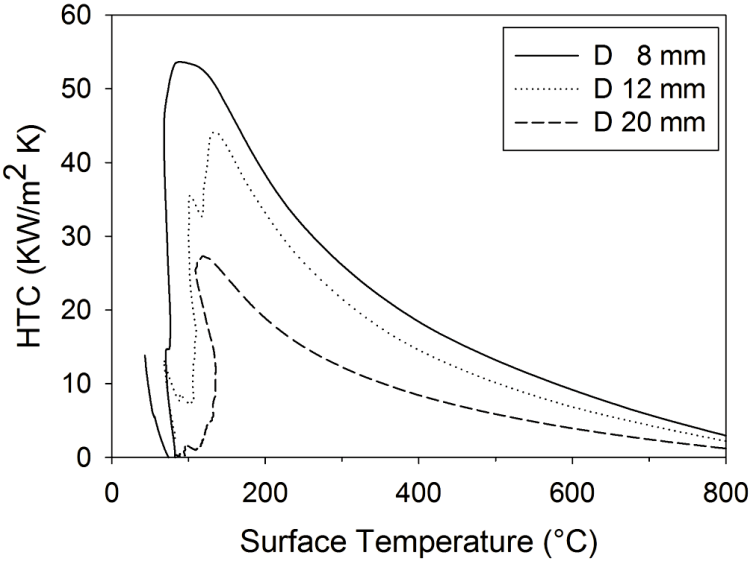

Figure 4.10 HTC as function of surface temperature of AISI 304 stainless steel probes with different diameters when quenched in $NaNO_2$ 4% aqueous solution

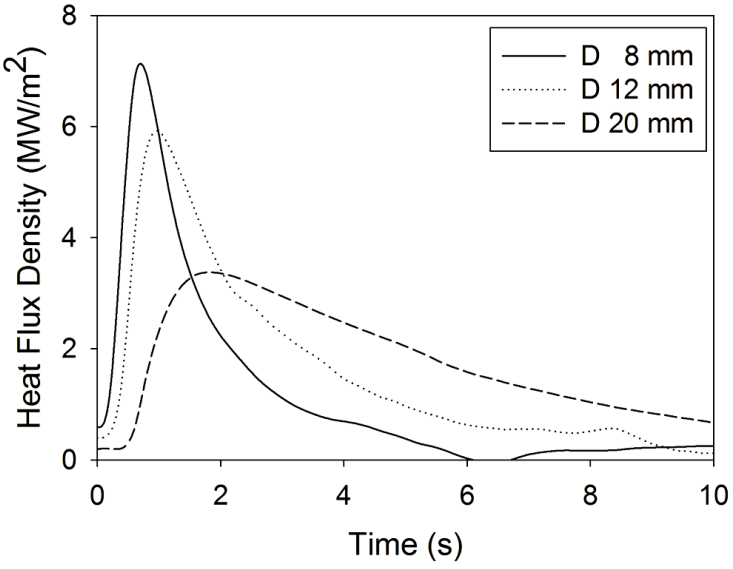

Figure 4.11 Heat flux density as function of time of AISI 304 stainless steel probes with different diameters when quenched in $NaNO_2$ 4% aqueous solution

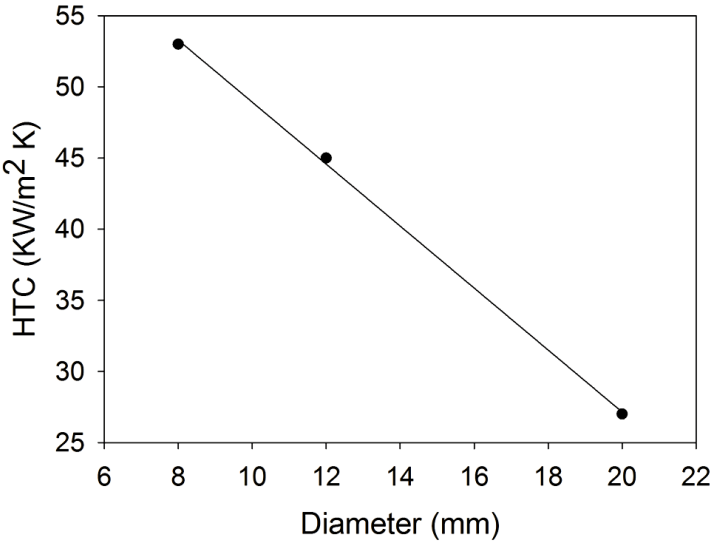

Figure 4.12 HTC as function of bar diameter

4.2.3 Interrupted quenching

Using the cooling curves of figure 4.2 and the transformation diagrams of AISI 5160 steel, the time when the quench has to be interrupted in order to avoid through hardening was determined. Since the Ms temperature is 255 °C, the maximum cooling time was selected to be the time the temperature 1 mm below surface requires to reach the Ms. At this point the surface temperature has already stopped its cooling and further cooling would produce a reduction in the compressive stresses.

Figure 4.13 shows the cooling curve of the 8 mm sample quenched in 4 % brine solution for approximately 1.3 seconds. The surface temperature drops to 112°C and then is reheated by the core thermal energy, then the temperature through the cross section stabilises at 244°C. The temperature 1 mm below surface decreases to 223°C, which is only 32°C below Ms temperature.

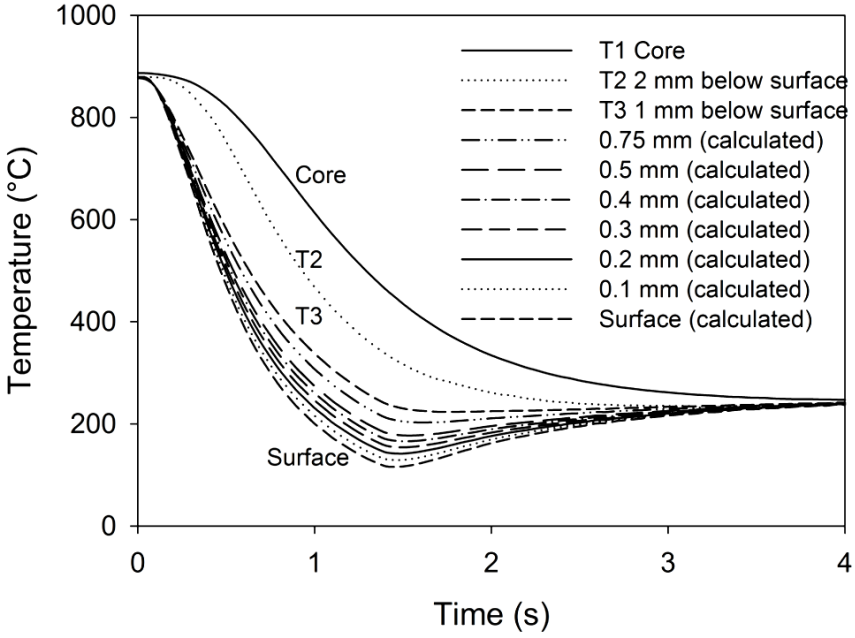

Figure 4.13 Cooling curve of interrupted quenching of 8 mm sample in 4% $NaNO_2$ solution.

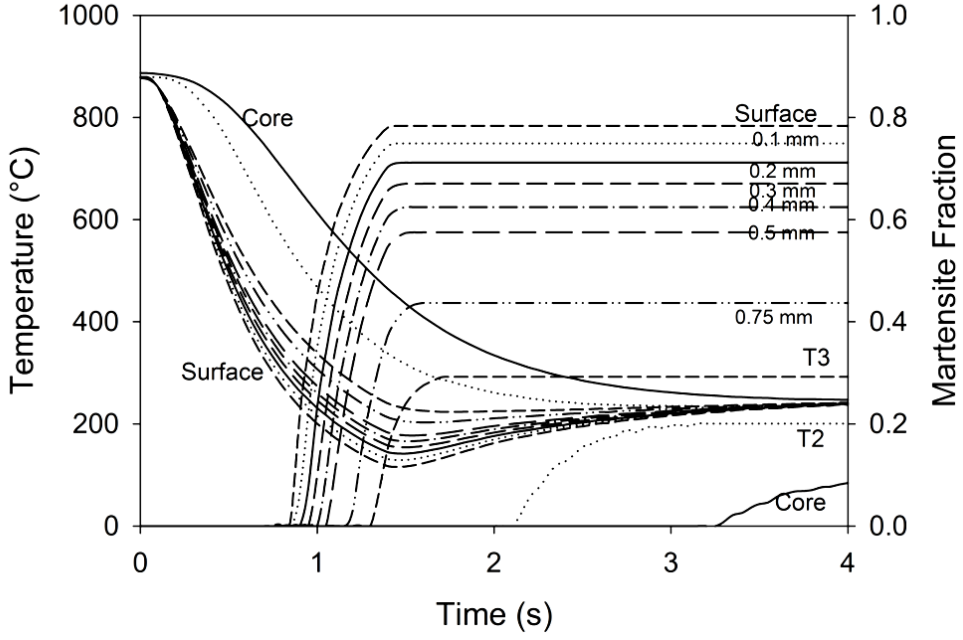

Figure 4.14 Fraction of martensite transformed for nominal AISI 5106 composition (8 mm).

The distribution of the fraction of martensite transformed was calculated from equation 2.13 and the cooling curves data. For the nominal composition the Ms temperature of the AISI 5160 steel is 250°C. Figure 4.14 shows the martensite fraction at different depths for the interrupted quenching. At the surface, the martensite fraction would be expected to be less than 0.8, which means a fraction of 0.2 of retained austenite.

In section 2.2 the effect of carbon on Ms temperature was established. Thus, an increase in the Ms temperature by partial decarburisation would reduce the amount of retained austenite.

4.3 Decarburisation

Results of hardness profiles from the decarburisation experiments are shown in figure 4.15. The hardness values were used in accordance to ref **[81]** to estimate the martensite carbon content. It was found that for completely decarburised zones the hardness of ferrite was nearly 140 HV and zones without decarburisation showed a maximum hardness of 850 HV. The values shown in figure 3.5 are 30 HV offset of the average values reported for steels. Therefore it was considered that the entire curve has an offset of 30 HV lower for the 5160 steel. For each hardness point, 4 measurements were taken an averaged.

Carbon content was estimated by plotting the equation that describes the curve of figure 3.5 and using the hardness values obtained. In figure 4.16 the decarburisation profile is displayed.

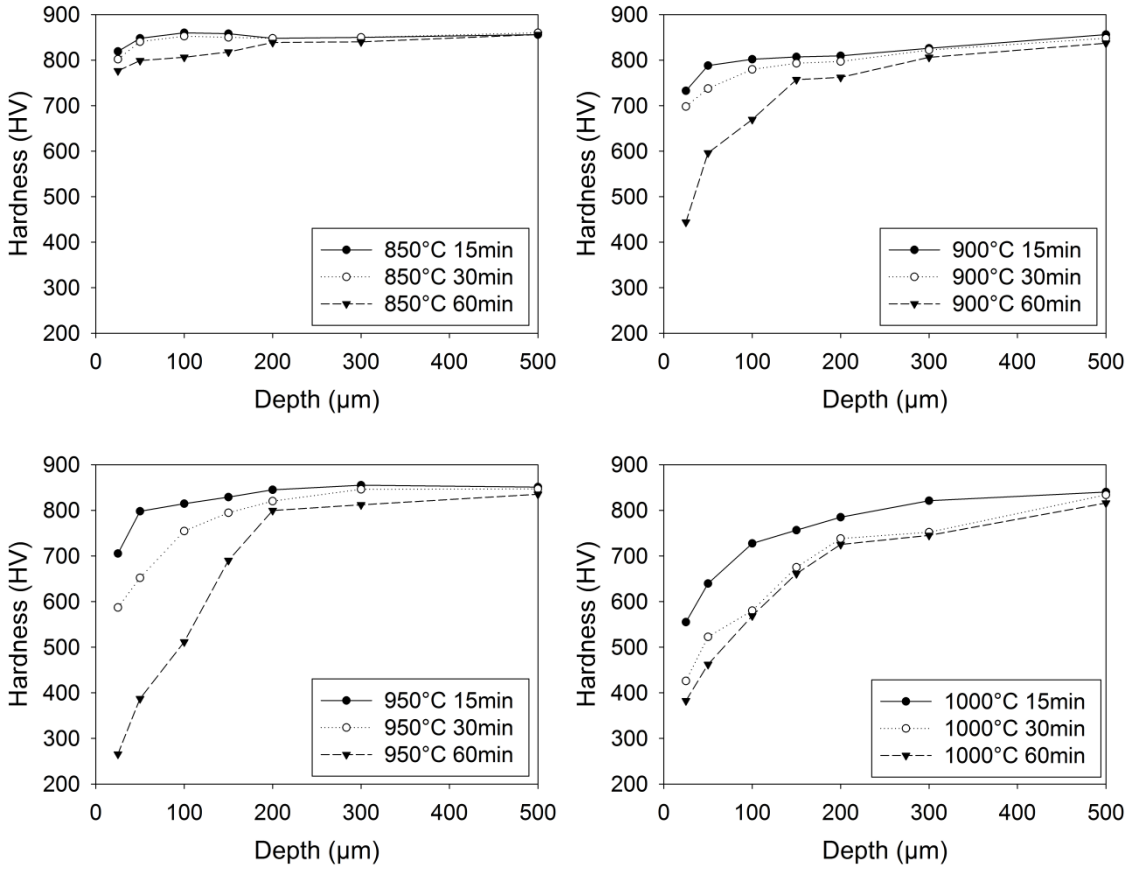

Figure 4.15 Hardness profile as function of austenitizing temperature and time.

As can be noticed from figures 4.15 and 4.16, there is a clear trend of carbon to diffuse outward as the temperature and time are increased. Although this was the trend for almost all conditions, for 1000°C at 60 minutes the decarburisation was similar to the one obtained for 30 minutes at the same temperature and less than the sample heated at 950°C for 60 minutes. This can be explained since at 1000°C chromium segregation below surface was observed, which might reduce the carbon diffusion coefficient. Energy Dispersive X-Ray Spectroscopy (EDS) maps of elemental distribution for the sample heated 1000°C for 60 minutes are displayed in figure 4.17. From microstructure's morphology it can be observed that below the oxide scale, martensite is present and no ferrite nor complete decarburised grains are observed.

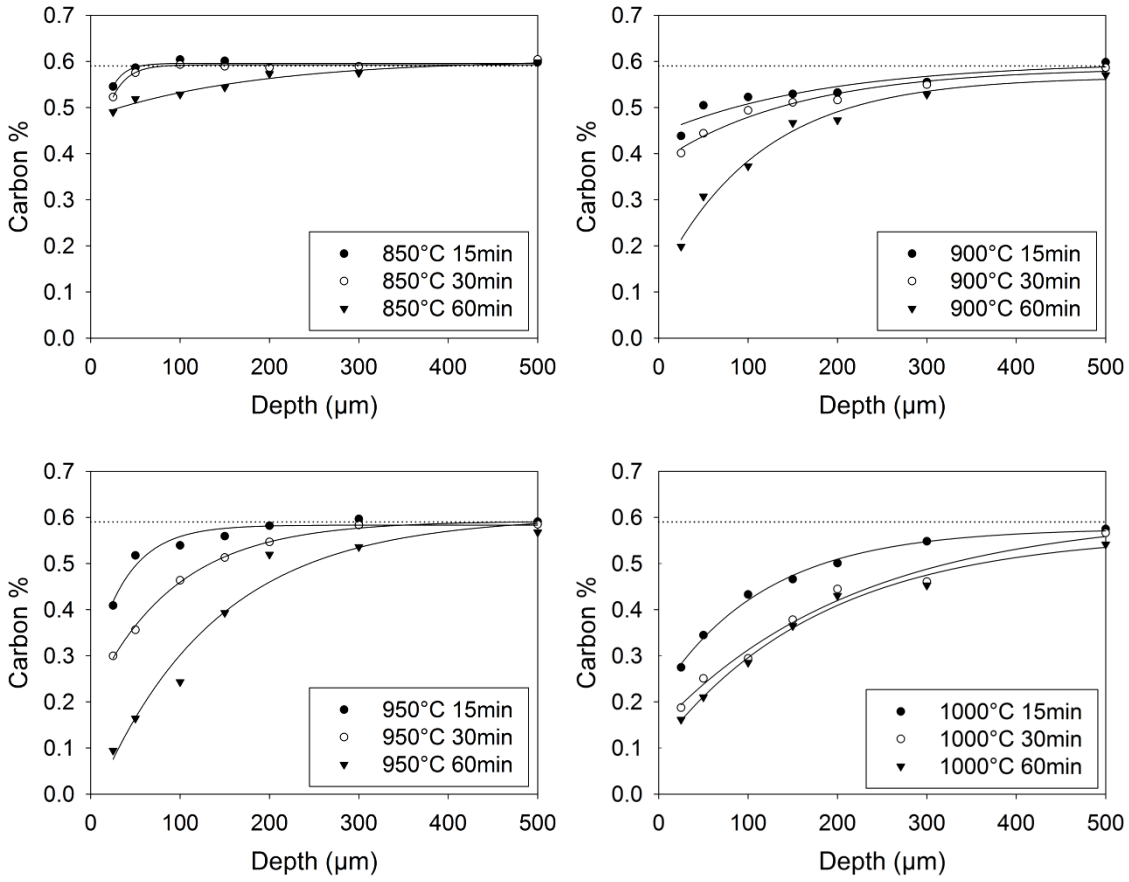

Figure 4.16 Effect of austenitizing temperature and time on decarburisation.

The microstructure of the sample heated at 950°C from 60 minutes displayed in figure 4.18, shows that martensite transformation did not take place completely at the very surface. According to hardness tests, decarburised grains still contain a little amount of carbon, however the hardenability is locally reduced and austenite grains with incomplete transformation are noticed at surface. On the other hand, the 1000°C condition, EDS maps did not showed Cr segregation below the oxide scale. In order to completely understand the diffusion mechanisms and rates, further analysis is suggested.

In section 2 was established that the possible carbon content at surface suitable to enhance the interrupted quenching was 0.3 %. Seeing figure 4.16, the

austenitizing conditions that might promote a partial decarburisation from 0.58 to 0.3 % are an austenitizing temperature of 900°C for approximately 45 min., 950°C for 30 minutes and 1000°C for 15 minutes. The recommended rule

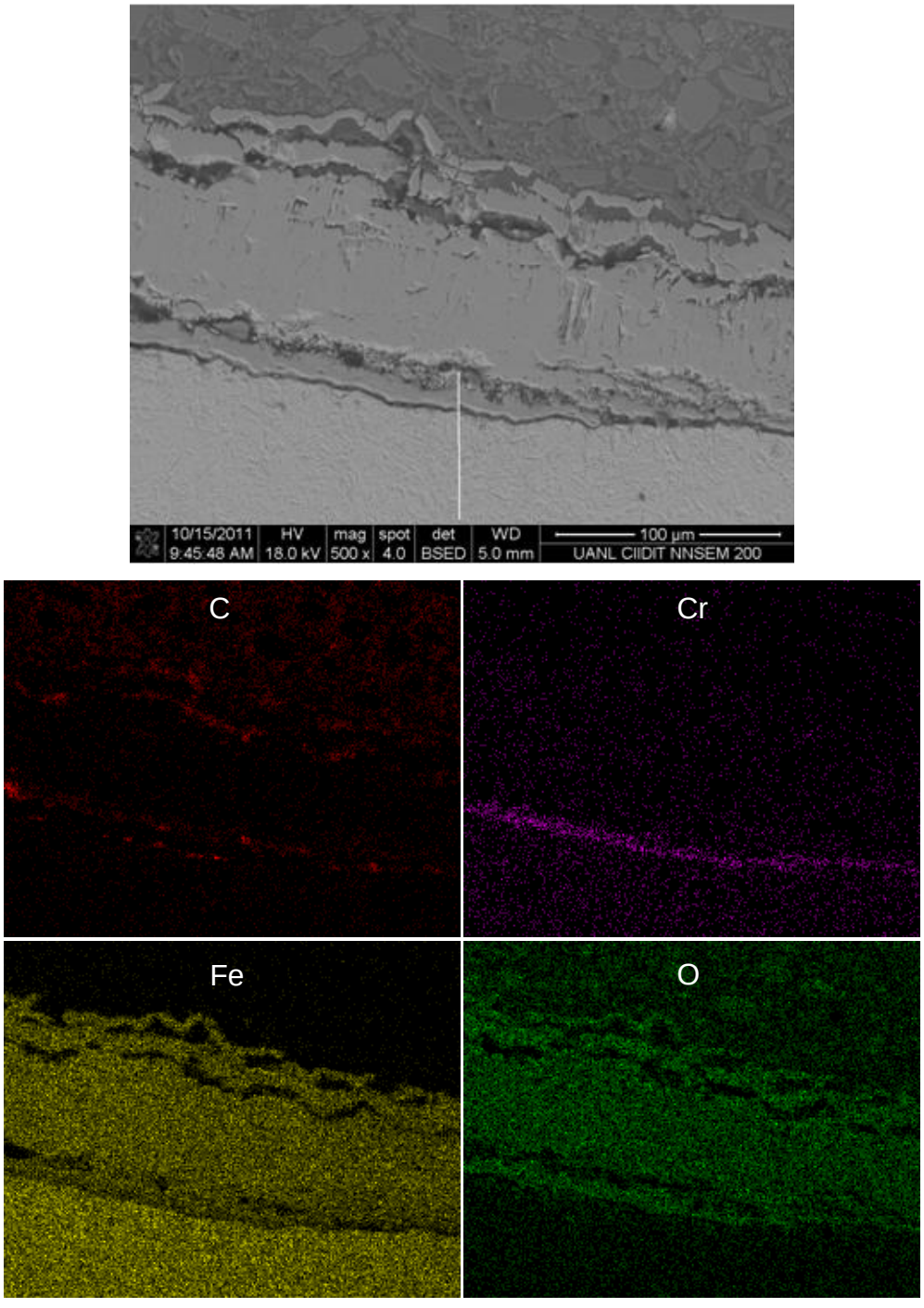

Figure 4.17 EDS maps showing elements distribution at surface of sample heated at 1000°C for 60 min.

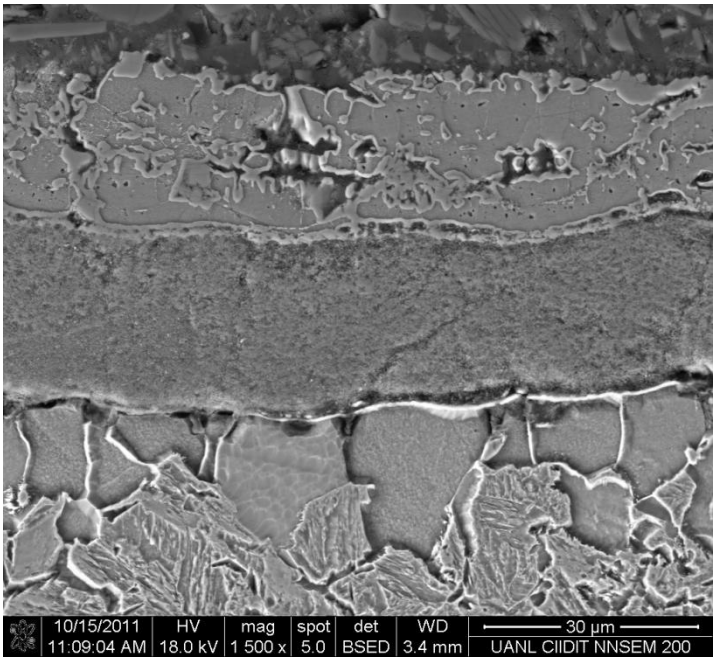

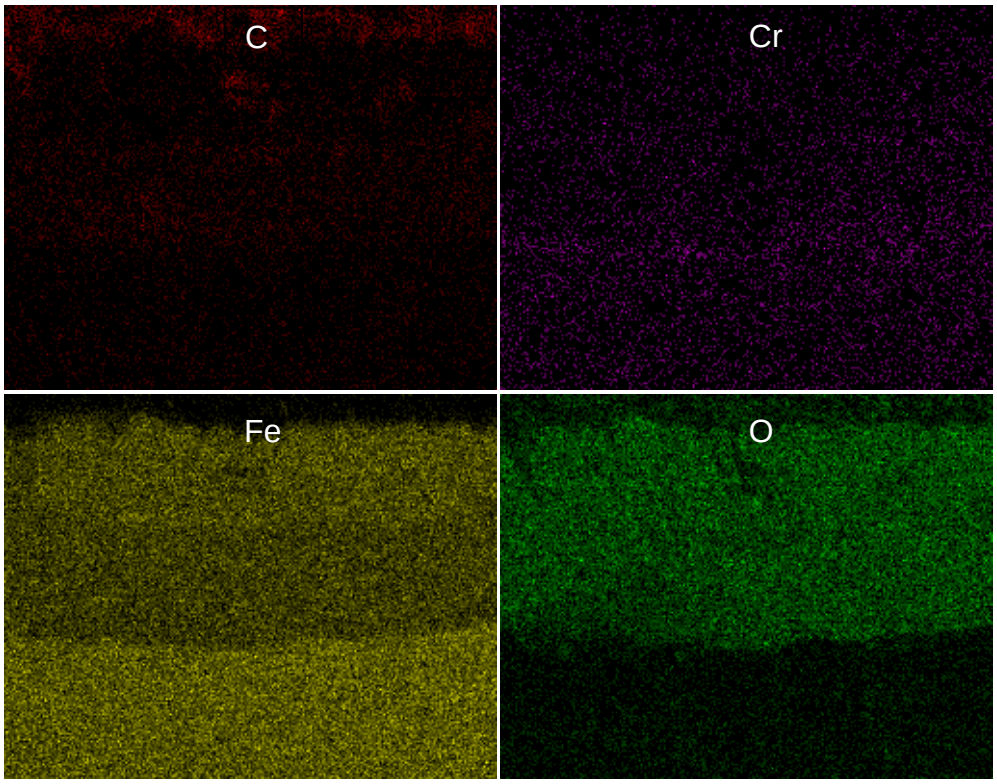

Figure 4.18 EDS maps showing elements distribution at surface of sample heated at 950°C for 60 min.

for austenitizing time is one hour per inch of thickness. Since the fatigue samples have a 12 mm section, the preferred time is 30 minutes in order to

promote full and uniform austenitization. Austenitizing at 1000°C for 15 minutes was discarded, moreover, this high temperature promote the formation of a thick oxide scale. Therefore, austenitizing at 950°C for 30 minutes was selected. Figure 4.19 shows the difference between the morphology of martensite partially decarburised (surface) and martensite without decarburisation (core).

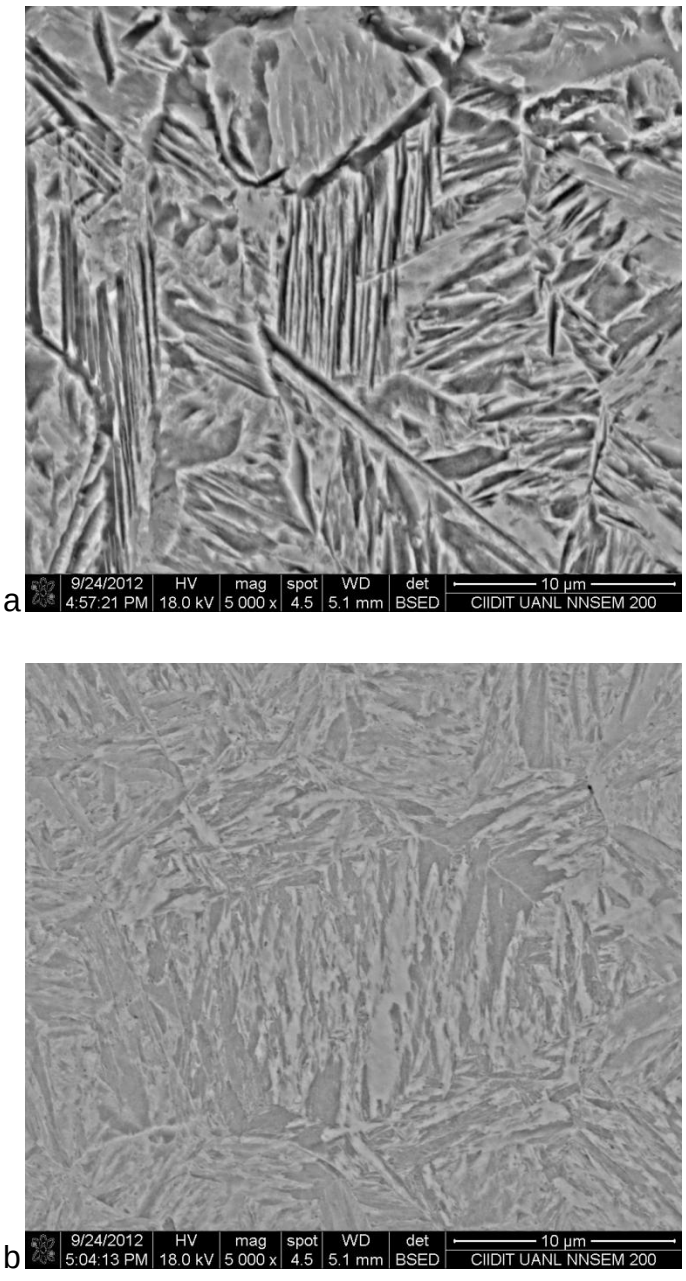

Figure 4.19 Morphology of as-quenched martensite with 0.3 wt% C (a) and 0.58 % C (b).

After the austenitizing condition was selected and the carbon profile estimated, the effect of partial decarburisation on the local Ms temperature had to be evaluated. Although the effect of decarburisation on TTT and CCT diagrams was shown in figure 2.26, including the increase of Ms temperature to 384°C for 0.3 % C, the local Ms temperature will have a decreasing distribution from surface to core as function of the carbon content. This is, using the carbon profile and the Andrews' equation (Eq. 2.14) the Ms temperature at different depths was obtained as showed in Figure 4.20.

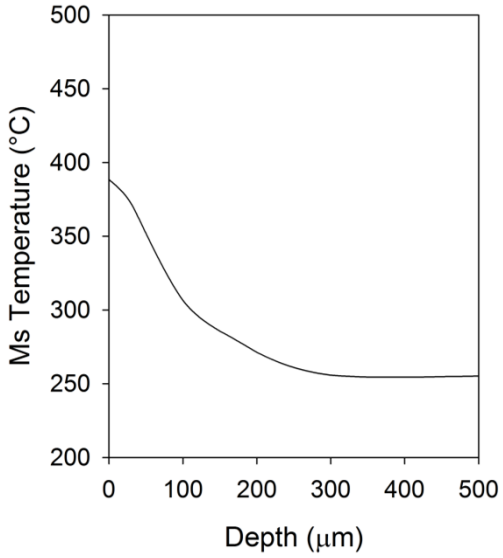

Depth	Ms (°C)
Surface	388.4
0.025 mm	375.8
0.05 mm	352.0
0.10 mm	306.5
0.15 mm	285.6
0.20 mm	271.3
0.30 mm	255.8
0.50 mm	255.2

Figure 4.20 Martensite start temperature distribution.

With the shift in surface Ms, transformation at surface would occur 0.3 seconds in advance as it would without decarburisation, while transformation 1 mm below surface takes place at the same cooling time. In addition, as can be seen in figure 4.21, the martensite fraction increased from the original value of 0.78 to 0.97. Therefore, the reduction in retained austenite might be more favourable from a fatigue point of view, compared with the detrimental effect that the loss of carbon may cause. This, since the more carbon a steel contains, the more brittle its martensite becomes **[103]** and the more susceptible to cracking. In addition, if the amount of retained austenite is reduced and the fatigue resistance might be increased, because of the well known detrimental effects of retained austenite on fatigue due to its intrinsic low ability to retard crack growth **[80]**.

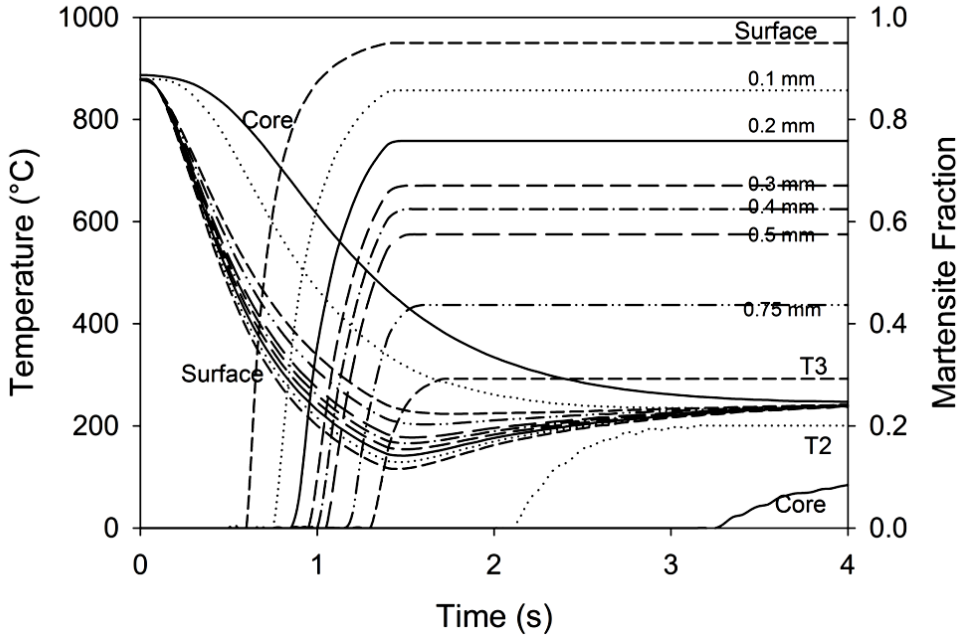

Figure 4.21 Fraction of martensite transformed for a partially decarburised AISI 5106 subjected to the same interrupted quenching of figure 4.13.

From the point of view of the intensive quenching theory, the greater the thermal gradient the greater compressive stresses. This since the first surface layer of martensite transform maintaining the bulk thermally-expanded size. Thus when the subsurface and core contract, they pull the surface layer.

For the case of partial decarburisation the surface transformation takes place at 388°C, which is 0.3 seconds prior to the non-decarburised case, which means that subsurface and core size are hotter and therefore larger when the martensite transformation at surface starts. The shift of only 0.3 seconds in the surface transformation means that the core temperature at the beginning of transformation at the surface is close to 800°C instead of 600°C. From figure 4.22, it could be analysed that when the surface transformation take place for the partially decarburised steel (0.3 % C) at Ms of 388°C the specific volume due to the transformation $\gamma \rightarrow \alpha'$ increased from 0.126 to 0.129 cm^3/g and the core specific volume (0.6 % C at 800°C) was 0.1303 cm^3/g. On the other hand,

for the non-decarburised steel the transformation (at 255 °C) induced a change from 0.125 to 0.1295 cm^3/g, while the core size was 0.1285 cm^3/g. For both cases the surface specific volume increased 2.38 and 3.4 %, respectively. Although less expansion occurred with the partially decarburised steel, the martensite layer takes the size of the core, and compressive residual stresses arise from core contraction. In other words, after the surface transforms the core of the decarburised steel can contract 24% more than the core of the non decarburised steel. As the core contracts, it also pulls the hard martensite shell to the centre.

At the end of the cooling, a certain amount of retained austenite is present. From 4.21 it can be noticed that the untransformed martensite fraction is the fraction of retained austenite. This retained austenite transforms to bainite or pearlite during tempering.

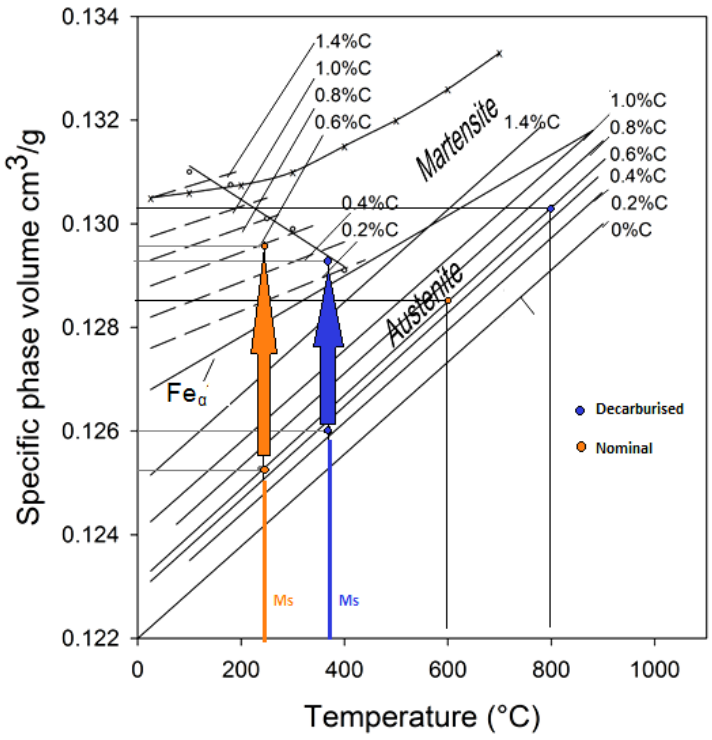

Figure 4.22 Specific phase volume as function of temperature and carbon contents.

4.4 Tempering

Results of tempering experiments carried out in partially decarburised samples with an initial hardness of 860 HV (core) are shown in figure 4.23 and 4.24. Temperatures used were 150, 200, 250, 350, 450 and 550 °C for 60 minutes. As expected the increase in tempering temperature produce a decrease in hardness. This also represents a strength reduction and a toughness increase [104]

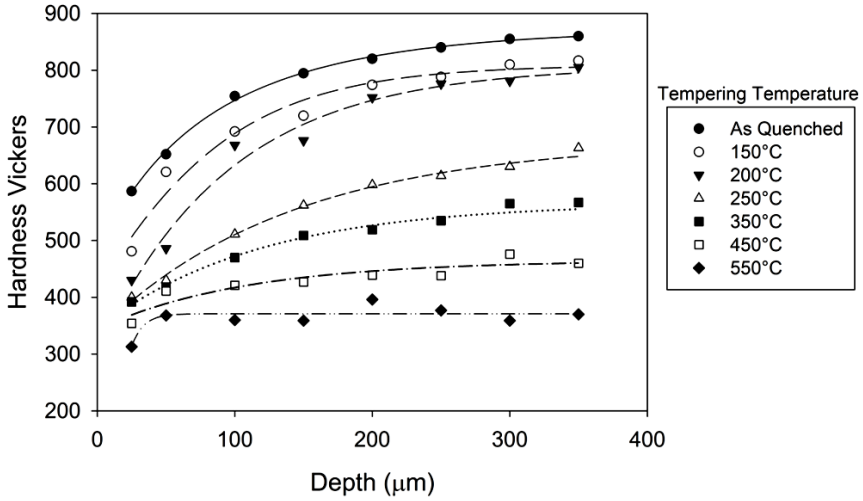

Figure 4.23 Hardness profile of partially decarburised AISI 5160 steel as a function of tempering temperature.

The morphology of tempered martensite is shown in figure 4.25, where can be noticed that cementite particles are expelled from solid solution as the temperature is increased. The morphology of the tempered martensite at 550°C is similar to the morphology usually found in bainite structures. It can be noticed that tempering at 150 °C apparently did not cause any change on the morphology, and from figure 4.24 there can be observed that tempering at 250°C produced a sharp decrease on hardness which is related to the precipitation of carbides and cementite particles. These particles growth as the diffusion of carbon is promoted, until they become microscopically visible [86].

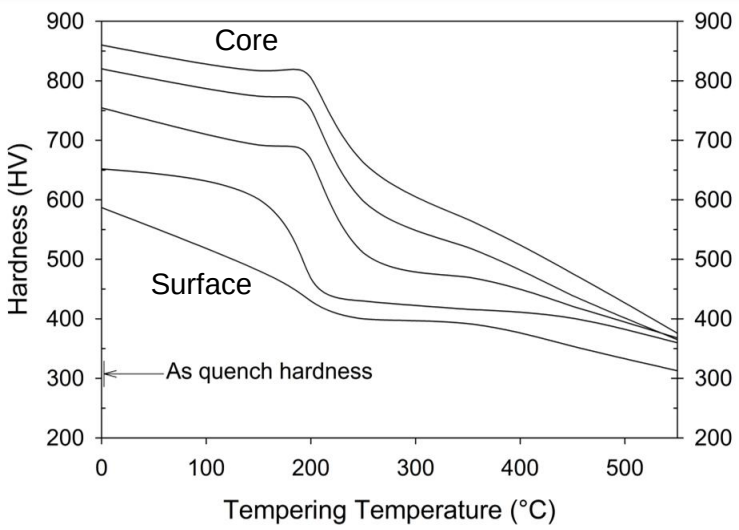

Figure 4.24 Effect of tempering temperature on martensite hardness as a function of depth.

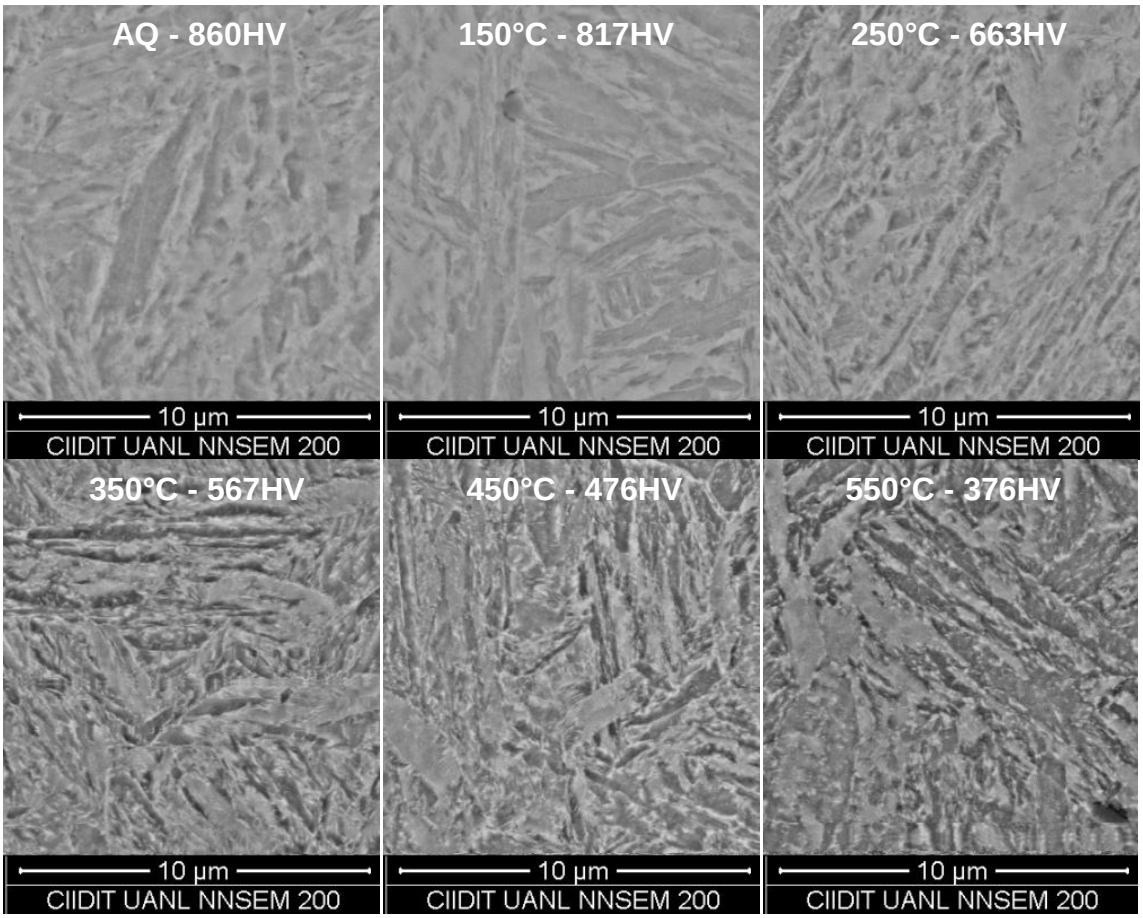

Figure 4.25 Morphology of as-quenched and tempered martensite. Original magnification 5000 X.

4.5 Heat treatments of 5160 steel fatigue samples

Once the austenitizing time and temperature were established for the desired partial decarburisation as well as the quenching and tempering conditions, the heat treatment was performed on the fatigue specimens.

Is important to note that the at the beginning of the experimentation, the fatigue specimens were placed in the furnace at the austenitizing temperature with no prior heating. Because of the high temperature difference between the samples and the furnace, high heating rates took place. For the samples heated this way, great distortion was observed after quenching and tempering. In some cases cracking of steel was observed. In order to avoid this undesired distortion and cracking a pre-heating process at 350°C for 10 minutes was done prior to austenitizing.

The selected temperature to decarburise the surface to 0.3%C was 950°C for 30 minutes, then cooled by an interrupted quenching ($NaNO_2$ 4% solution for 1 second) and followed by tempering. Some conditions included a second tempering at different temperatures (see figure 3.17).

As mentioned in section 4.2 and 4.3 the expected microstructure after the interruption of the quenching is a martensite shell and a bainite core. In figure 4.26a the cooling curve of the heat treatment BIQ4 over the CCT diagram of the 5160 steel is shown. From light microscopy it is difficult to resolve tempered martensite and bainite [78], however by overetching with Nital 4% is possible to distinguish a surface layer. In figure 4.26b a light microscopy image clearly shows a surface layer of nearly to 400 µm in thickness.

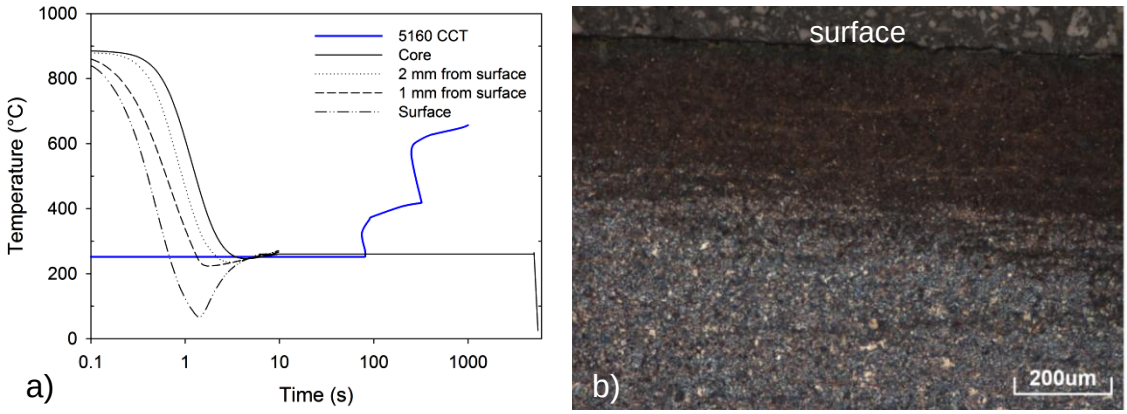

Figure 4.26 Cooling curve over CCT of 5160 steel for HT BIQ4 a), and light microscopy of the cross-section, etched with Nital 4% b).

Figure 4.27 shows Scanning Electron Microscopy (SEM) images of the microstructure morphology at the core and surface. The morphology at the core resembles a mixture of different types of bainite while at surface the microstructure looks likely tempered martensite. A closer inspection at core is shown in figure 4.28, where areas of lower, columnar and nodular bainite can be observed.

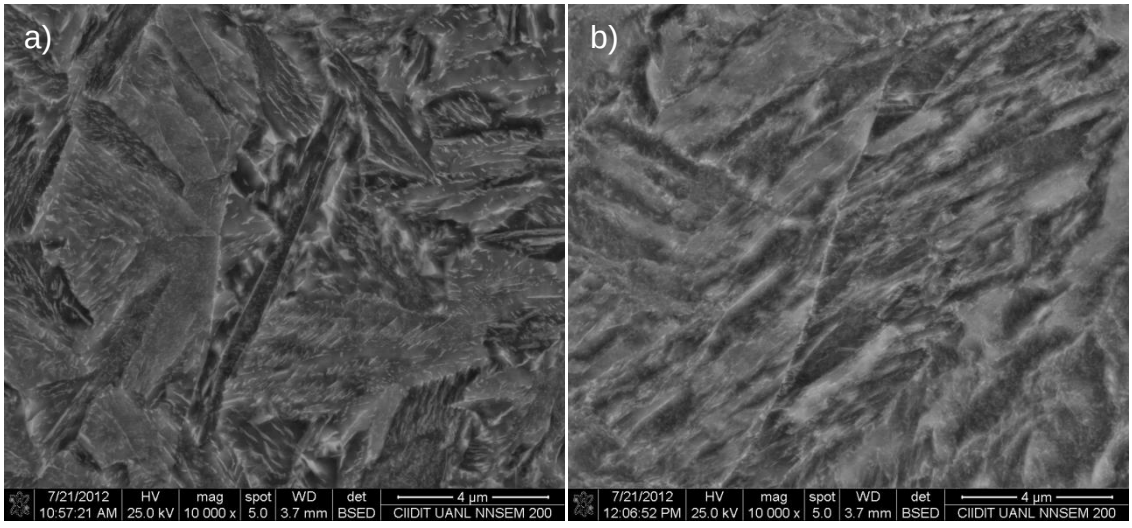

Figure 4.27 Scanning electron microscopy images of BIQ4 showing bainite at the core a) and tempered martensite at surface b).

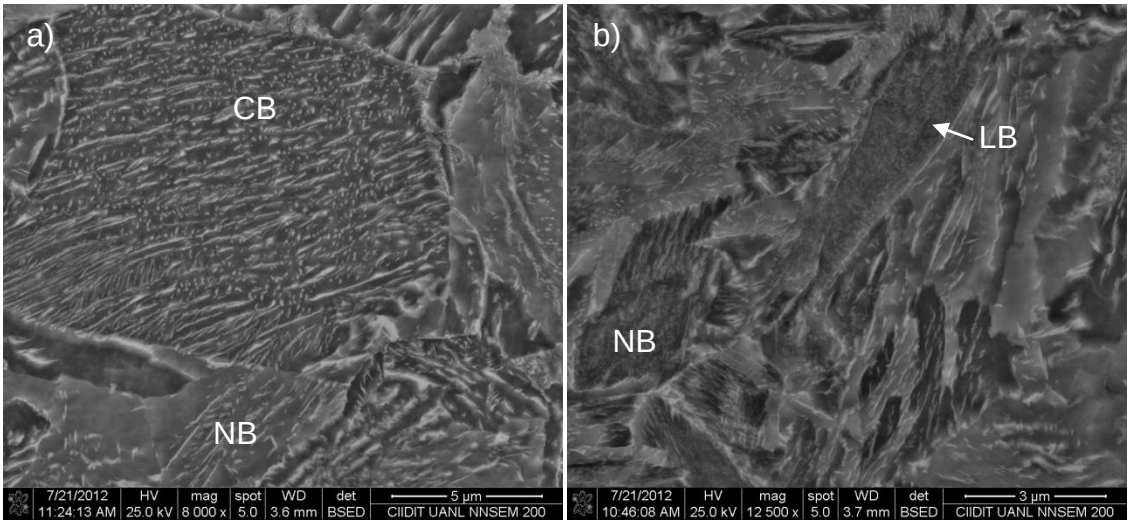

Figure 4.28 SEM images of BIQ4 showing columnar bainite a), and a mixture of lower and nodular bainite b) at core.

From the heat treatment BIQ3, where after the interruption of the cooling the samples was placed at 150°C, the martensite shell is clearly observed with light microscopy since the core microstructure has great amounts of retained austenite which do not get etched by Nital. Since the core temperature remains below the Ms for a longer period of time, the austenite becomes more stable at a lower temperature. In figure 4.29 the martensite case is uniformly formed along the surface, indicating that a uniform heat extraction took place.

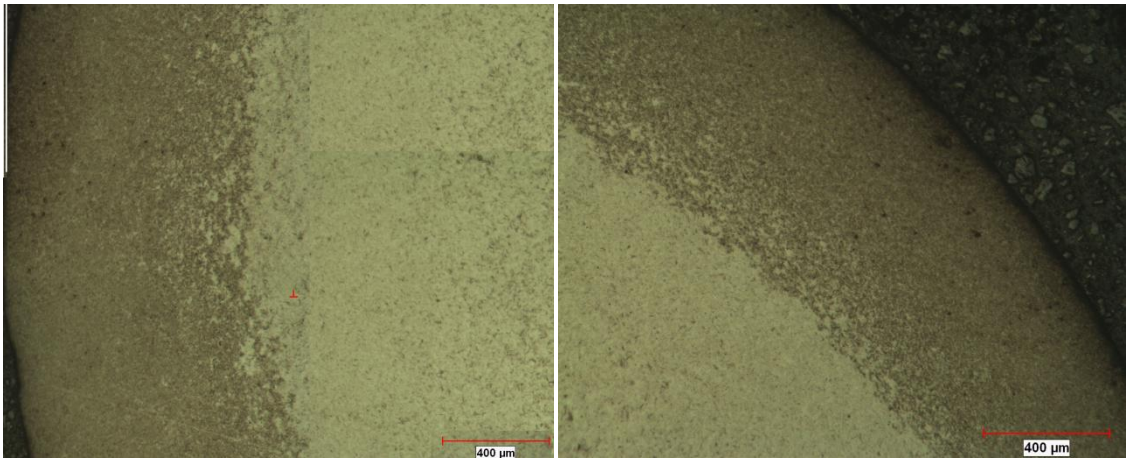

Figure 4.29 Martensite case uniformly formed at surface with BIQ3 treatment.

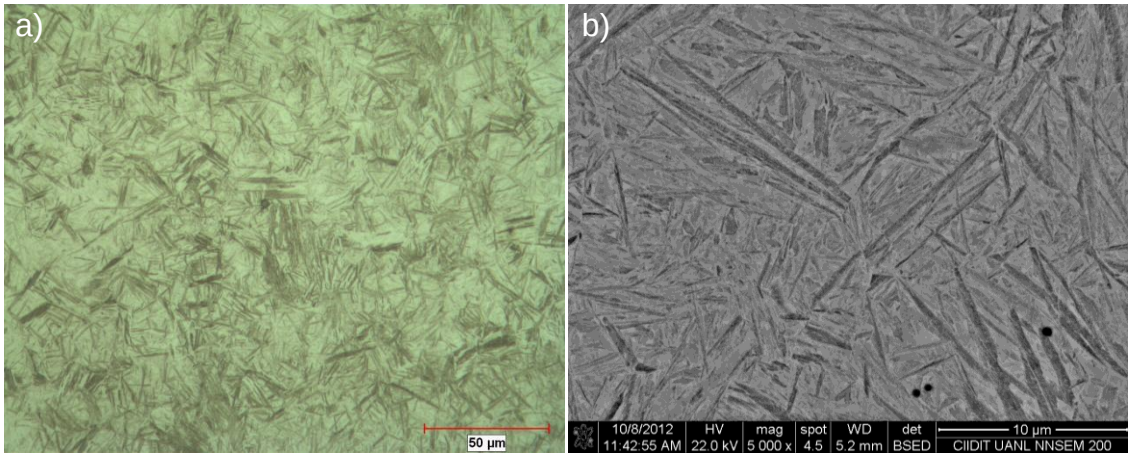

Figure 4.30 Light a) and scanning electron microscopy b) of the core microstructure of BIQ3, showing martensite laths in a retained austenite matrix.

After tempering, the cooling produced a microstructure consisting of martensite laths in a retained austenite matrix. In figure 4.30, light microscopy shows the martensite laths (dark) and retained austenite (light). This type of microstructure is usually prone to fail under fatigue conditions, as is demonstrated in the next section.

On the other tempering extreme temperature (550°C), figure 4.31a shows the microstructure at the core for the BIQ7 treatments. More uniform microstructure was found when a second tempering at 550°C was performed, where only columnar bainite was present; while for BIQ8 (which include only one tempering at 550°C immediately after the interruption of the cooling), pearlite formed at the core instead of bainite, see figure 4.31b. Cooling curves of both conditions are shown in figure 4.32. The microstructure at surface for both cases was tempered martensite as seen in figure 4.33.

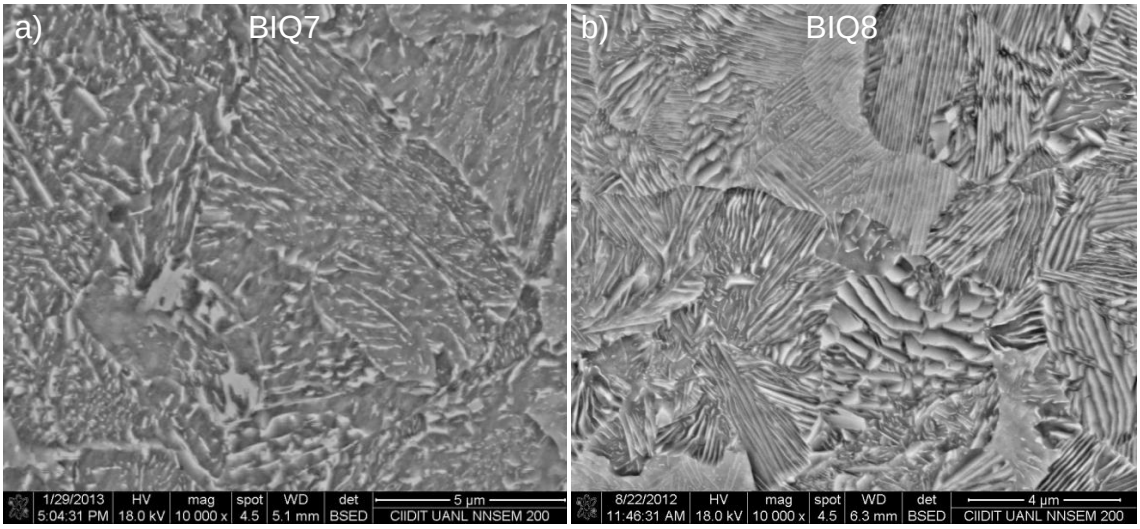

Figure 4.31 Core microstructure of BIQ7 (2nd Tempering at 550°C), showing columnar bainite a); and core microstructure of BIQ8 (1 tempering at 550°C) showing pearlite b).

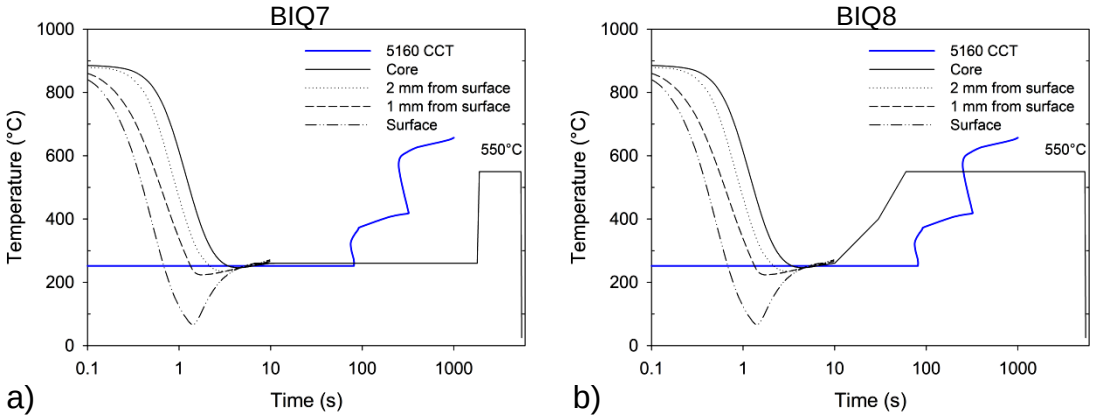

Figure 4.32 Cooling curve over CCT of 5160 steel for BIQ7 a), and BIQ8 b).

In addition, hardness profiles were obtained for BIQ 4-7 in order to evaluate the depth of the martensite case. The main variable of these experiments was the second tempering temperature. Figure 4.34 shows the hardness profiles of each condition, and emphasizes the presence of a martensite layer. In all cases, the hardness at the zone very close to the surface were slightly smaller due to decarburisation, followed by an increase to a maximum at a depth between 200

and 500 µm. The hardness drop is related to the interruption of quenching, however it is difficult to establish a precise depth of the case since there is a gradual reduction in hardness. This gradual reduction is due to the volume fraction of martensite at the local position, and to the temperature of undercooling below the Ms temperature.

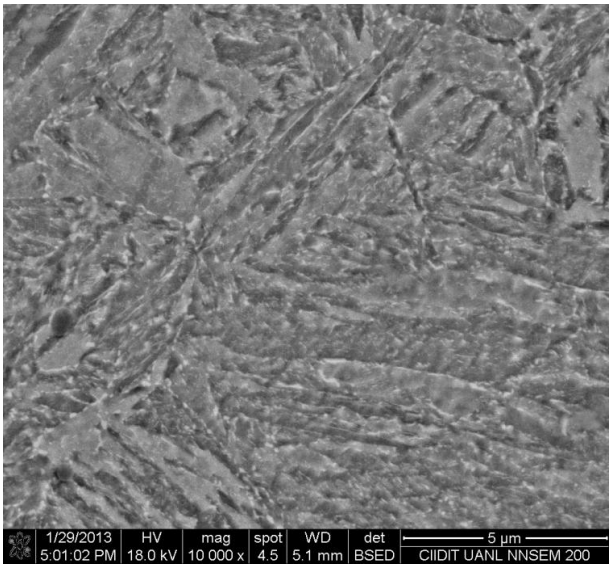

Figure 4.33 Surface microstructure of BIQ7, showing tempered martensite.

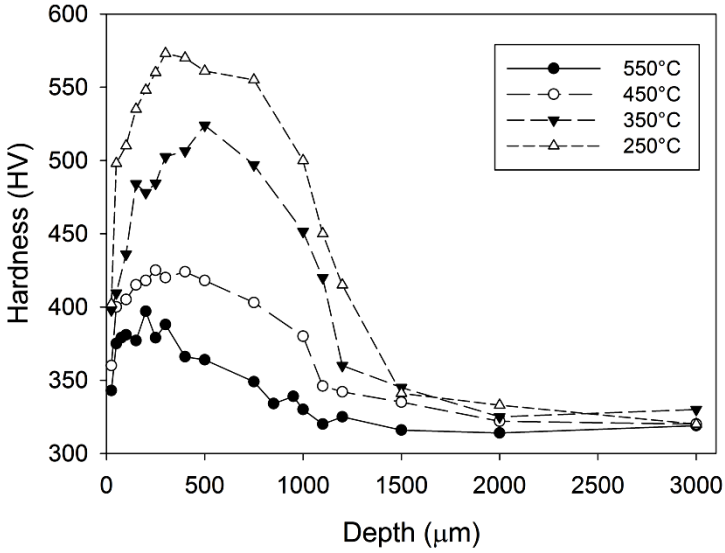

Figure 4.34 Hardness of martensite case as a function of tempering temperature.

The morphology of the oil quench OQ2 is shown in figure 4.35. The microstructure at the surface and core was tempered martensite. Since no decarburisation was promoted by austenitizing at 850°C, the amount of retained austenite is expected to approximate 20%.

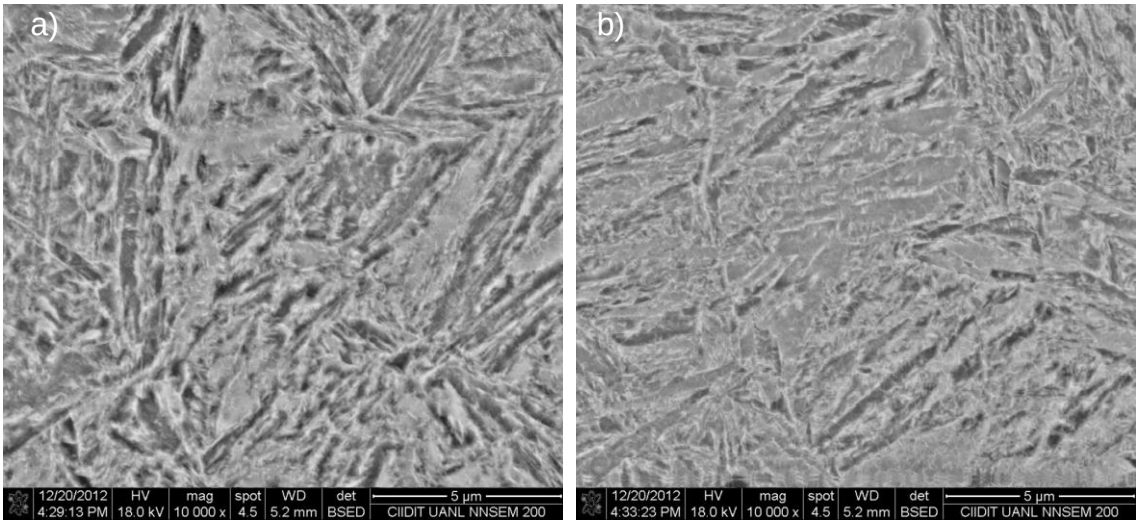

Figure 4.35 Surface and core's microstructure of OQ2, showing tempered martensite.

4.6 Fatigue results

From the rotating bending fatigue experiments valuable information was obtained. Wöhler or S-N diagrams were constructued using the initial stress without considering the presence of a crack. As mentioned in section 3, since the type of loading is a constant deflection instead of a constant load, the load deacreases as the crack grows. In figure 4.36, the type of output data provided by the fatigue tester during each test (load vs cycles) is shown. A closer inspection of the load behaviour is observed in figure 4.37, where the load axis was rescaled to highligh the load decrease. It can be noticed that crack nucleation took place within the first 10,000 cycles. This information is used to

estimate the number of cycles that a crack requires to nucleate and its growth rate in further sections.

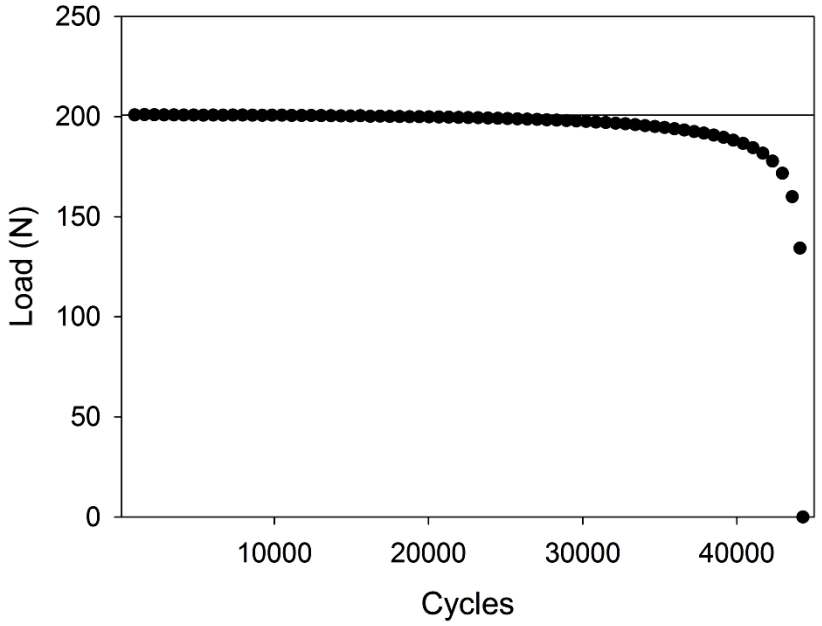

Figure 4.36 Load data acquired during fatigue tests

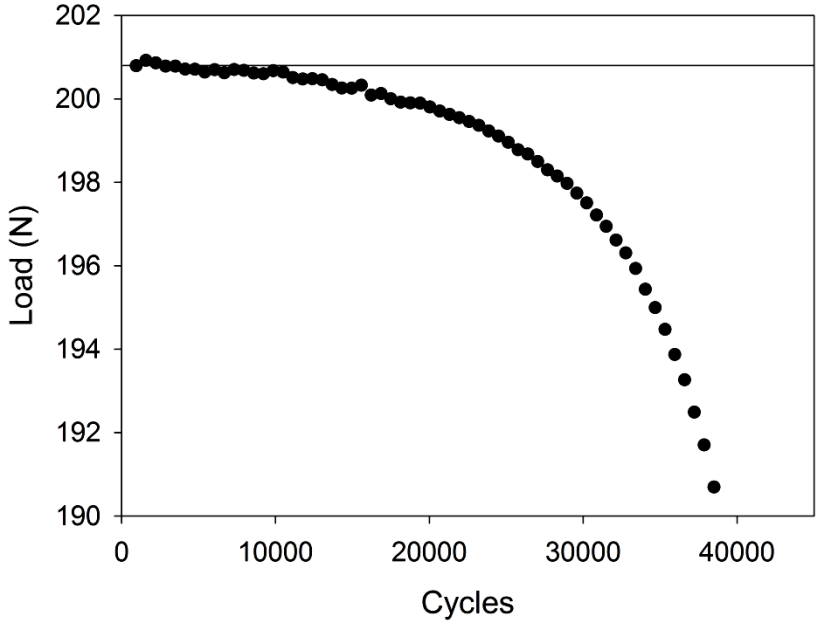

Figure 4.37 Closer inspection of load behaviour of figure 4.36 during fatigue tests.

Results of fatigue experiments of heat treatments BIQ1 and BIQ2, which were austenitized at 850°C are displayed in figure 4.38. In this figure and as it would be in further S-N diagrams, the stress range is on the left vertical axis and the alternating stress or stress amplitude on the right axis. Usually the alternating stress is used to define the fatigue limit, thus the fatigue limit for these conditions were approximately 325 and 375 MPa for the BIQ1 and BIQ2 respectively.

Is important to point out that these fatigue limits are approximations since the staircase method must be employed in order to define more precisely the fatigue limit. In the present work the staircase method was not employed since it requires the usage of at least 12 samples at stress levels close to the fatigue limit. For the construction of the S-N diagrams a total of 10 to 15 samples were employed for each heat treatment condition.

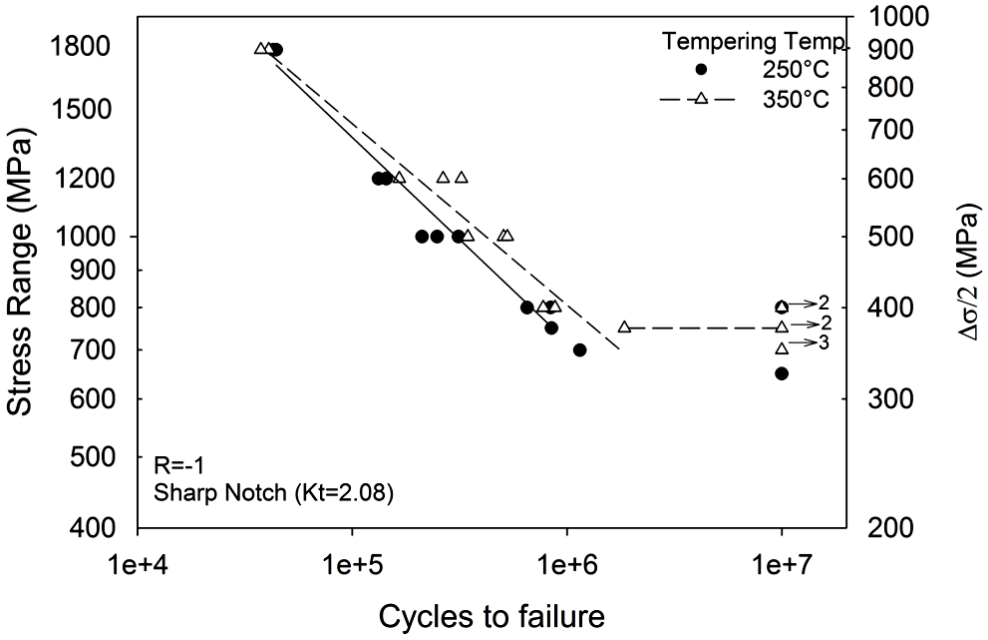

Figure 4.38 S-N diagram of BIQ1 and BIQ2 (austenitizing temperature 850°C)

In most rotating bending fatigue testers there is no information during the test, as is in constant load tests. When no information is available it is impossible to determine if the test condition has produced any damage to the sample after a certain number of cycles, namely 10 millions. This means that when any fatigue test is stopped because an infinite life is considered, usually (5 x 10^6 or 1 x 10^7) the sample has to be discarded, and its experimentation at higher stresses is not acceptable due to the cumulative damage that it might have suffered [105]. An advantage that was found from using this type of tester (constant bending) is that the decrease on load is an *in situ* indicator of the presence of a crack, therefore the samples that endure 1 x 10^7 cycles at a certain stress level without experimenting decrease on load, can be tested a higher stress level assuring that there is no crack present. In order to verigy this fact some samples were cut, and the cross section at the notch was examined. Figure 4.39a shows the cross section of an experiment stopped after 1 million cycles with no load decrease and figure 4.39b an experiment stopped when the load decrease of 0.6 N was detected. The presence of a short crack at the radius was noticed when the cross section was analysed.

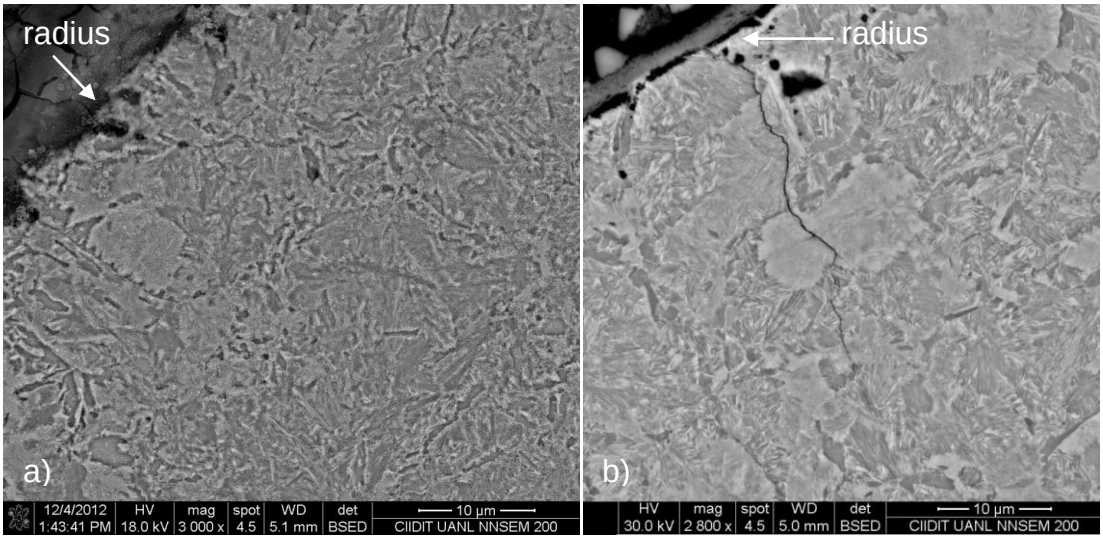

Figure 4.39 Cross section at notch after 1 millions cycles of a sample with no decrease on load a) and with a 0.6 N load decrease b).

Caution was taken not to retest any sample that experimented a decrease on load in the previous test. This allows to determine the fatigue limit for each fatigue sample, if small stress steps increments are used. The stress increments used to define the fatigue limit were of 25 MPa which represented a 6 N increase of the applied load.

In addition, since the applied load is displayed during the experiment, it is possible to predict whether the sample would fail or not. It was observed that conditions that do not promote a decrease of load (less than 0.3 N) during the first million of cycles did not fail after 10 million cycles.

An infinite fatigue life was considered to be 1×10^7 for fatigue experiments of BIQ1, BIQ2 and BIQ4 treatments. However, since it was noticed that all samples that failed, did it within the first two million cycles or did not fail, the infinite fatigue life considered for further experiments was 5×10^6 cycles.

The results of experiments BIQ4 to BIQ7 (austenitizing at 950°C, quenched 1s in brine solution, tempered at 250°C for 30 min. and with a second tempering at different temperatures) are shown in figure 4.40. As can be clearly noted an increase on the second tempering temperature enhances the fatigue resistance. With a tempering of 250°C the fatigue limit was 300 MPa which represents a low fatigue resistance. As the tempering temperature was increased to 350 and 450°C the fatigue limit increase to 475 and 490 MPa respectively. Although the fatigue limit differs of only 15 MPa there is a switch to the right of the 450°C condition of the linear part of the diagram. Interestingly, the slope of the linear part of the 350, 450 and 550°C diagrams seems to be the same. The major enhancement in the fatigue limit was observed when increasing from 250 to 350°C where an increase of the fatigue limit of 58% was

noticed. Then an increase from 350 to 450°C produced only a 3% increase in the fatigue limit. Finally, increasing from 450 to 550°C produced an increase in the fatigue limit of 17%. The total improvement on the limit from the inferior condition of 250°C to the final condition of 550°C was almost doubled.

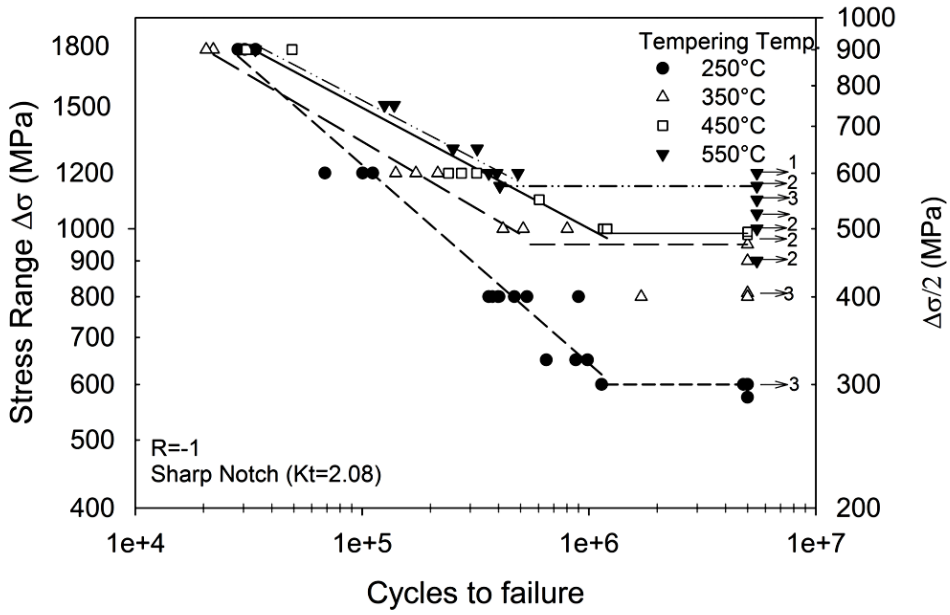

Figure 4.40 S-N Diagrams for heat treatments BIQ4 to BIQ7 (austenitizing temperature. 950°C)

The results of BIQ3, do not appear in figure 4.40 since the samples only resisted 450 cycles at 900 MPa (amplitude) and less than 5000 cycles at 600 MPa. As expected, even that a well defined martensite case was formed at the surface, the great amount of retained austenite in addition to the martensite formed after cooling from the tempering temperature (150°C), reduced the ductility and the material became brittle.

When comparing the BIQ2 and BIQ5 trials, which differ only on their austenitizing temperature, it is observed that the partially decarburised condition BIQ5 withstood up to 475 MPa without failing while BIQ2 only 375 MPa. This

represents an improvement of 26% in the fatigue limit promoted due to the reduction in the retained austenite by shifting the Ms temperature of surface layers. Retained austenite reduce the fatigue resistance since it promotes the growth of cracks [80]. In figure 4.41 the comparison of these conditions is observed. This figure also validates the hypothesis that a controlled partial decarburisation is beneficial when an interrupted quenching is performed.

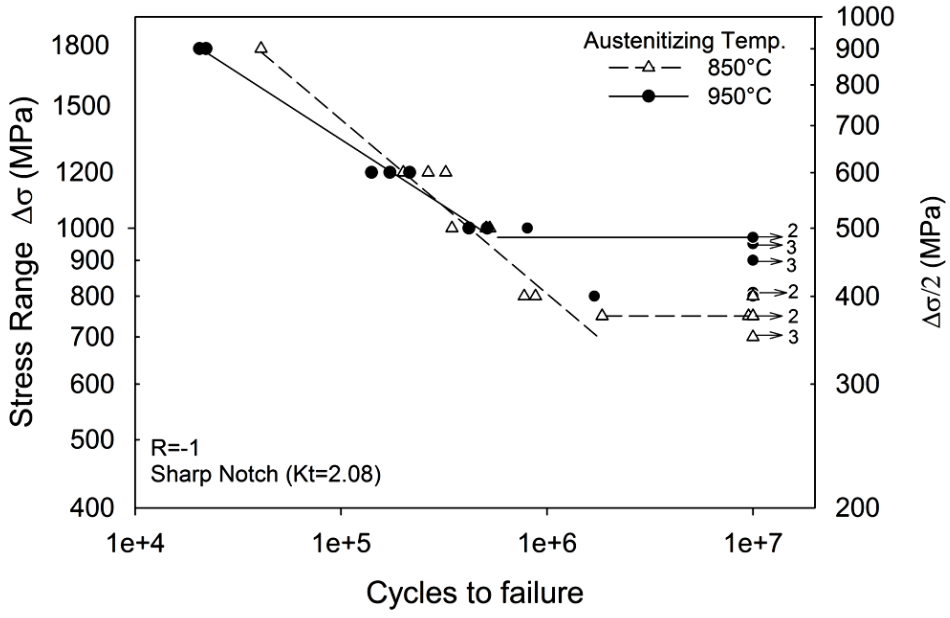

Figure 4.41 S-N diagrams of heat treatment BIQ2 and BIQ5 (2nd tempering at 350°C).

In order to determine if the fatigue resistance of the partially decarburised samples with a second tempering at 550°C was mainly due to the tempering of martensite at this temperature or to the formation of bainite at the core, the BIQ8 trial was performed. As seen in figure 4.32 the difference is that the BIQ8 was put at 550°C directly after the quench, avoiding the bainite nose. As observed in the microstructure of figure 4.31 the core was pearlitic while BIQ7 was bainitic. The surface of both consisted in tempered martensite. In figure 4.42 the S-N diagrams show that the bainitic core has a fatigue limit 53% greater than the

pearlitic one. It has been reported that some fatigue cracks nucleate below the surface when the substrate has a considerable lower strength than the surface layer, although this is difficult to determine, it is a possibility since the surface layer was similar in both heat treatments, although the retained austenite transformed to bainite and pearlite respectively. Other explanation might be related to crack propagation, if the mechanism, once the crack surpass the case, the crack is prone to grow easier in the pearlite structure through the lamellae.

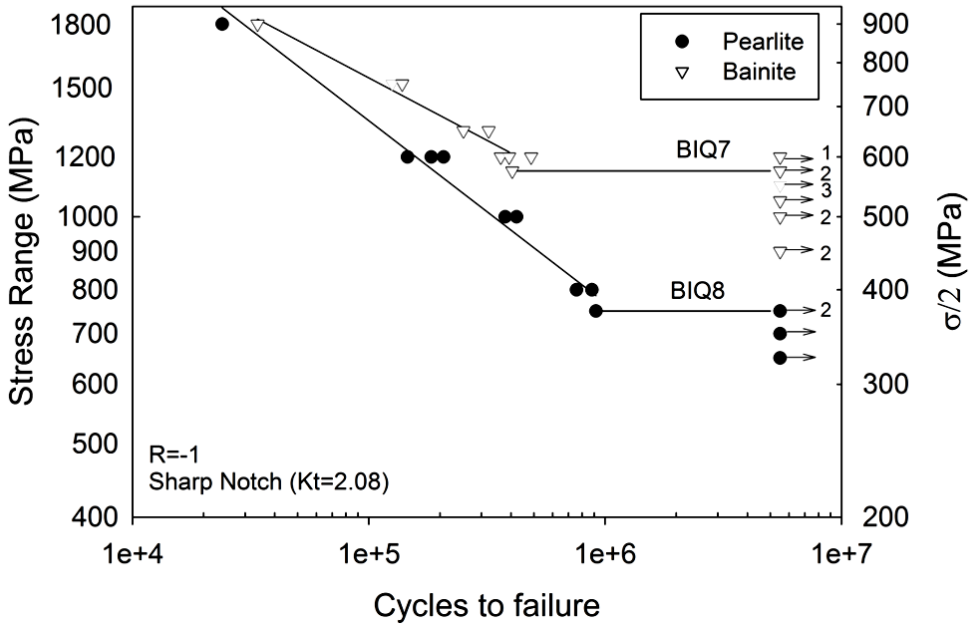

Figure 4.42 S-N diagrams of heat treatments BIQ7 and BIQ8 (see figure 4.32)

The oil quenched samples were tempered at 400°C since according to references [106] and [90] produce the greater fatigue resistance. Spring manufacturers usually temper in the range of 400 to 550°C. Tempering at 250°C was also performed although the steel exhibited very low fatigue resistance. The OQ2 with the tempering at 400°C presented a fatigue limit of 525 MPa, which is superior to the BIQ 4,5 and 6. Nevertheless, the fatigue limit of the oil quenching is inferior 9.5% than the brine interrupted-quenching 7. Figure 4.43 displays the

S-N curves of the OQ2 and the BIQ7. The fact that for the BIQ7 the partial decarburisation increased the volume fraction of martensite and therefore reduced the amount of retained austenite when cooling at room temperature is crucial in the delay of crack nucleation. In addition, this decarburisation do not improve the fatigue resistance by itself, it has to be accompanied by an interrupted quenching. If the quenching is not stopped the core would transform and expand, this expansion of the core would produce tensile stresses on the decarburised layer producing tensile residual stresses or cracking. This is the main reason why decarburisation is related to detrimental effects, since with a conventional quenching (through hardening) the mechanical and fatigue properties decrease.

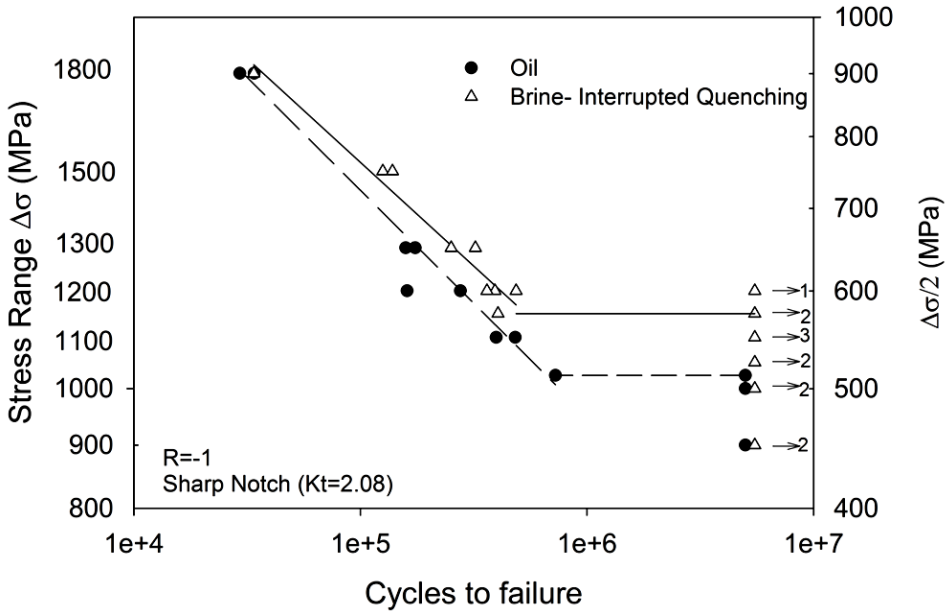

Figure 4.43 S-N diagrams of the OQ2 and BIQ7.

4.6.1 Fractography

Macroscopic observation of fractures from samples of heat treatments BIQ4 to BIQ 7 are shown in figures 4.44 to 4.47. The upper image in each figure shows the fracture at a high stress (900 MPa) after approximately 1 x 10^3 cycles, and the lower image exhibits the fracture at a stress level near to the fatigue limit of each heat treatment, referred in figure 4.40. The diameter of the surface fracture is 8 mm, thus the print shows a 11.8X magnification. From the fracture at 900 MPa it can be noted that the cracks nucleated from surface in a radial direction towards the centre, and therefore the overload fracture is a well defined circle. Comparing with figure 2.29 the fractures at a high stress are like from the schematic figure of a mild notch, since the final fracture due to the overload is off-centred, although the value of 900 MPa might not be a high nominal stress enough as the diagram attempts to describe. Instead, this applied stress could represent a mild stress and the fracture would indeed correspond to a sharp notch. The fractures for the stresses that endure more than 5 x 10^5 cycles (near to the fatigue limit) indeed look like the diagram from a sharp notch. Interestingly, the fracture of the BIQ7 (figure 4.47) did not present a well defined circle in the final fracture, instead a diffuse circle was noticeable. In the BIQ7 treatment, the higher tempering temperature produced an increase on ductility and toughness, allowing the material to fracture by plastic deformation cycles. This is, according to the fractography the final rupture of material might be at a much lower load value than for BIQ4-6 treatments, where the rapid crack growth reaches a minimum area which in addition to the load, exceeded the tensile strength and produced a marked fracture.

This assumption is verified by analysing the load-cycles curves of each condition, as plotted in figure 4.48. It can be noticed that the ultimate load prior to fracture of the BIQ7 is much lower than those for the other heat treatments,

this means that the material withstand more crack propagation since the decrease in load

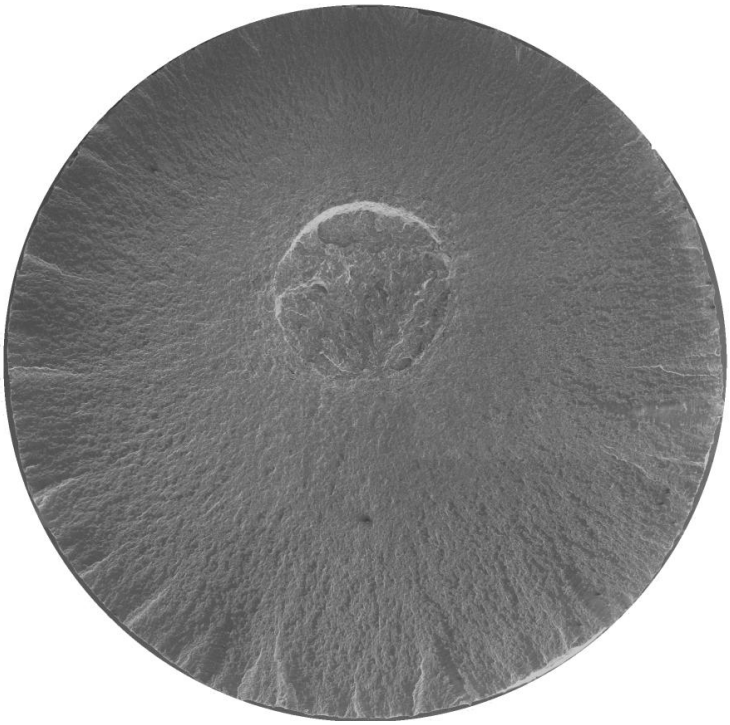

a)

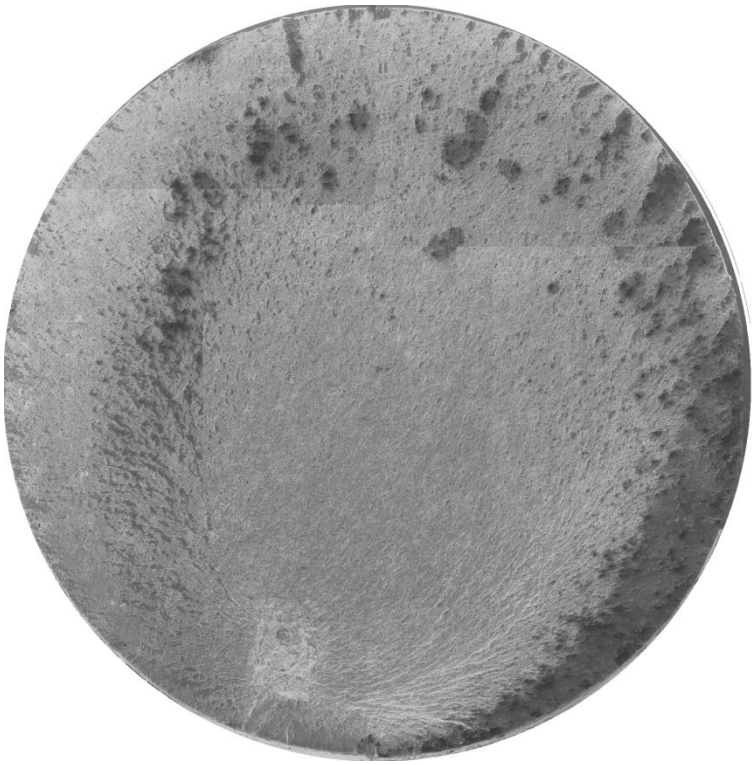

b)

Figure 4.44 Facture of BIQ4 (250°C) samples after $3x10^4$ a) and $1x10^6$ cycles b)

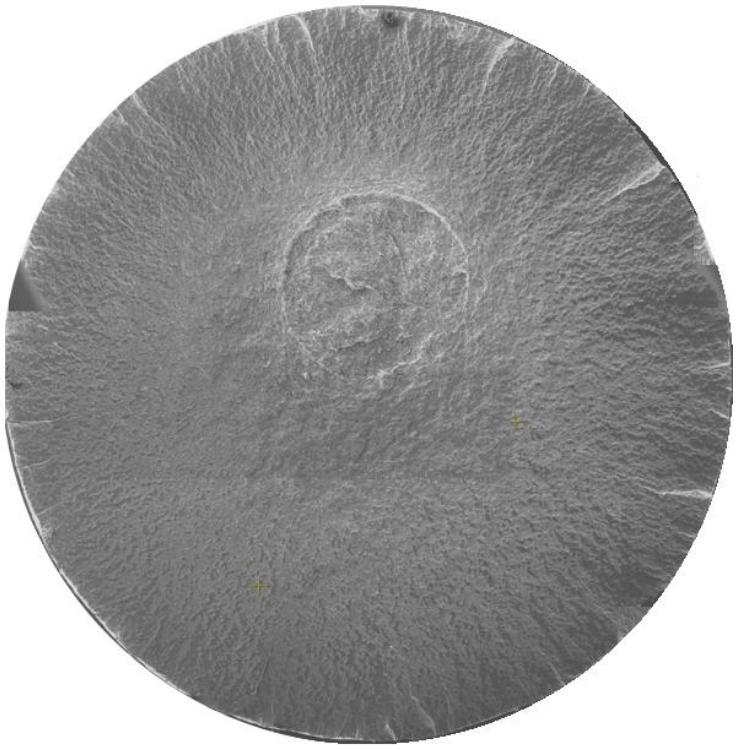

a)

b)

Figure 4.45 Facture of BIQ5 (350°C) samples after $3x10^4$ a) and $1x10^6$ cycles b)

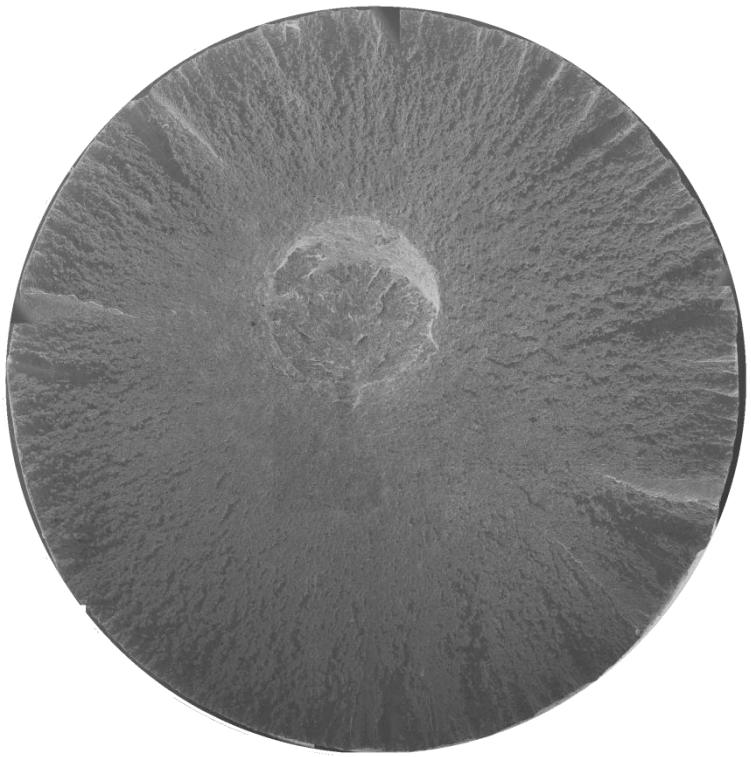

a)

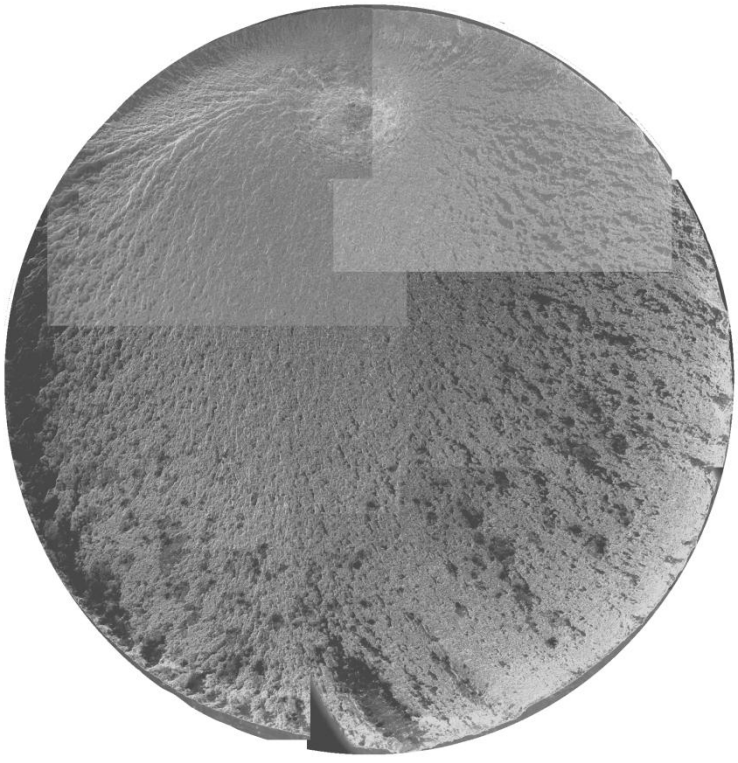

b)

Figure 4.46 Facture of BIQ6 (450°C) samples after $3x10^4$ a) and $1x10^6$ cycles b)

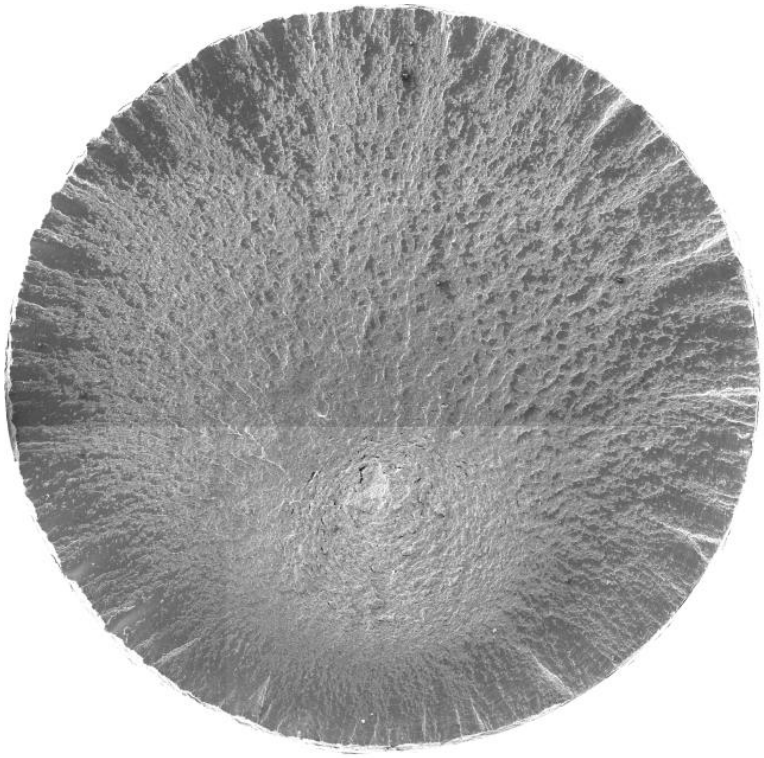

a)

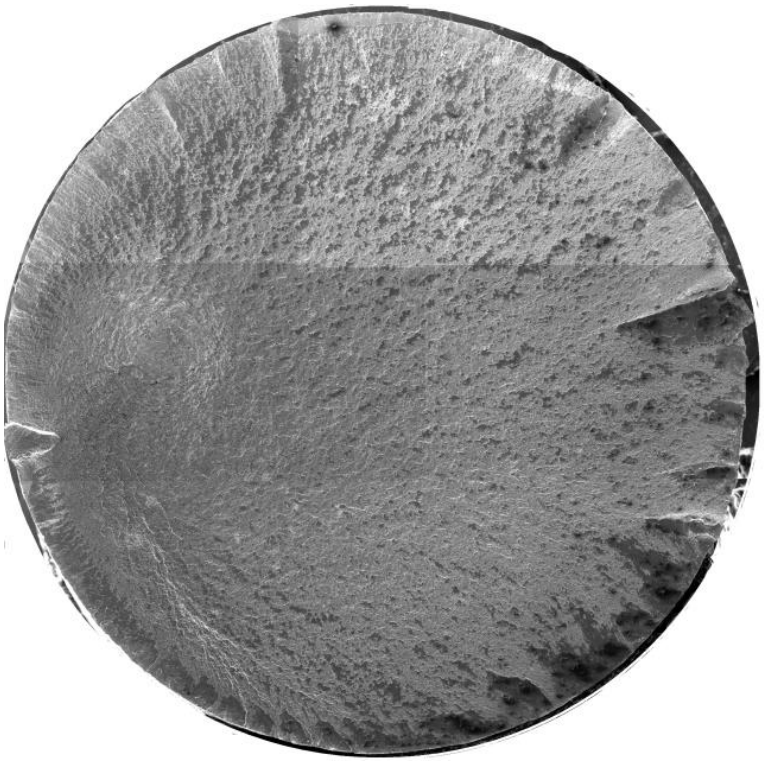

b)

Figure 4.47 Facture of BIQ7 (550°C) samples after $3x10^4$ a) and $6x10^5$ b) cycles

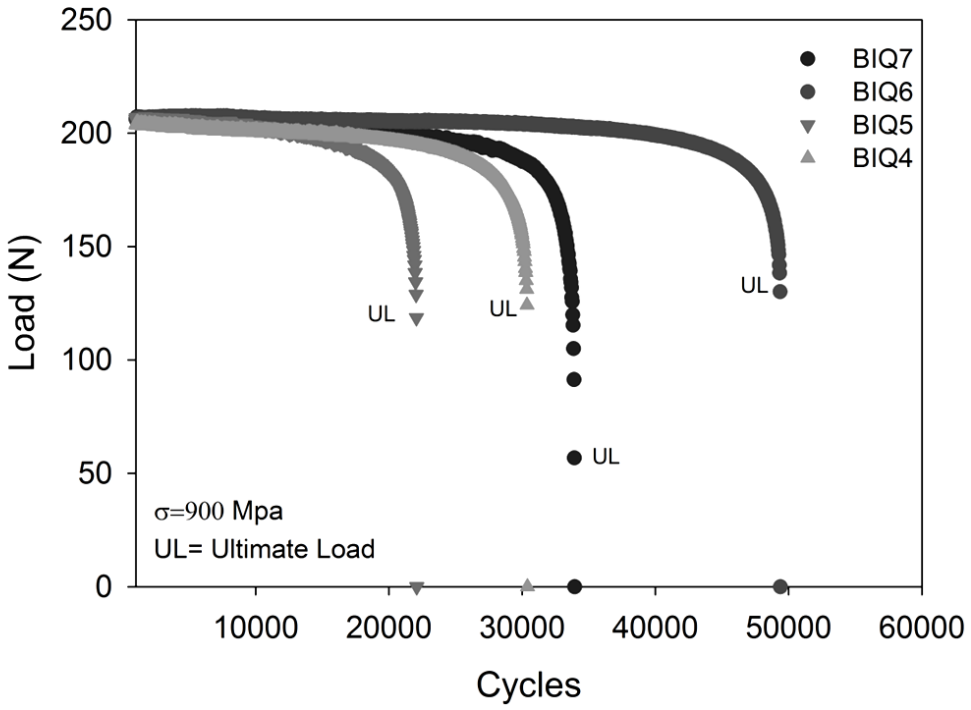

Figure 4.48 Load versus cycles of BIQ4 to 7 at a 900MPa nominal stress, showing the ultimate load prior to fracture.

is related with the increase of cracks in this type of fatigue test. When comparing BIQ7 and BIQ6 curves, it can be noticed that when both loads have decreased to near 125 N, the BIQ6 sample came apart while the BIQ7 sample, although few cycles, withstood the crack propagation until the load was almost 50 N.

The relationship of the load decrease with fractographies is an example of the advantage of registering this information unlikely in common rotating bending testers. The load data obtained during experiments can be used to analyse the mechanisms of cracking during each test. In the next section, a model to determine crack nucleation and crack length is exposed.

4.6.2 Fatigue load analysis

4.6.2.1 Introducing novel concepts

In addition to the ultimate load as showed in figure 4.48, the load versus cycles data can be used to determine the duration of the cracking stages, which was one of the main scopes when the fatigue tester was designed. Before analysing the data some equations and variables are introduced. The fraction of the instant load decrease is calculated from the following equation:

$$L_{frac} = \frac{[L_0 - L_n]}{[L_0]} = 1 - \frac{L_n}{L_0} \qquad \text{Eq. 4.1}$$

where $L_{frac.}$ is the fraction of instant load decrease, L_0 is the initial load and L_n is the load at n cycles. In figure 4.49 a plot log-log of $L_{frac.}$ against cycles is shown and figure 4.50 shows a semi-log plot. It can be noted from both figures that the load decrease has a sigmoidal shape. As shown in figure 4.50 it might be possible to define the cycle of crack nucleation.

In addition, another concept would be introduced in order to be able to note the cracking stages. Thus, the L_{frac} *rate* as function of cycles is calculated, and is named *decrease in load rate* DL:

$$DL = \frac{\delta L_{frac.}}{\delta n} = \frac{[L_{n+1} - L_n]}{[(n+1) - n]} \qquad \text{Eq. 4.2}$$

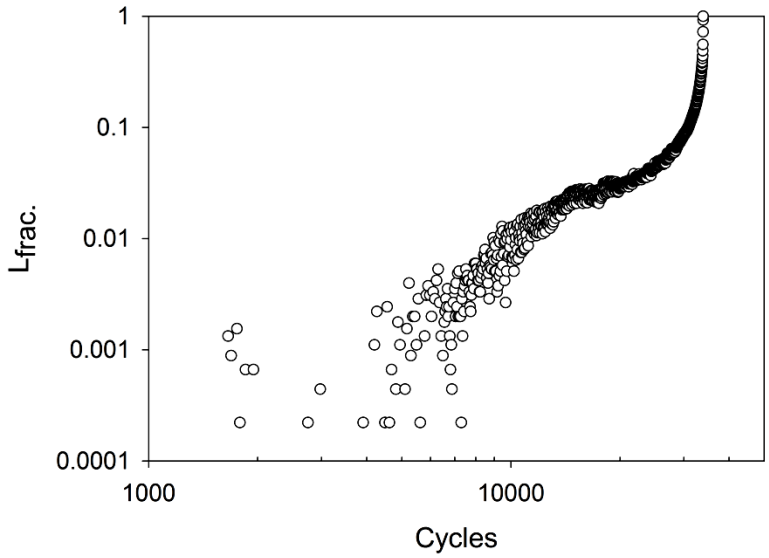

Figure 4.49 $L_{frac.}$ vs. cycles log-log plot

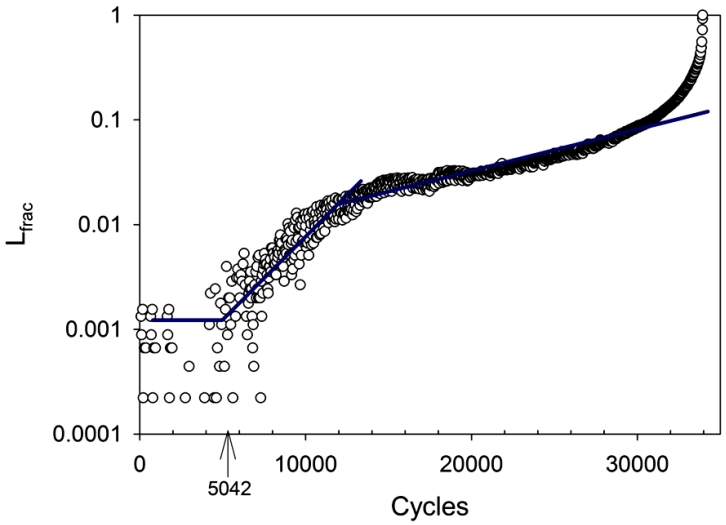

Figure 4.50 $L_{frac.}$ vs. cycles semi-log plot

The *DL rate* is a relationship of the change of load as function of cycles, then since the decrease on load is related to the length of the crack, there is a relationship between the *DL rate* and the crack growth rate. In figure 4.51 the *DL rate* against the number of cycles is plotted. The *DL rate* remained ranging from 1 x 10^{-4} to 1x10^{-5} the first 32500 cycles, then the DL rate grows exponentially until fracture. Since the DL rate and the crack growth rate are related, it could be

stated that the cycles where the DL rate remained stable belong to the second cracking stage, at constant growth rate. Therefore the transition cycle from the second to the third stage of cracking can be pointed out.

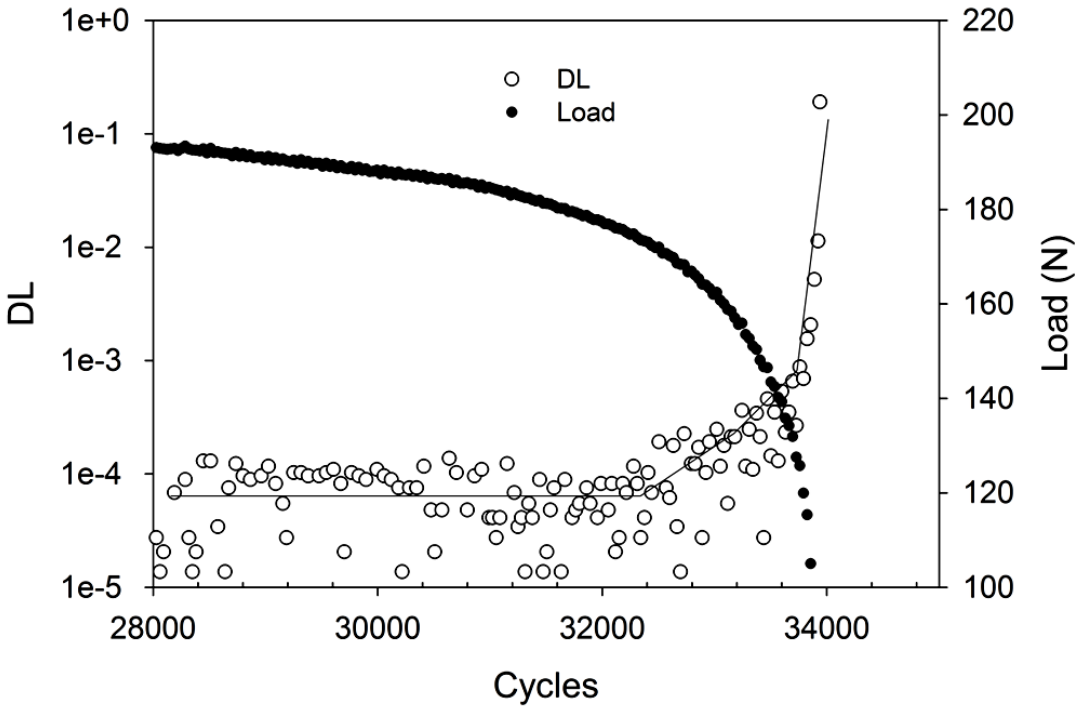

Figure 4.51 DL rate against cycles, showing the transition cycle from the second to the third stage of cracking.

Although the stages might be identified, to determine the relationship between the change in load and the crack length, some assumptions have to be done. A model to estimate the crack length is proposed in the following section.

4.6.2.2 Crack length model

In order to estimate the crack length as function of the load reduction, some assumptions have to be considered when correlating the fractographies of final fractures and the load data. Firstly, it will be assumed that the cracks start all over the surface at the same time, and grow in the radial direction forming a perfect concentric circle, instead of an off-centred one. The area of the overload fracture is assumed to be a perfect circle. Then, the diameter of the final fracture is subtracted from the diameter of the sample, and the value of 2a is obtained. In figure 4.52 a representation of these measurements is shown. Note that the line cross the centre of the sample and the centre of the final fracture.

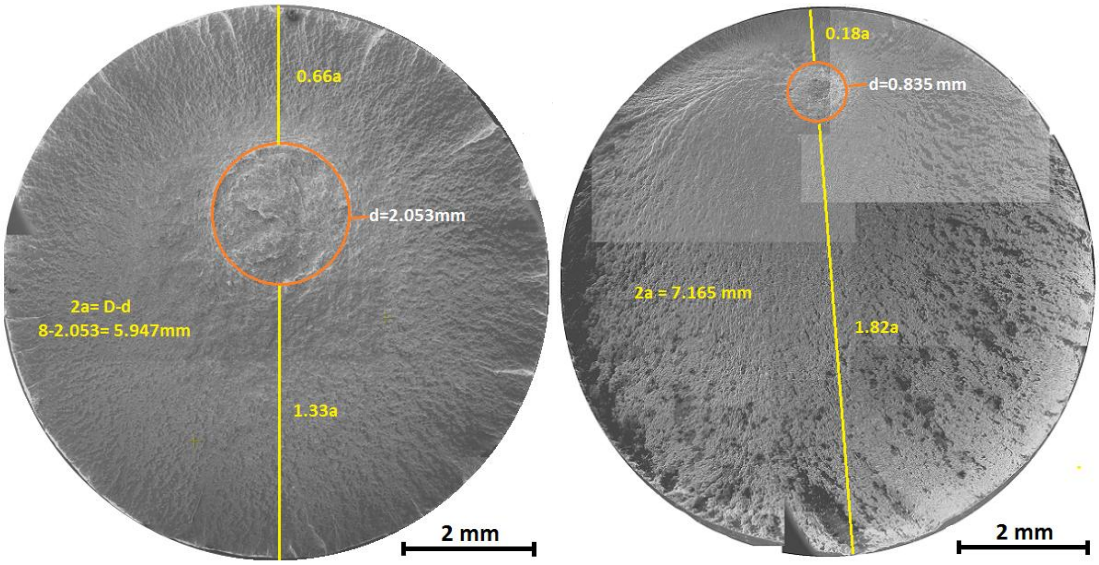

Figure 4.52 Representation of the measures taken from fractures.

With the value of 2a and the ultimate load (averaged 1 second prior to rupture), the relationship between the load and the area reduction was estimated. The fraction of diameter reduced ($d_{frac.}$) is calculated from the following equation:

$$d_{frac.} = 1 - \frac{[d_{ff}]}{D} \qquad \text{Eq. 4.3}$$

where D is the initial diameter of the sample, and d_{ff} is the diameter of the final fracture.

The Ultimate Load Fraction ($UDL_{frac.}$) is the ratio of the ultimate change in load prior to rupture and the initial load of the each experiment and is expressed as follow:

$$UL_{frac.} = 1 - \left[\frac{UL}{L_0}\right] \qquad \text{Eq. 4.4}$$

Then the ratio between the $d_{frac.}$ and $UL_{frac.}$ is calculated and is called the *crack-to-load* factor and it will be represented by the letter *β.* See equation 4.5

$$\beta = \frac{d_{frac.}}{UL_{frac.}} \qquad \text{Eq. 4.5}$$

$$\beta(n) = \frac{d_{frac.(n)}}{L_{frac.(n)}} \qquad \text{Eq. 4.6}$$

From fatigue fractures and the load data a value of β as function of $UL_{frac.}$ was determined, as shown in figure 4.53. The value of β can is obtained from the equation in the figure 4.53 and used to estimate the crack length *2a* at discrete times of the fatigue experiments.

$$\beta(L_{frac.}) = -1.35(L_{frac.}) + 2.28 \qquad \text{Eq. 4.7}$$

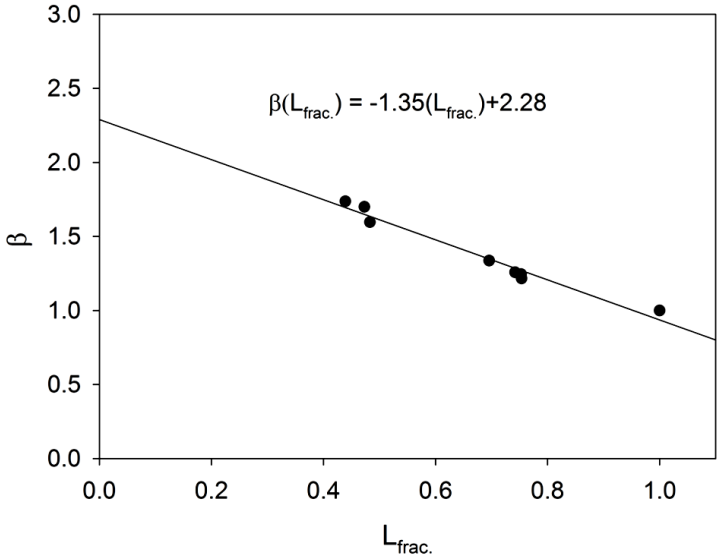

Figure 4.53 Experimental determination of the β factor as function of $L_{frac.}$

4.6.2.3 Crack nucleation and crack length estimation

From 4.54 to 4.57, examples of how the cycle of crack nucleation was determined are shown. The criteria used to define that a nucleation has taken place was a crack length (2a) of 2.5 x 10^{-5} m or a $L_{frac.}$ value of 0.0015. This assumption considers that when a single crack *(a)* of 12.5 μm is present, there is a limited number of cycles before a stable crack growth takes place (II stage).

The results in figures 4.54 to 4.57 show that at the higher stress level, the second tempering at 450°C retarded the crack nucleation up to 8873 cycles, while the tempering at 250°C exhibit a rapid crack nucleation. This rapid nucleation might be due to temper embrittlement and the high hardness of martensite.

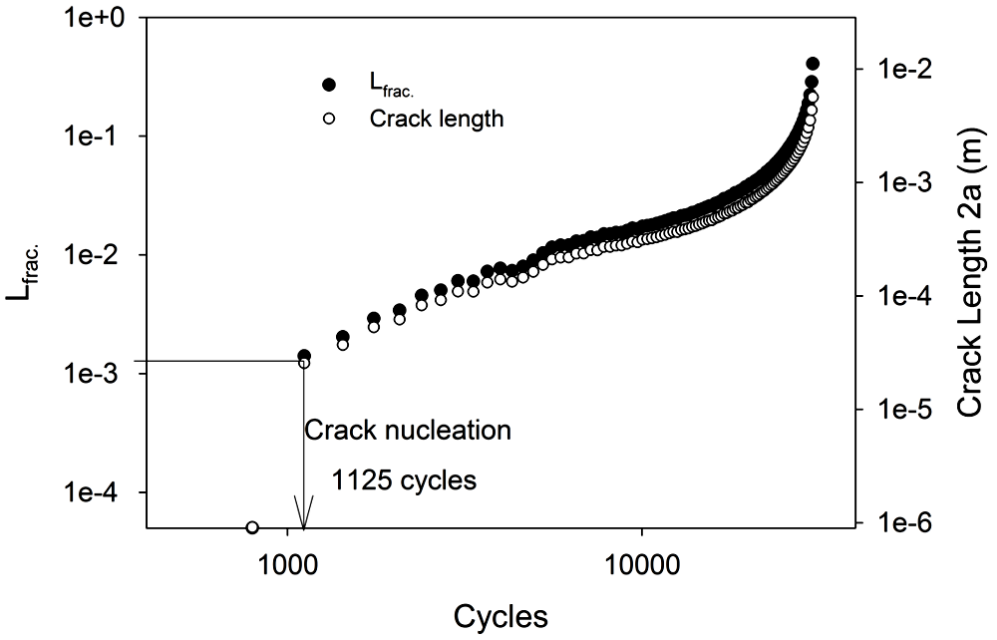

Figure 4.54 Crack length and Lfrac. against cycles, showing crack nucleation of BIQ4 fatigued at 900 MPa.

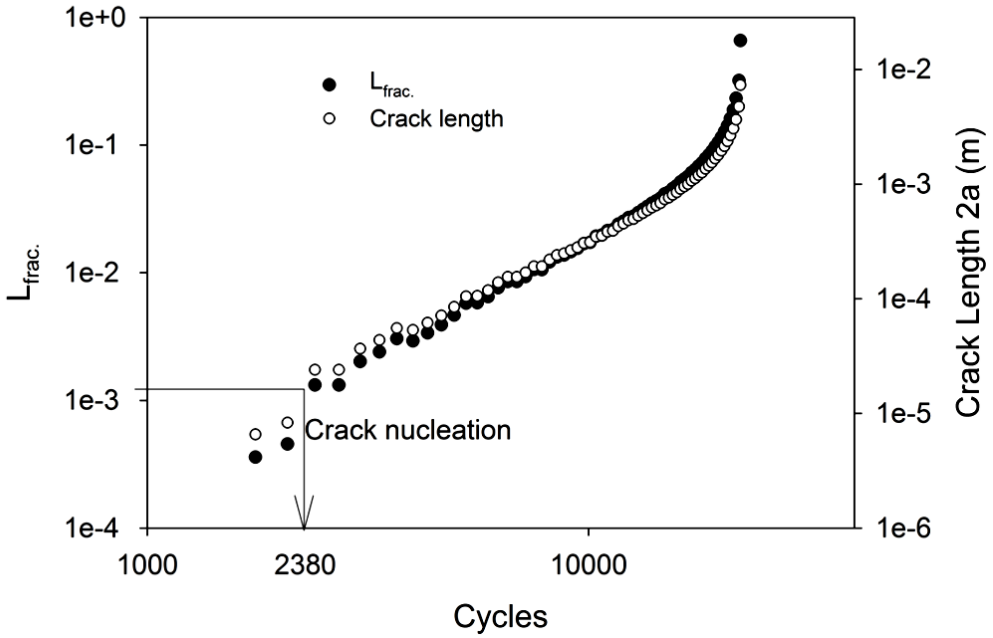

Figure 4.55 Crack length and Lfrac. against cycles, showing crack nucleation of BIQ5 fatigued at 900 MPa.

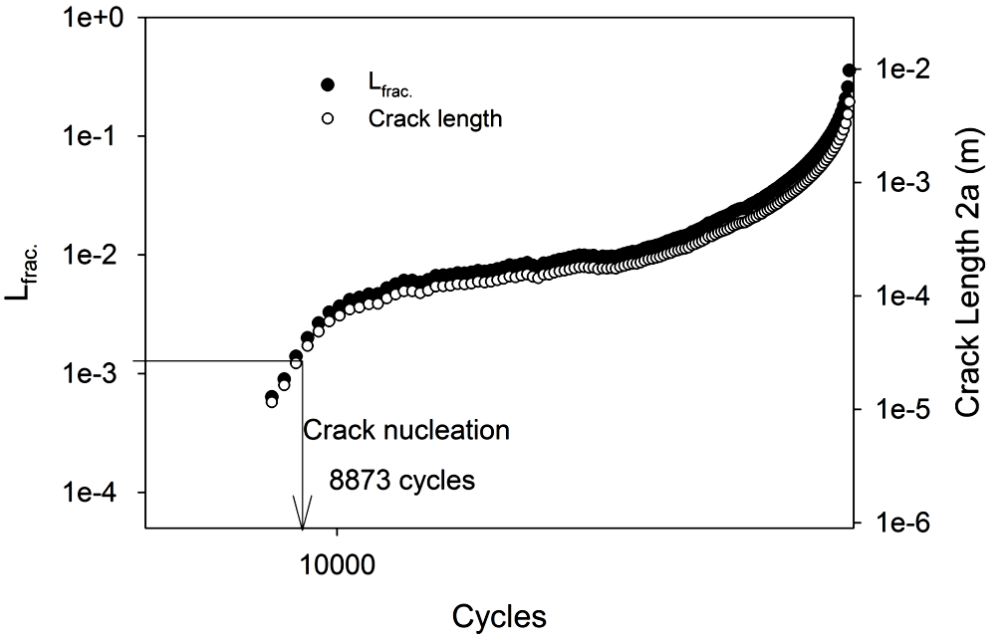

Figure 4.56 Crack length and Lfrac. against cycles, showing crack nucleation of BIQ6 fatigued at 900 MPa.

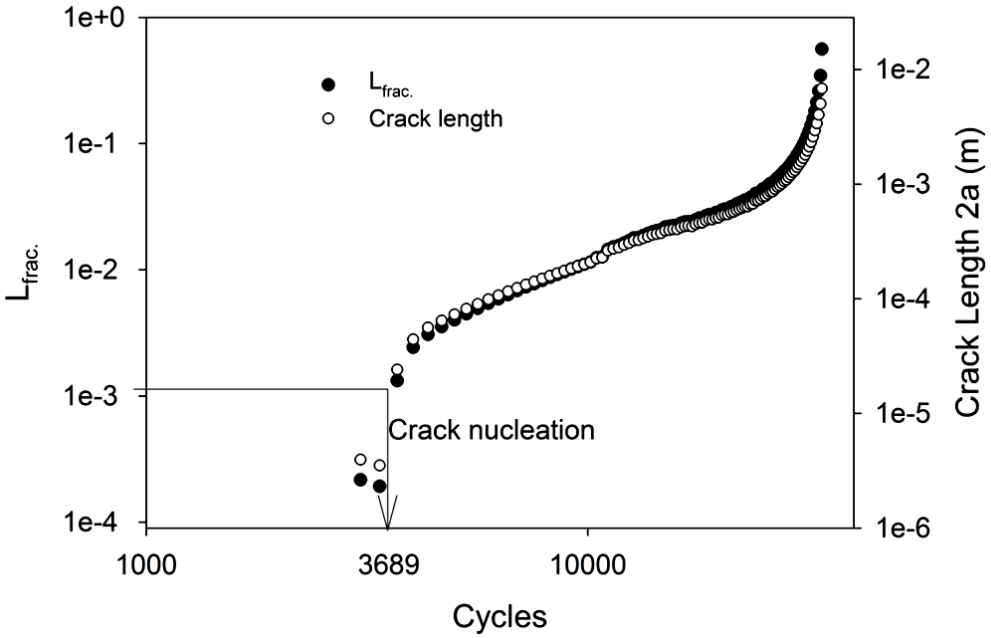

Figure 4.57 Crack length and Lfrac. against cycles, showing crack nucleation of BIQ7 fatigued at 900 MPa.

Interestingly, when the crack length prior to fracture were obtained as function of the ultimate load, it was found that the crack of BIQ7 was longer and in OQ2 was shorter, see figure 4.58a. This means that the nodular bainite encountered in the BIQ7 core allows plastic deformation unlikely the martensite of the through hardened OQ2, which after cracking 0.0035 m did not sustain the load. On the other hand the diameter of the BIQ7 was considerable reduced from the original 0.008 to 0.001 m before rupture. At this stress level only the heat treatment BIQ6 showed a slightly superior fatigue resistance, although low cycle fatigue might not be sufficiently representative of the material resistance.

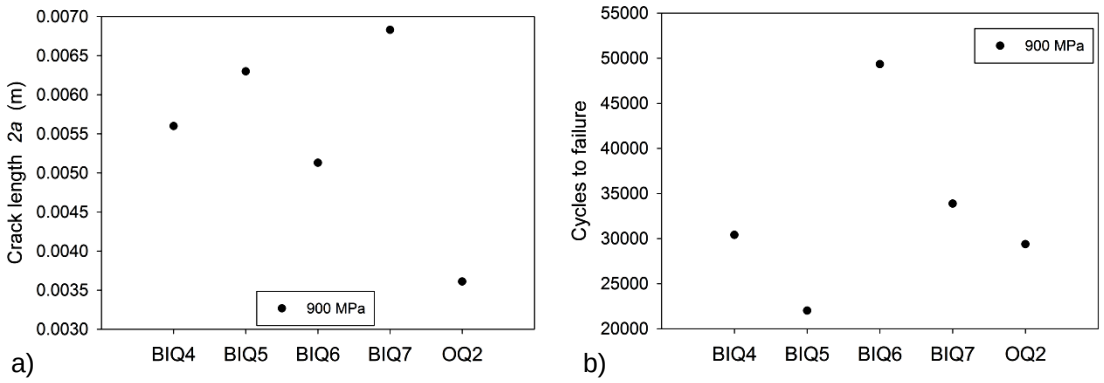

Figure 4.58 Crack length prior to final fracture of fatigue experiments at a stress of 900 MPa. a) and cycles to failure b).

At a medium stress as 600 MPa the fatigue results are more representative, thus a comparison of the crack lengths is illustrated in figure 4.59. Once again the BIQ7 exhibited the longer crack and the OQ2 the shorter one. At this applied stress the BIQ7 failed at 361,000 cycles followed by the BIQ6 and OQ2 at approximately 275,000 cycles. From figure 4.60 can be noticed that crack nucleation took place firstly in the oil quenched sample, before 1354 cycles, while in BIQ7 nucleation occurred after 10,366 cycles.

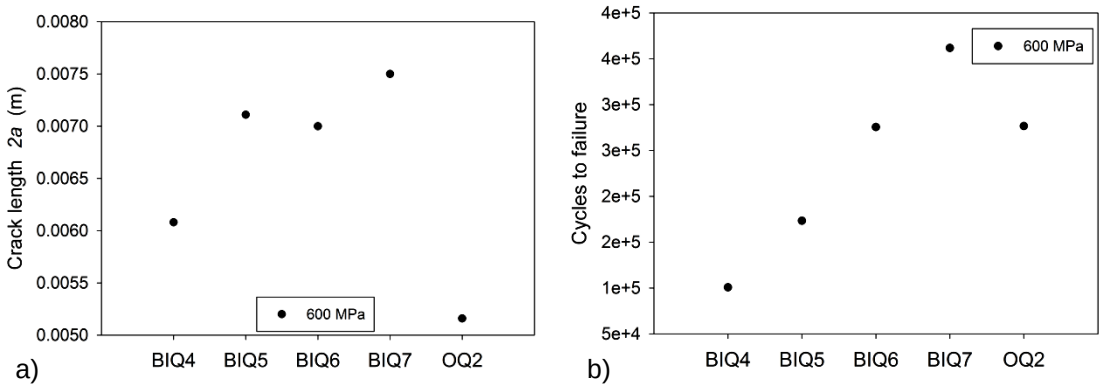

Figure 4.59 Crack length prior to final fracture of fatigue experiments at a stress of 600 MPa. a) and cycles to failure b).

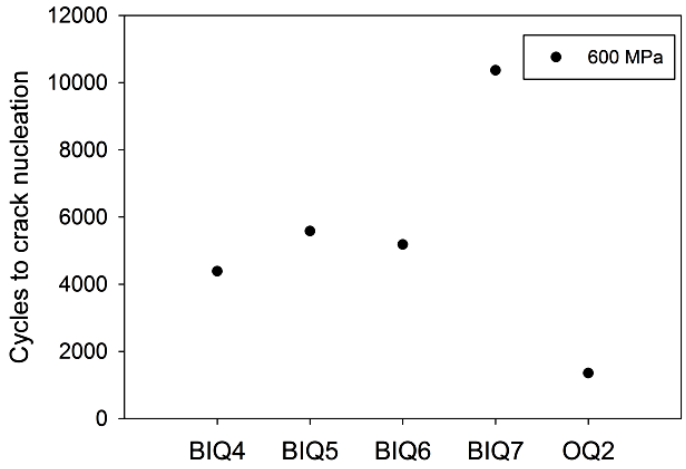

Figure 4.60 Cycles to crack nucleation

The second tempering of the brine interrupted quenching treatments, produced an improvement in the fatigue resistance as the temperature was raised. As mentioned in past sections, this enhancement might be due to isothermal transformation at the core of the retained austenite and more cementite precipitation, or due to the increase in ductility of the tempered martensite. Whether the nucleation is retarded (related to surface) or the crack growth rate reduced (related to core) it might be explained by analysing figure 4.61. The

crack length is displayed in a semi-log plot against cycles. It can be noted that for the heat treatments presented, crack nucleation do not differs substantially among heat treatments when compared with the entire fatigue life. Although in figure 4.60 the crack nucleation was demonstrated to be 2.5 time higher for BIQ7, it represented a minimum percentage of the cycles to failure. It can be concluded that the sharp notch induced the crack nucleation at early cycles, thus the predominant fatigue mechanism involved is crack growth.

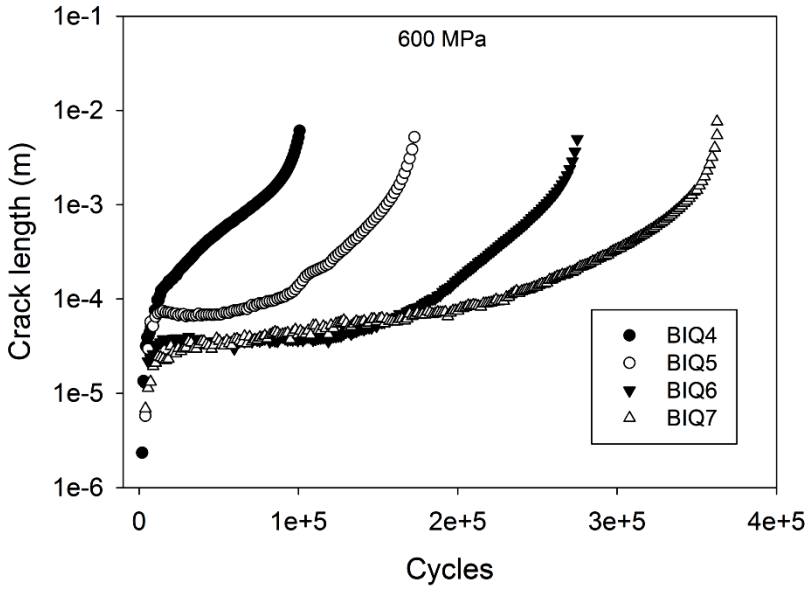

Figure 4.61 Crack length of fatigue experiments carried out at 600 MPa.

Is worth to remark that the crack length in figure 4.61 refers to *2a*, and not to the length of a single crack. The vertical axis is displayed on logarithm scale, and it can be observed that the second stage of cracking for all cases started approximately with a crack length of 6 x 10^{-5} m and the transition to the thirst cracking stage of rapid propagation occurred when the crack length was slightly above 1x 10^{-4} m. The transition from the second to the third cracking stage is more noticeable in figure 4.62, where the crack growth rate is plotted against cycles. Is noted that the crack growth rate remains stable in a range from 5x10^{-10} to 5 x 10^{-9} m for great part of the fatigue life. This is related to the

constant crack growth (II stage), and then a rapid propagation is observed. The change in the crack growth rate is highlighted with coloured lines (green-BIQ4, blue-BIQ5, red-BIQ6 and gray-BIQ7). This same colours are used in figure 4.63 to correlate the crack growth rate with the crack length at the transition point from stage II to III. It was found that the crack length were shorter than 0.5 mm when the transition to the rapid propagation took place, this means that the crack might reached the transition zone from the martensite case to the bainitic core, when faster crack propagation took place. In addition to microstructure, the increase in crack growth rate is also affected by the reduction of the area, which correspond in a local stress increment.

Is worth to mention that the II stage represents almost 60 % of the entire life and the III stage a 40%, while nucleation is only a 2%. Then, it can be concluded that the principal fatigue mechanism is the crack growth or crack propagation. (See figure 4.64)

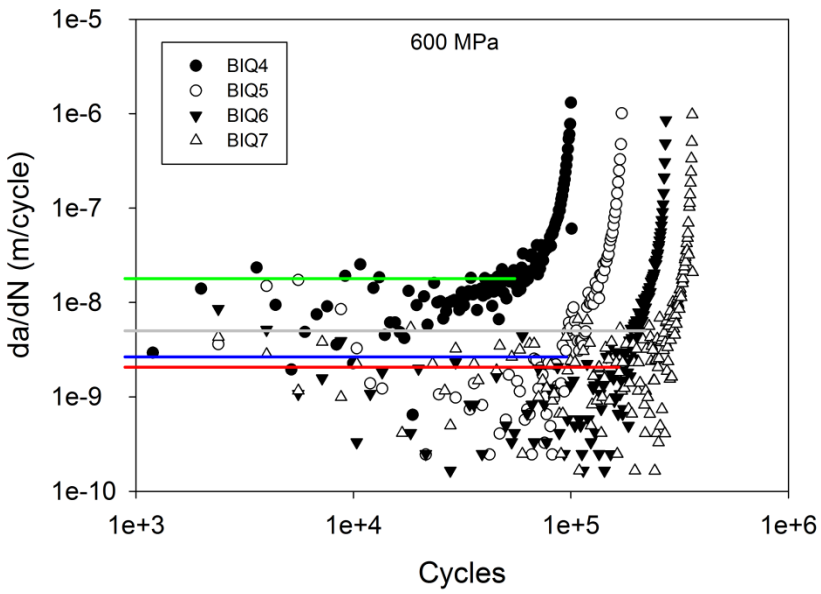

Figure 4.62 Crack growth rate (log) against cycles, showing the transition from cracking stages II to III.

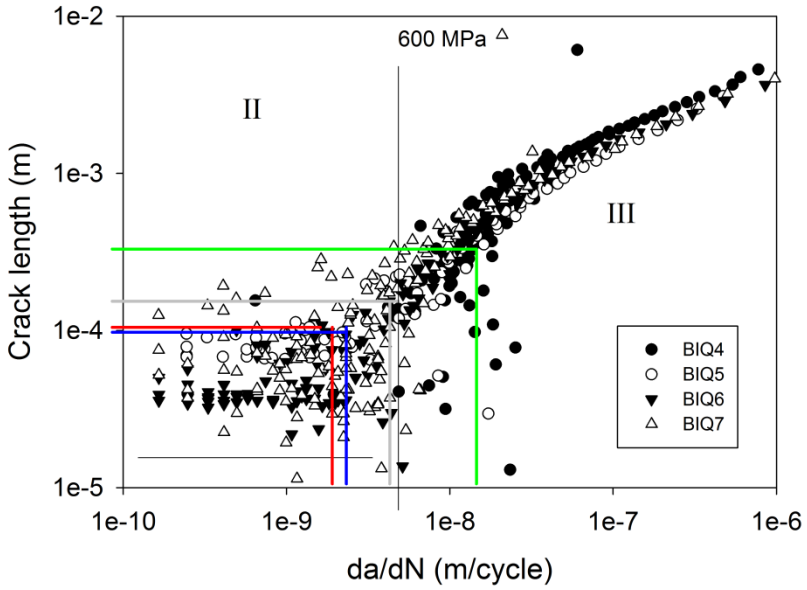

Figure 4.63 Crack length at transition from cracking stage II to III.

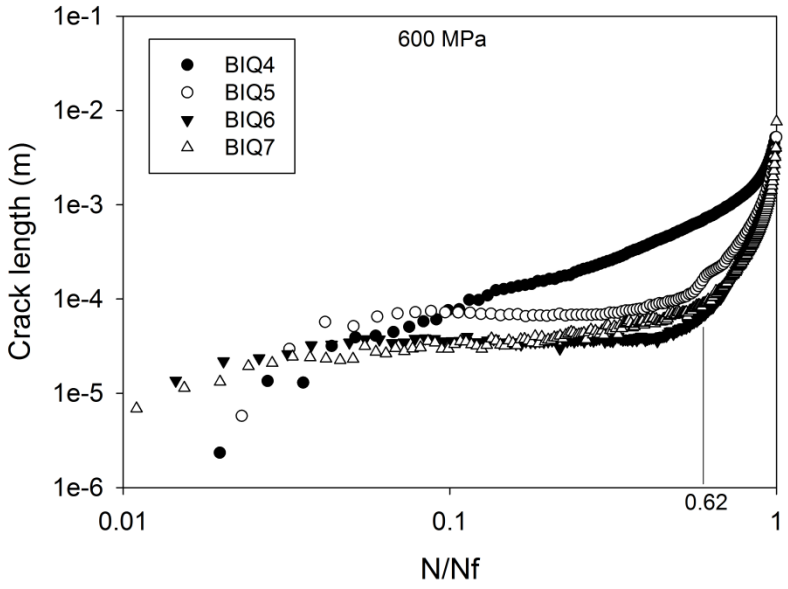

Figure 4.64 Crack length as function of normalized cycles.

Finally, when comparing BIQ7 to BIQ8 load data it was found that nucleation for the BIQ8 (600 MPa) took place after 53,599 cycles. Although this is five times the cycles for nucleation of BIQ7, the transition from the cracking stages II to III occurred only 21,000 cycles later, at 74,399 cycles. The microstructure of BIQ8 contained pearlite at the core and a surface mostly of martensite with traces of pearlite, which formed from retained austenite. The presence of pearlite increased the propagation rate with detrimental effects. Interestingly, the crack length 2a was also 0.0001 m, likely BIQ5, BIQ6 and OQ2. The average crack growth rate of BIQ 7 and BIQ8 at the second stage was $1.6x10^{-9}$ and $1.3x10^{-8}$ m/cycle respectively.

These findings suggest that the delay on nucleation that BIQ8 exhibited might be related to the formation of larger compressive residual stresses when bainite is avoided and instead pearlite is promoted as core structure. However, after a crack is nucleated, it propagated much more rapid, being the bainite a more endurable microstructure.

CHAPTER 5

CLONSLUSIONS AND PROPOSED FURTHER RESEARCH

5.1 Conclusions

The presented research involved different topics as heat transfer, quenching, fatigue and crack modeling. The conclusions will be addressed by topic in the same order as they were treated along this document.

1. Regarding the heat transfer obtained with the $NaNO_2$ solution, it is concluded that the optimal concentration that produce the maximum cooling rate is 4 to 9%, however the more salt additive the solution contains, the higher the saturation temperature of the liquid. Thus, in order to cool the surface to a lower temperature the 4% solution showed better results. The high cooling rates obtained with this corrosion inhibitor, allowed to produce a shell-core type microstructure in thin sections.

2. The parabolic temperature distribution model presented is a useful tool to predict the temperature profile and facilitates the design of the quenching. The parabolic approach showed good correlation with the experimental thermal data and also with the microstructure obtained (case depth). This method is an alternative to the inverse problem methods which are usually more complex and time consuming.

3. The fatigue tester developed in this research allowed for the obtention of important information that common rotating bending fatigue testers are not able to provide. Results of common testers are usually limited to the number of failure cycles. In addition, the new fatigue tester allows the user to estimate if a given test would result in a failure or not after a number of cycles. This is related to experiments carried out near the fatigue limit, where after 1-5 $x10^6$ cycles the user is aware of the presence or absence of a damage, namely cracks.

4. It was demonstrated that a slight partial decarburisation is beneficial in the interrupted quenching. The modification of the martensite start temperature reduced the amount of retained austenite and the increase of the steel fatigue limit.

5. The fatigue limit of the AISI 5160 steel was increased 10% compared to conventional oil quenching and tempering, with a brine interrupted quenching and tempering. Various cooling paths and tempering temperatures were experimented, being the heat treatment BIQ7 that exhibited superior fatigue resistance.

6. The BIQ8 treatment produced a pearlitic core and a martensite case with traces of pearlite. This microstructure retarded the crack nucleation up to 5 times, however after nucleation, propagation was much rapid than in martensite-bainite samples.

7. It was possible to propose a model to correlate the load data with the crack length by using measurements from fatigue fractures and the load data from experiments. The three cracking stages were identified with this methodology. The crack length information is useful for a better understanding of the fatigue process. This crack length model might be useful when the effect of coatings on fatigue is analysed.

8. Although the implementation of the BIQ7 process is complex, it presents the following benefits:

a) The base solution is water which is less expensive than the oil, although the sodium nitrite represents also a considerable cost, only a 4% is needed
b) The washing process after quenching in oil is suppressed
c) The quenching (cooling) time is reduced. In the present work a relation of 60:1 was found and it might increase in larger parts
d) After the interruption of the cooling the material remains hot, therefore do not have to be reheated to be tempered, only isolated and maintained at the desired temperature, thick section even temper themselves. This represents a large amount of energy that is lost when great loads at room temperature are introduced in the furnaces.
e) The increase in the fatigue limit of 10%, implies that a section reduction of 10% is allowable to endure the same load. This represents savings in material and, in the case of vehicles, a direct weight reduction.

5.2 Proposed further research

1. As showed in the results section, the fatigue limit was increased as the second tempering temperature was increased, however experiments were carried out at a maximum tempering temperature of 550°C ,it would be interesting to increase this temperature to 600 650 and 700 °C, followed by fatigue experiments.

2. The decarburisation profile enhanced the fatigue resistance in samples austenitized at 950°C. Previous research have showed that this austenitizing temperature might produce embrittlement. Thus, if a similar decarburisation profile is promoted at lower austenitizing temperatures (longer times) the fatigue limit might be increased. The austenitizing temperatures and times depend on the size and atmosphere of the furnace.

3. The high cooling rates obtained with the sodium nitrite solution are achievable with high speed water. It would be worth to design an automated equipment of high speed water circulation for thin sections as the fatigue samples.

4. The model used to determine the crack length may change for material to material, therefore more materials have to be studied.

References

1. R.I. Stephens, A. Fatemi, R.R. Stephens y H.O. Fuchs, Historical overview of fatigue, Metal Fatigue in Engineering, John Wiley & Sons, 2a ed., 2001, pp (1-9).

2. S. Guo, Study on Reliability Tests to a Few Samples of Mechanical System, Applied Mechanics and Materials Vol. 42, (2011) pp 339-342.

3. N.I. Kobasko, Stress State of Steel Parts during Intensive Quenching, Intensive Quenching Systems: Engineering and Design, ASTM, 2010, pp (107-120).

4. L.C.F. Canale y G.E. Totten, Hardening of Steels, Quenching Theory and Thecnology, Taylor & Francis Group, 2nd ed. 2010, pp (1-42).

5. M.A. Aronov, N.I. Kobasko y J.A. Powell, Review of Practical Applications of Intensive Quenching Methods, Intensive Quenching Systems: Engineering and Design, ASTM, 2010, pp (185-209).

6. L.C.F. Canale, N.I. Kobasko y G.E. Totten, Intensive Quenching Part 1-What is it?, International Heat Treatment and Surface Engineering, vol 1, 2007, pp 30-33.

7. N. I Kobasko y N. I. Prokhorenko, Quenching Cooling Rate Effect on Crack Formation of 45 Steel, Metallovedenie and Termicheskaya Obrabotka Metallov (in Russian), No. 2, 1964, pp. 53-54.

8. H.M. Tensi, A.Stich y G.E. Totten, Quenching and Quenching Technology, Steel Heat Treatment: Metallurgy and Technologies, Taylor & Francis Group, 2007, pp (583-589).

9. N.I. Kobasko, Thermal and Metallurgical basics of design of high-strength steels, Intensive Quenching Systems: Engineering and Design, ASTM

International, 2010, pp (1-23).

10. TOTTEN, G.E.; Bates, C.E.; Clinton, N.A. Handbook of Quenchants and Quenching Technology. ASM Int. 1993, OH USA, 291-338.

11. LISCIC, B.; Filetin, T. Measurement of Quenching Intensity, Calculation of Heat Transfer Coefficient and Global Database of Liquid Quenchants. Mat. Eng. 2012, 19, 52-63.

12. SCOTT, H. The Problem of Quenching Media for the Hardening of Steel. Heat Transfer Symp. Trans. ASM. 1933, 577-584.

13. PETRASH, L.V. Some Physical Phenomena During Quenching. Metallove. Term. Obrab. Met. 1973, 6, 67-70.

14. CHEVRIER, J.C.; Moreaux, F.; Beck, G. L'éffusivité et la résistance thermique des zones superficielles du solide détreminent le processus de vaporisation du liquide en regime de trempe. J.Heat Mass Transfer. 1972, 15, 1631-1645.

15. MOREAUX, F.; J.C. Chevrier; Beck. G. Destabilization of Film Boiling by Means of a Thermal Resistance. Int. J.Multiphase Flow. 1975, 2, 183-190.

16. STEVENS, J.W.; Witte, L.C. Transient Film and Transition Boiling from a Sphere. Int. J. Heat Mass Transfer. 1971, 14, 443-450.

17. THIMBLEBY, H. The Leindenfrost phenomenon. Phys. Educ. 1989, 24, 300-303.

18. N.I. Kobasko, M.A. Aronov y J.A. Powell, Critical Flux Densities and Characteristics of Heat Transfer During Film Boiling, Intensive Quenching Systems: Engineering and Design, ASTM, 2010, pp (45-61).

19. B. Liscic, H.M. Tensi, L.C.F. Canale y G.E. Totten, Quenching Theory and

Thecnology, Taylor & Francis Group, 2a ed. 2010, pp (129-178).

20. B. Liscic, S. Singer & H. Beitz, Dependence of Heat Transfer Coefficient at Quenching on Diameter of Cylindrical Workpieces, J. ASTM Intl., Vol. 8, No. 7.

21. N.I. Kobasko, Intensive Steel Quenching Methods, Intensive Quenching Systems: Engineering and Design, ASTM, 2010, pp (151-169).

22. J.P. Holman, Heat Transfer, McGraw-Hill, décima edición, 2010 pp. (30-31).

23. L.C.F. Canale y G.E. Totten, Quenching Technology: A Selected Overview of the Current State-of-the-Art, 59o Congresso Annual Da ABM/59th Annual Congress International, Julio de 2004, Sao Paulo, Brazil, pp (3705-3716).

24. T. Réti, Residual Stresses in Carburized, Carbonitrided, and Case-Hardened Components, Handbook of Residual Stress and Deformation of Steel, ASM International, 2002, pp (189-208).

25. KOBASKO, N.I.; Prokhorenko, N.I. Effect of the quenching rate on the formation of cracks in steel no. 45. Met. Sci. Heat Treat.1964, 6(2), 104-105.

26. FLETCHER, A.J.; Griffiths, W.D. Heat transfer during vapour blanket stage of quench, Mater. Sci. Technol. 1993, 9 (11), 958-966.

27. LUTY, W. Cooling Media and Their Properties. Quenching Theory and Technology, 2nd Ed. Liscic, B., Tensi, H.M., Canale, L.C.F., Totten, G.E., Eds; Taylor & Francis, 2010, 359-444.

28. PILLING, N.B.; Lynch, T.D. Cooling Properties of Technical Quenching Liquids. Chicago Meeting. 1919.

29. ARAI, T.; Furuya, M. Effect of Hydrated Salt Additives on Film Boiling

Behavior at Vapor Film Collapse. J. Eng. Gas Turbines Power, 2009, 131(1), 012902-6.

30. CUI, Q.; Chandra, S.; McCahan, S. The effect of dissolving salts in water sprays used for quenching a hot surface: part 2- spray cooling. ASME J. Heat Transfer, 2003, 125 (1), 333-338.

31. MUKHINA, M.P.; Kobasko, N.I.;Gordeeva, L.V.Hardening of structural steels in cooling media based on chlorides. Met. Sci. Heat Treat. 1989, 31(9), 677-689..

32. KOBASKO, N.I.; Moskalenko, A.A.; Mazurenko, E.A.; Medvedev, A.M. Intensive Quenching of Tools in Water Salt Solutions. New Aspects Fluid Mech., Heat Transfer Environ. Taipei. 2010, 320-325.

33. SHMYREV, I.P.; Mazanik, V.F. Use of Quenching Media with Different Cooling Capacity in Heat Treating the Grooved Rolls of Cold Rolling Pipe Mills. Metallove. Term. Obrab. Met. 1992, 5, 11-12.

34. LOZANO, D.E.; Mercado-Solis, R.D.; Colás, R.; Canale, L.F.; Totten, G.E. Heat Transfer Coefficients during Quenching of Inconel and AISI 304 Stainless Steel Cylinders in NaNO2 Aqueous Solutions. Proceedings of the 6th Int. Quenching and Distortion Control. **Proc. 6th Int. Quenching and Control of Distortion Conf., Chicago, USA, 2012, 746-754**.

35. PUSTOVOIT, V.N.; Churyukin, Yu.N. Application of an Aqueous Solution Monosulfite Liquor as a Quenching Medium. Metal. Termicheskaya Obrabotka Metallov, 1986, 10, 31-35.

36. KOBASKO, N.I.; Moskalenko, A.A.; Dobryvechir, V.V.; Protsenko, L.M.; Intensive quenching of tools in water salt solutions of optimal concentrations. J. ASTM Int. 2011, 9(2), ID JAI104072.

37. KOBASKO, N.I. Intensive Steel Quenching Methods. Quenching Theory and Technology, 2nd Ed. Liscic, B., Tensi, H.M., Canale, L.C.F., Totten, G.E., Eds; Taylor & Francis, 2010, 509-568.

38. NARAZAKI, M.; Totten, G.E.; Webster, G.M. Hardening by Reheating Quenching. Handbook of Residual Stress and Deformation of Steel. ASM Int. 2002, 270-274.

39. KOBASKO, N.I. Effect of Accuracy of Temperature Measurements on Determination of Heat Transfer Coefficient during Quenching in Liquid Media. J. ASTM Int. 2011, 9(2), ID JAI104173.

40. ASTM D6200-01, Standard Test Method for Determination of Cooling Characteristics of Quench Oils by Cooling Curve Analysis, ASTM Int., 2007.

41. LOZANO, D.E.; Mercado-Solis, R.D.; Colás, R.; Canale, L.F.; Totten, G.E. Surface Temperature and Heat Transfer Coefficient Determination during Quenching for Martensite Fraction Prediction using a Parabolic Heat Transfer Model. **Proc. 6th Int. Quenching and Control of Distortion Conf., Chicago, USA, 2012, 341-348**.

42. T. Lübben, J. Rath, F. Krause, F. Hoffman, U. Fritsching and H. Zoch, Determination of Heat Transfer Coefficient During High-Speed Water Quenching, International Metallurgy and Materials Congress, Istanbul, 2010, pp (1616-1625).

43. HTTP://WWW.ENG.FSU.EDU/~DOMMELEN/QUANTUM/STYLE_A/CBOXTE.HTML (accessed June 2012).

44. NOTTINGHAM, W.B. Thermionic emission. Technical report 321. Research Lab. of Electronics. Massachusetts Institute of Technology. 1956.

45. GUTMAN, E.M. Mechanoemission of Electrons. Mechanochemistry of

Materials. Cambridge Int. Science Publishing. 1998, 130-31.

46. KOBASKO, N.I.; Aronov, M.A.; Powell, J.A.; Totten, G.E. Intensive Quenching Systems: Engineering and Design. ASTM Int. 2010, 53-54.

47. ROSE, M.J. Adsorption of Surface-Active Agents at Interfaces: The Electrical Double Layer. Surfactants and Interfacial Phenomena. 3rd ed. John Wiley & Sons, Inc. 2004, 34-104.

48. QIAO, Y.M.; Chandra, S. Experiments on adding a surfactant to water drops boiling on a hot surface. Proc. R. Soc. Lond. A. 1997, 453, 673-689.

49. BANNYKH, O:A.; Bozhko, G.T.; Tropkina, M.N.; Manikhin, P.I. Oxidation of Steel During Quenching in Aqueous Solutions of Electrolytes. Metallove. Term. Obrab. Met. 1984, 12, 2-3.

50. MOREAUX, F.; Beck. G.; Archambault, P. Effect of Workpiece Surface Properties on Cooling Behavior. Quenching Theory and Technology, 2nd Ed. Liscic, B., Tensi, H.M., Canale, L.C.F., Totten, G.E., Eds; Taylor & Francis, 2010, 289-314.

51. LÜBBEN, T.; Rath, J.; Krause, F.; Hoffman, F.; Fritsching, U.; Zoch, H. Determination of Heat Transfer Coefficient During High-Speed Water Quenching, Int. Met. & Mat. Congress, Istanbul, 2010, 1616-1625.

52. FUNATANI, K.; Narazaki, M.; Tanaka, M. Evaluation of Testing Methods of Cooling Power of Liquid Quenchants.. **Proc. 3rd Int. Conf. Quenching and Control of Distortion, Prague, Czech Replubic, 1999, 515-521.**

53. NARAZAKI, M.; Kogawara, M.; Shirayori, A.; Fuchizawa, S. Accuracy of Evaluation Methods for Heat Transfer Coefficients in Quenching. **Proc. 18th ASM Heat Treating Soc. Conf. 1999, 509-517.**

54. TENSI, H.M.; Liscic, B. Determination of Quenching Power of Various

Fluids.Quenching Theory and Technology, 2nd Ed. Liscic, B., Tensi, H.M., Canale, L.C.F., Totten, G.E., Eds; Taylor & Francis, 2010, 315-358.

55. HASAN, H.S.; Peet, M.J.; Jalil, J.M.; Bhadeshia, H.K.D.H. Heat Transfer Coefficients during Quenching of Steels.

56. SIMENCIO, R.L. Calculation of Kobasko's Simplified HTC from Cooling Curve Data Obtained with small probes. J. ASTM Intl., 2012, 9(4), ID JAI104304.

57. FELDE, I. Estimation of Heat Transfer Coefficient Obtained During Immersion Quenching. **Proc. 6th Int. Quenching and Control of Distortion Conf., Chicago, USA, 2012, 447-456.**

58. HERNANDEZ-MORALES, B.; Lopez-Sosa, F.; Cabrera-Herrera, L. A new Methodology for Estimating Heat Transfer Boundary Conditions during Quenching of Steel Probes.. **Proc. 6th Int. Quenching and Control of Distortion Conf., Chicago, USA, 2012, 81-92.**

59. YING-YI, L. Applied Research on the CaCl2 Aqueous Solution Quenching Medium. Proc. 4th Int. Conf. on Quenching and the Control of Distortion. Beijing. 2003, 257-261.

60. HU, H. The use of an Aqueous Supersaturated CaCl2 Quenching Medium to Quench Adjustable Wenches. Heat Treat. Met., China, 1990, 3, 48-50.

61. A. Wachter, Sodium Nitrite as Corrosion Inhibitor for Water, Industrial and Engineering Chemistry, Vol. 37 No.8, 1945, pp (749-751).

62. M. Levy, Corrosion Inhibitors in AutomotiveCoolant Media, Industrial and Engineering Chemistry, Vol. 50 No4, 1958, pp(657-662).

63. ARAMIDE, F.O. Corrosion Inhibition of AISI/SAE Steel in Marine Environment. Leonardo Journal of Sciences, 2009 (15), 47-52.

64. SUSSMAN, S.; Nowakowski, O.; Constantino, J.J. Experiences with Sodium Nitrite- Unpredictable Corrosion Inhibitor. Ind. and Eng. Chemistry. 1959, 51(4), 581-584.

65. COHEN, M. Inhibition of Steel Corrosion by Sodium Nitrite in Water. Columbus Ohio Meeting, 1948, 26-39.

66. N.I. Kobasko, Transient Nucleate Boiling and Self-Regulated Thermal Processes, Intensive Quenching Systems: Engineering and Design, ASTM, 2010, pp (39-40).

67. J.P. Holman, Heat Transfer, McGraw-Hill, décima edición, 2010 pp. (168-173).

68. B. Liscic and T. Filetin, Measurement of Quenching Intensity, Calculation of Heat Transfer Coefficient and Global Database of Liquid Quenchants, Mat. Eng. 19, 2012, p 52-63.

69. H.S. Hasan, Evaluation of Heat Transfer Coefficients during Quenching of Steels, Ph.D. Thesis, University of Cambridge, UK, 2009.

70. B. Hernandez-Morales, F. Lopez-Sosa and L. Cabrera-Herrera, A new Methodology for Estimating Heat Transfer Boundary Conditions during Quenching of Steel Probes. Proc. 6th Int. Quenching and Control of Distortion Conference, pp.81-92, 2012.

71. L. Meekisho, B. Hernández-Morales, J.S. Téllez-Martínez and X. Chen, Computer-aided cooling curve analysis using WinProbe, Int. J. Materials and Product Thecnology, 2005, vol. 24, 155-169.

72. J.V. Beck, Nonlinear Estimation Applied to the Nonlinear Inverse Heat Conduction Problem, Int. J. Heat Mass Transfer, Vol. 13, 1970, pp (703-716).

73. I. Felde, Estimation of Heat Transfer Coefficient Obtained During Immersion Quenching, Proc. 6th Int. Quenching and Control of Distortion Conference, pp. 447-456, 2012.

74. R.A. Harding, Ph.D. Thesis, University of Sheffield, UK 1976.

75. H.K.D.H. Bhadeshia and R.W.K. Honeycombe, The Heat Treatment of Steels: Hardenability, Steels Microstructure and Properties, Butterworth-Heinemann Elsevier, 3dr ed. 2006, pp (167-181).

76. M. Przylecka, W. Gestwa, L. Canale and G.E.Totten, Sources of Failures in Carburized and Carbonitrided Components, Failure Analysis of Heat Treated Steel Components, ASM International, 2008, pp(177-234).

77. H.K.D.H. Bhadeshia and R.W.K. Honeycombe, Formation of Martensite, Steels Microstructure and Properties, Butterworth-Heinemann Elsevier, 3dr ed. 2006, pp (95-127).

78. G. Krauss, Martensite, Steels: Processing, Structure and Performance, ASM International, 2005, pp (55-86).

79. G.E. Totten, C.E. Bates and N.A. Clinton, Other Quenching Processes, Handbook of Quenchants and Quenching Technology, ASM International, 1993, pp(304-309).

80. G. Parrish, Retained Austenite, Carburizing Microstructure and Properties, ASM International, 1st ed. 1999, pp (77-94).

81. G. Krauss, Hardness and Hardenability, Steels: Processing, Structure and Performance, ASM International, 2005, pp (297-326).

82. H.K.D.H. Bhadeshia, Program MAP STEEL MUCG73, http://www.msm.cam.ac.uk/map/steel/programs/mucg73-b.html.

83. INTERNET source, http://calculations.ewi.org/vjp/secure/TTTCCTPlots.asp, accesed on June 2011.

84. M. Meier, Jominy Test Data and Hardenability Calculations per ASTM A 255-89 (software), version 2.02, 2001.

85. J.VATAVUK and L.C.F. Canale, Steel Failures due to Tempering and Isothermal Heat Treatment, Book Chaper, Failure Analysis of Heat Treated Steel Components, ASM Int., 2008, pp (285-309).

86. D.S. Clark, Physical Metallurgy for Enginers, agreagar capitulo y paginas.

87. H.K.D.H. Bhadeshia and R.W.K. Honeycombe, The Tempering of Martensite, Steels Microstructure and Properties, Butterworth-Heinemann Elsevier, 3dr ed. 2006, pp (183-207).

88. G. Krauss, Tempering of Steel, Steels: Processing, Structure and Performance, ASM International, 2005, pp (327-352).

89. ASM Handbook vol 19: Fatigue and Fracture, ASM International, 1996, pp (1548-1550).

90. M.S. Htun, S.T. Kywa and K.T. Lwin, Effect of Heat Treatment on Microstructure and Mechanical Properties of Srping Steel, J. of Metals and Minerals, Vol.18 No.2, 2008, pp (191-197).

91. HAFTRIRMAN, A.S. Rahman, M.A. Mat and F. Sutrisno, Effect of Tempering Temperature on Fatigue Strength of Thyssen 6582 Steel, Conf. on Applications and Design in Mechanical Engineering, Malaysia, 2007.

92. S. Sato, K.Inoue and A.Ohno, The Effect Of Shot-Peening to Decarburized Spring Steel Plate,First International Conference on Shot Peening, Paris,1981, pp 303-314.

93. K. DALAEI, J. HÖIJER, G. ÅKERSTRÖM, B. KARLSSON and L.E. SVENSSON, Influence of Decarburization on the fatigue behaviour of shot peened spring steels, www.shotpeener.com/library/pdf/2008081.pdf.

94. S.S. Manson and G.R. Halford, Fatigue and Durability of Structural Materials, ASM International, 2006.

95. R.I. Stephens, A. Fatemi, R.R. Stephens y H.O. Fuchs, Fatigue Tests and the Stress-Life (S-N) Approach, Metal Fatigue in Engineering, John Wiley & Sons, 2a ed., 2001, pp (59-92).

96. R.I. Stephens, A. Fatemi, R.R. Stephens and H.O. Fuchs, Notches and their effects, Metal Fatigue in Engineering, John Wiley & Sons, 2a ed., 2001, pp (186-243).

97. G.E. Totten, personal communication.

98. X. Chen, L. Meekisho and G.E. Totten, Computer-Aided Analiysis of the Quenching Probe Test, Heat Treating: Proc. 18th Conf., 1999, pp (545-551).

99. B. Liščić, S. Singer and B. Smoljan, Predictionof Quench-Hardness within the Whole Volume of Axially Symmetric Workpieces of Any Shape, J. ASTM Int., Vol. 7(2), ID JAI102647.

100. N.I. Kobasko, Effect of Accuracy of Temperature Measurements on Determination of Heat Transfer Coefficient during Quenching in Liquid Media, J. ASTM Int., Vol. 9 No.2,2012.

101. E. Carvalho, M.R. Fernandes, S. Augustinho, L.F. Canale and G.E. Totten, Comparison of Structure and Quenching Performance of Vegetable Oils, J. ASTM Int. vol.6 No.9.

102 M. Narazaki, S. Asada & K. Fukahara, Recent Research on Cooling Power

. of Liquid Quenchants, 2nd Int. Conf. on Quenching and the Control of Distortion, 1996, p 37-46.

103 L.F.C Canale, R. Mesquita and G.E. Totten, Steel Heat Treatment Failures
. due to Quenching, Failure Analisys of Heat Treated Steel Components, ASM International, pp (255-284).

104 G. Parrish, Postcarburizing Thermal Treatments, Carburizing Microstructure
. and Properties, ASM International, 1st ed. 1999, pp (171-195).

105 R.I. Stephens, A. Fatemi, R.R. Stephens y H.O. Fuchs, Fatigue from
. variable amplitude loading, Metal Fatigue in Engineering, John Wiley & Sons, 2a ed., 2001, pp (270-317).

106 W.J. Nam, C.S. Lee and D.Y.Ban, Effects of alloy assitions and tempering
. temperature on the sag resistance of Si-Cr spring steels, Materials Science & Engineering, 2000, pp 8-17.

107 J.P. Wise, G. Krauss and D.K. Matlock, Microstructure and Fatigue
. Resistance of Carburized Steels, 20th ASM Heat Treating Society Conference Proceedings, ASM International, 2000, pp (1152-1161).

108 G. Parrish, Decarburization, Carburizing Microstructure and Properties,
. ASM International, 1st ed. 1999, pp (37-50).

109 R.G. Baggerly and R.A. Drollinger, Determination od Decarburization in
. Steels, Journal of Materials Engineering and Performance, 1993, pp (47-50).

110 A.R. Marder, S.M. Perpetua, J.A. Kowalik and E.T. Stephenson, The Effect
. of Carbon Content on the Kinetics of Decarburization in Fe-C Alloys, Metellurgical Transactions A, Volume 16A, June 1985, pp (1160-1163).

111 D. Au, The Effect of Heat Treatment Atmosphere on Hardening of Surface

. Region of H13 Tool Steel, Postgraduate Diploma in Research, Aukland University of Technology, Aukland 2006, pp (17-34).

112 H. Cheng, T. HE and J. XIE, Solution of an Inverse Problem of Heat . Conduction of 45 Steel with Martensite Phase Transformation in High Pressure during Gas Quenching, J. Materials Science and Technology, Vol. 18, 2002, pp (372-374).

113 K.C. Deshmukh, S.D. Warbhe, G.D. Kedar and V.S. Kulkarni, Inverse Heat . Conduction Problem in a Semi-Infinite Cylinder and its Thermal Stresses by Quasi-Static Approach, Applications and Applied Mathematics Journal, Vol. 6 2011, pp (1883-1892).

114 T. Oguri, K. Murata and Y. Sato, X-ray Residual Stress Analysis of . Cylindrically curved surfaces- estimation of circumferential distributions of residual stresses, Journal of Strain Analysis, Vol. 38 No.5, 2003, pp (459-468).

115 P.G. Shewmon, Diffusion in Solids, McGraw-Hill.
.

116 S.H. Avner, Introduction to Physical Metallurgy, McGraw-Hill, 2nd ed., pp . (252-347).

117 N. Birks, G.H. Meier and F.S. Pettit, Oxidation and decarburization of steels, . Introduction to the High Temperature Oxidation of Metals, 2nd ed., Cambridge 2006, pp (151-162).

118 G. Krauss, Isothermal and Continuos Cooling Transformation Diragrams, . Steels: Processing, Structure and Performance, ASM International, 2005, pp (181-196).

119 G. Krauss, Residual Stresses, Distortion, and Heat Treatment, Steels: Processing, Structure and Performance, ASM International, 2005, pp (417-

. 426).

120 C. Ruud, Measurement of Residual Stresses, Handbook of Residual Stress
. and Deformation of Steel, ASM International, 2002, pp (99-117).

121 H.S. Hasan, M.J. Peet, J.M. Jalil and H.K.D.H. Bhadeshia, Heat Transfer
. Coefficients during Quenching of Steels.

122 H.K.D.H. Bhadeshia, Some Phase TRansformations in Steels, Cambridge.
.

123 L.J. Ebert, The Role of Residual Stresses in the Mechanical Performance of
. Case Carburized Steels, Metallurgical Transactions A, Vol. 9A, 1978, pp (1537-1551).

124 P. Fernandes and K.N. Prabhu, Comparative Study of Heat Transfer and
. Wetting Behaviour of Conventional and Bioquenchants for Industrial Heat Treatment, Internatinoal Journal of Heat and Mass Transfer, Vol. 51, 2008, pp (526-538).

125 J. Rath, T. Lübben, F. Hoffman and H.-W. Zoch, Generation of compressive
. residual stresses by high speed water quenching, International Heat Treatment and Surface Engineering, Vol. 4 No. 4, 2010, pp (156-159).

126 J.V. Beck, Nonlinear Estimation Applied to the Nonlinear Inverse Heat
. Conduction Problem, Int. J. Heat Mass Transfer, vol. 13, pp. 703-716, 1970.

LIST OF TABLES

LIST OF FIGURES

APENDIX A

Non-metallic inclusions in AISI 5160

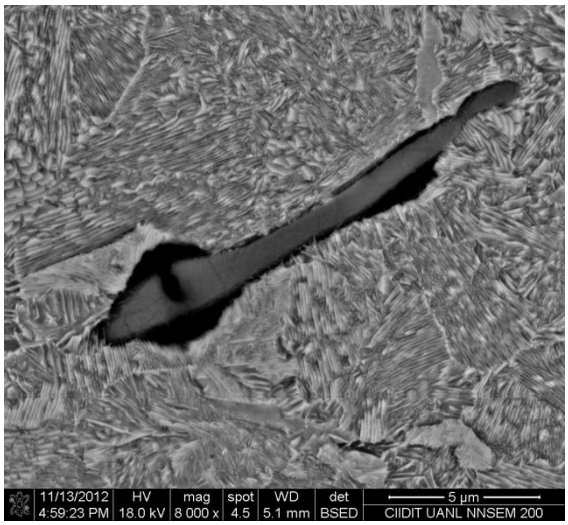

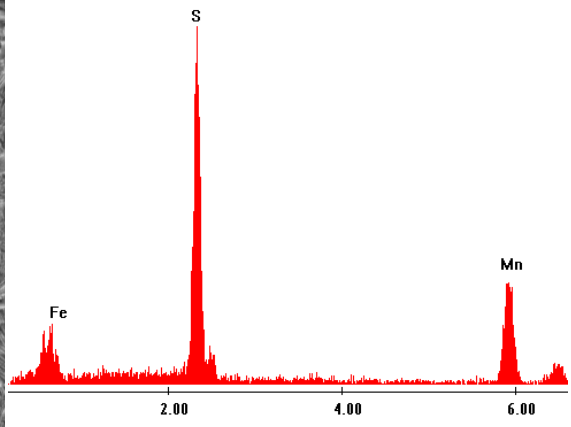

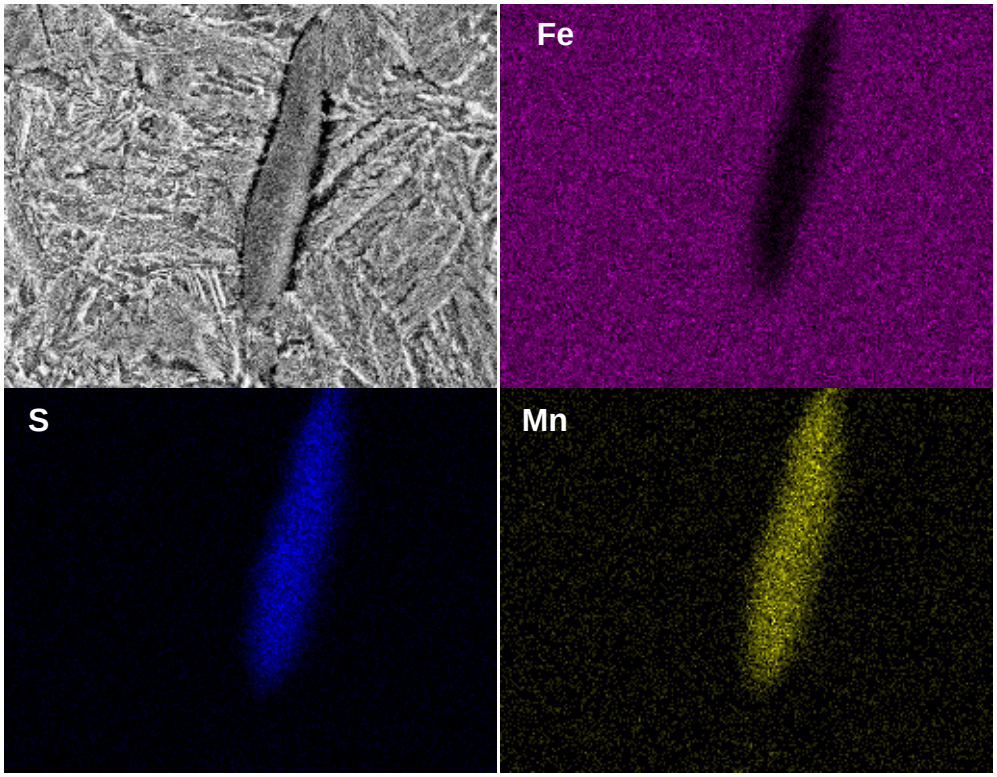

APENDIX B

Fracture surface of the OQ2 (600 MPa.) showing no delimited final fracture. And closer inspection showing cracking stages (below left image) and intergranular fracture of the tempered martensite (below right).

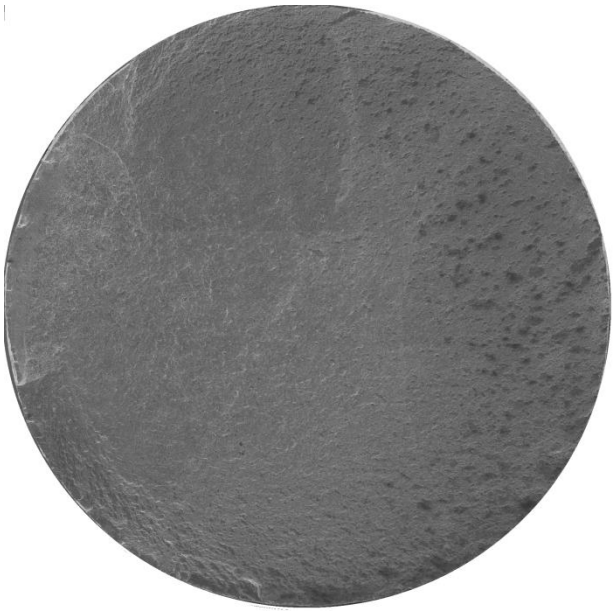

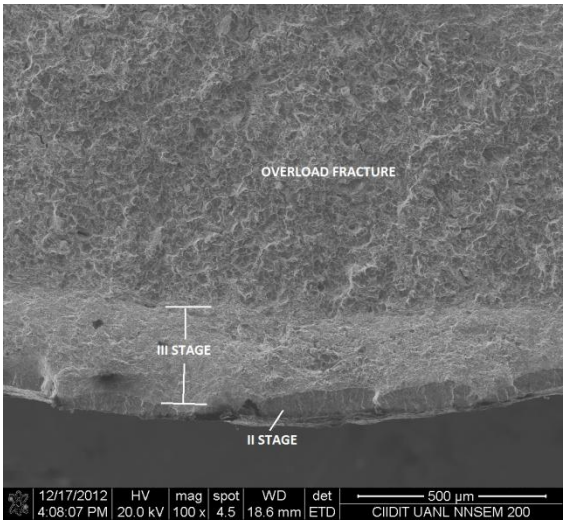

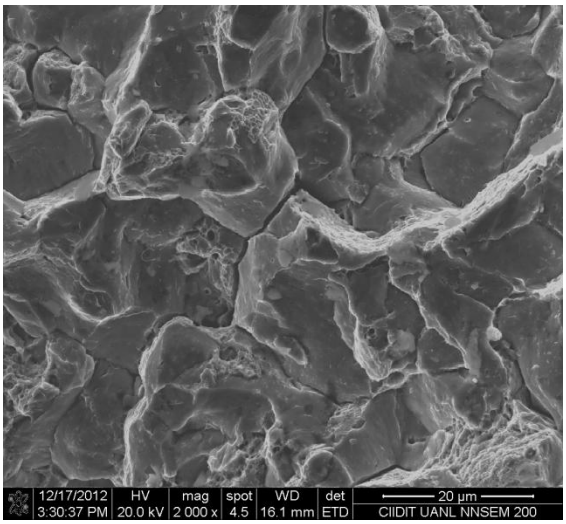

APENDIX C

SEM images showing the cracking stages of BIQ7 (900 MPa.)

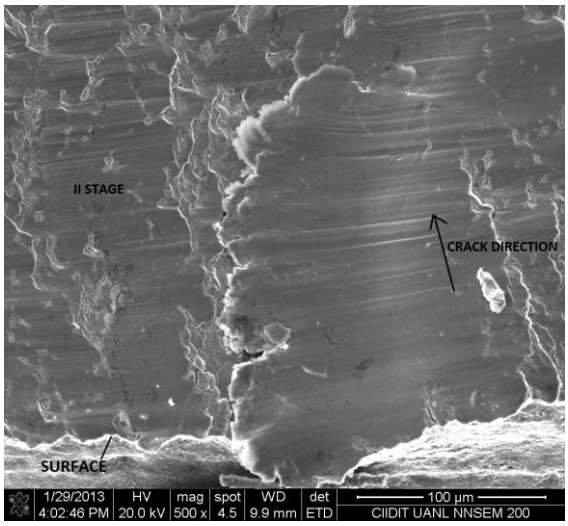

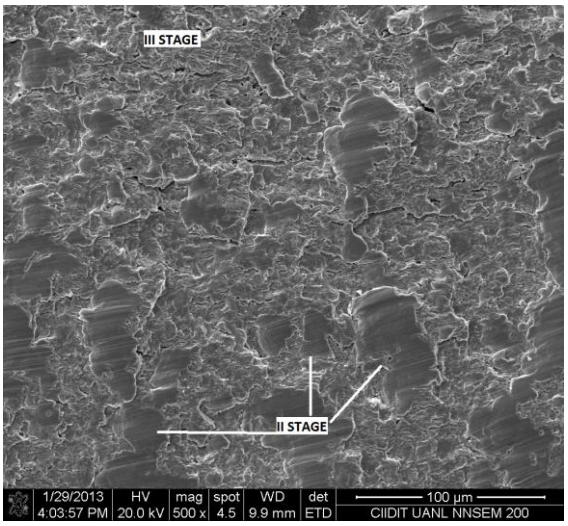

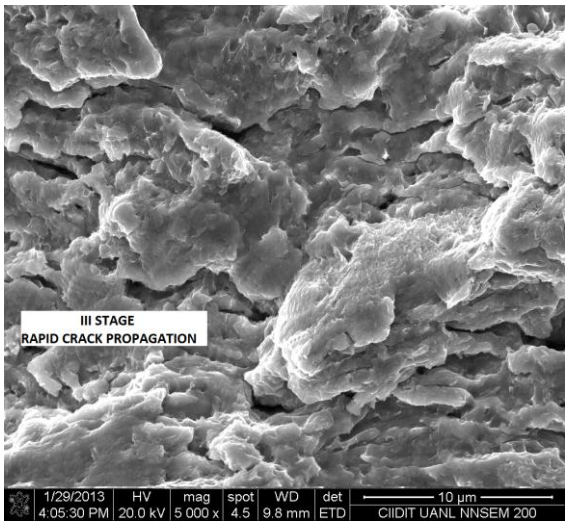

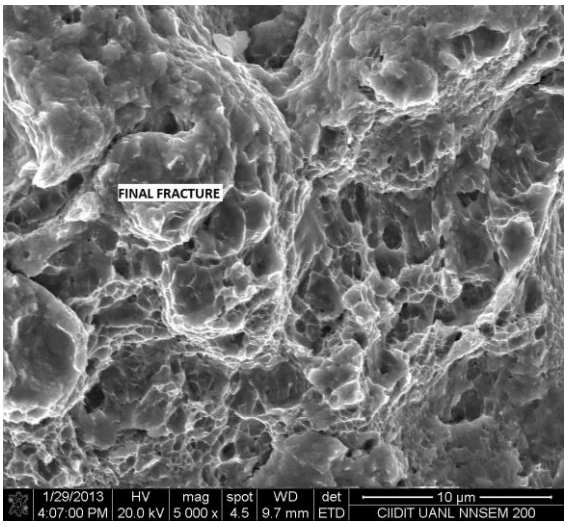

AUTOBIOGRAPHY

Diego Emilio Lozano de la Garza

Born in 1984, Diego E. Lozano finished his college degree in Mechanical and Electrical Engineering in 2006. Same year started his Master in Materials Engineering, where he conducted a research on wear of an aluminum alloy. In 2008 received his Master degree. From 2010 to 2013 completed his Doctoral degree in Materials Engineering with a project related with heat treatments and fatigue of spring steel.

From 2007 to 2011 designed and constructed different laboratory machines, including a pin-on-disk tribometer, a rotating bending fatigue tester and a high speed water quenching system.